

May 2020

Harbingers of Exotic Transients: The Electromagnetic Follow-up of Gravitational-wave Transients & Transient Rates

Deep Chatterjee
University of Wisconsin-Milwaukee

Follow this and additional works at: <https://dc.uwm.edu/etd>



Part of the [Astrophysics and Astronomy Commons](#)

Recommended Citation

Chatterjee, Deep, "Harbingers of Exotic Transients: The Electromagnetic Follow-up of Gravitational-wave Transients & Transient Rates" (2020). *Theses and Dissertations*. 2363.
<https://dc.uwm.edu/etd/2363>

This Dissertation is brought to you for free and open access by UWM Digital Commons. It has been accepted for inclusion in Theses and Dissertations by an authorized administrator of UWM Digital Commons. For more information, please contact open-access@uwm.edu.

HARBINGERS OF EXOTIC TRANSIENTS:
THE ELECTROMAGNETIC FOLLOW-UP OF
GRAVITATIONAL-WAVE TRANSIENTS
&
TRANSIENT RATES

by

Deep Chatterjee

A Dissertation Submitted in
Partial Fulfillment of the
Requirements for the Degree of

Doctor of Philosophy
in Physics

at

The University of Wisconsin-Milwaukee
May 2020

ABSTRACT

HARBINGERS OF EXOTIC TRANSIENTS: THE ELECTROMAGNETIC FOLLOW-UP OF GRAVITATIONAL-WAVE TRANSIENTS & TRANSIENT RATES

by

Deep Chatterjee

The University of Wisconsin-Milwaukee, 2020
Under the Supervision of Professor Patrick Brady

Gravitational waves (GWs) provide a unique view of the universe. They directly probe the extreme gravity and extreme matter of compact objects like black holes (BHs) and neutron stars (NSs) which is not always possible from traditional electromagnetic (EM) wave astronomy. The cataclysmic coalescence of compact object binaries is one of the loudest individual sources of GWs that can be detected by the Laser Interferometer Gravitational wave Observatory (LIGO) and the Virgo Observatory. If one of the component is a NS, there is a possibility that the merger is *bright* in the EM spectrum. The relativistic astrophysics could launch a short *gamma-ray burst*, the radioactivity in the neutron rich ejecta could power a rapidly decaying optical transient called a *kilonova*. Hence, it is possible to jointly observe the same source via multiple messengers. It is this prospect of multi-messenger astronomy using GWs that is of great interest due to the rich science that can be extracted from such joint observations. In this thesis, I present the details of my work with the LIGO Scientific Collaboration and Virgo Collaboration in the context of multi-messenger astronomy. I also report my work on the time-domain astronomy front in the development of an observing strategy for the Zwicky Transient Facility (ZTF), and characterizing the detection efficiency of the intermediate Palomar Transient Factory (iPTF).

© Copyright by Deep Chatterjee, 2020
All Rights Reserved

To my parents,
my late grandmother,
and my fiancée.

TABLE OF CONTENTS

1	The Story So Far	1
1.1	Advanced LIGO and Advanced Virgo	2
1.1.1	The First & Second Observing Runs	3
1.1.2	2017: The Dawn Of Multi-messenger Astronomy	3
1.1.3	The Third Observing Run	5
1.2	The Time-Domain Sky	7
1.3	Organization Of Thesis	8
2	Multi-messenger Astronomy With Gravitational Waves	10
2.1	Compact Binary Coalescences	10
2.1.1	GWs in Linear Approximation	11
2.1.2	Evolution Of The Orbit	13
2.1.3	Interaction With Detectors	17
2.2	High Energy Astrophysics From Compact Objects	20
2.2.1	Gamma-ray bursts	20
2.2.2	Supernovae	24
2.2.3	Kilonovae	29
2.3	GW170817	30
3	Low Latency Inference Of EM Counterparts From LIGO-Virgo	32
3.1	Motivation	32
3.2	Ellipsoid Based Inference	36
3.2.1	Low-latency Searches	36
3.2.2	Capturing Detection Uncertainties	38
3.3	Machine Learning Based Inference	39
3.3.1	Injection Campaign	42
3.3.2	Training Features and Performance	44
3.3.3	ROC Curve	49
4	Sky Tiling For The Zwicky Transient Facility	52
4.1	Tiling Strategies	54
4.1.1	The Contour-covering Strategy	54
4.1.2	The Ranked Tiling Strategy	55
4.2	Contour Covering vs. Ranked Tiling	57
4.3	Depth vs. Coverage	62

5	Toward Rate Estimation For Transient Surveys	67
5.1	Motivation & Challenges	67
5.2	The intermediate Palomar Transient Factory	70
5.3	Single-epoch Efficiency	70
5.3.1	Point Source Transients	71
5.3.2	Recovery Criteria	73
5.3.3	Marginalized Efficiency	75
5.3.4	Single Parameter Efficiencies	75
5.3.5	Multi-dimensional Detectability	75
5.4	Type Ia Supernova	79
5.4.1	Explosion Models	80
5.4.2	The SALT2 Model	80
5.4.3	Lightcurve Ensemble	81
5.4.4	SN Ia Lightcurves	82
5.4.5	SN Ia Detectability	85
5.4.6	SN Ia Space-time Sensitive Volume	85
5.5	Other Transient Lightcurves	87
5.5.1	Type IIp Supernova Lightcurves	87
5.5.2	Kilonova Lightcurves	89
5.6	Rates	91
5.6.1	Likelihood Calculation	91
5.6.2	Rate Posterior	91
5.6.3	Approximate SN Ia Count in iPTF	93
5.6.4	Future Work	93
6	Conclusion	94
6.1	Future Work	95
6.1.1	Machine Learning	95
6.1.2	EoS Weighted Source Properties	96
6.1.3	Supernova Rates	96
6.2	Looking Ahead	96
A	Behavior Of Trained Classifier With SNR	98
A.1	Parameter Sweep	98
A.2	GstLAL Injection Sets	98
B	Single Epoch Performance	101
	Bibliography	103
	Curriculum Vitae	115

LIST OF FIGURES

1.1	Aerial views of the Advanced LIGO and Advanced Virgo detectors.	2
1.2	Binary neutron star inspiral range of LIGO/Virgo in the third observing run.	6
1.3	GCN notice timeline related to GW170817 in the few hours post discovery.	7
2.1	Sketch showing a binary orbit.	14
2.2	Sketch showing interaction of GWs with test masses.	17
2.3	Sketch illustrating relativistic beaming.	21
2.4	Example of variation of luminosity with time for type II supernova homologous expansion model of Arnett (1980).	26
2.5	Example of variation of luminosity with time for type I supernova homologous expansion model of Arnett (1982).	27
2.6	Lightcurve evolution of AT 2017gfo using best fit blackbody parameters.	30
3.1	Detection uncertainty of masses and spins from the GstLAL search pipeline.	37
3.2	Qualitative illustration of the binary classification treatment of calculating <code>HasNS</code> and <code>HasRemnant</code> source properties.	39
3.3	Correlation matrix of the recovered parameters from the dataset used to train the supervised binary classifier.	44
3.4	Predictions of the trained binary classifier upon performing a parameter sweep on the (m_1, m_2) values.	45
3.5	receiver operating characteristic curve for the classifier	50
4.1	Planned tile locations for ZTF	55
4.2	Comparison between ranked tiles and contour-covering tiles.	58
4.3	Comparison of sky area searched to cover 90% of the sky localization to the searched area to find the source.	59
4.4	Performance of different tiling strategies on the First Two Years dataset.	59
4.5	Cumulative histogram of coverage fraction as a function of number of tiles covered according to various tiling methods.	60
4.6	Depth vs. coverage for ranked tiling strategy for ZTF.	62
4.7	Detection fraction as a function of the integration time per pointing.	63
4.8	Detection fraction as a function of the integration time per pointing.	64
4.9	Detection fraction as a function of the integration time per pointing.	65
4.10	Maximum detectability fraction as a function of integration time required to reach this fraction.	66

5.1	Example fake injected transient and the corresponding difference image. . .	71
5.2	Cumulative histogram of the quantity Θ_{IQ} defined in Eq.(5.4).	74
5.3	Marginalized single-epoch efficiencies of iPTF.	76
5.4	Comparison of single parameter efficiency predicted by trained single-epoch classifier vs. original distribution.	77
5.5	Example SALT2 lightcurve, and its detection by iPTF.	83
5.6	SN Ia recovery skymap as a function of cosmological redshift.	84
5.7	SN Ia recovery efficiency as a function of cosmological redshift.	84
5.8	SN IIP time series lightcurve (texttt Nugent-sn2p) and its detection by iPTF.	88
5.9	AT 2017gfo blackbody lightcurve model and its detection by iPTF.	89
5.10	AT 2017gfo recovery skymap as a function of cosmological redshift	90
A.1	Extension of Fig. 3.4 to all parameters used in training.	99
B.1	Extention of Fig. 5.4 showing predicted marginalized efficiency across all parameters.	102

LIST OF TABLES

2.1	The table lists the subcategories of SNe I/II and the basis of such a classification. The content is taken from Table 13.1 of Longair (2011).	25
3.1	Number and population of injections used in the training of supervised binary classifier.	41
3.2	True-positive and false negative of the trained binary classifier using a threshold of $p(\text{HasNS}/\text{HasRemnant}) = 0.5$ to classify systems.	47
3.3	Example values of true positive and false positive numbers for changing values of the threshold used in Fig. 3.5.	49
4.1	Performance of the different tiling strategies.	61
5.1	Average mis-classification of the single-epoch classifier.	78
A.1	Calender times for GstLAL injection datasets.	100

ACKNOWLEDGEMENTS

This is LIGO document number P2000128, available at the LIGO DCC.¹ I carried out this work being a part of the LIGO Scientific Collaboration (LSC), the intermediate Palomar Transient Factory (iPTF), and Zwicky Transient Facility (ZTF) collaborations. The work for Chapter 3 is supported by National Science Foundation (NSF) grant no. PHY-1607585, PHY-1626190, PHY-1700765, and PHY-1912649. I acknowledge the use of computing resources of the LIGO Data Grid and facilities provided by Leonard E. Parker Center for Gravitation, Cosmology, and Astrophysics (CGCA) at the University of Wisconsin-Milwaukee (UWM). The work for Chapter 5 is supported by Global Relay of Observatories Watching Transients Happen (GROWTH) project under NSF grant no. 1545949. The research used resources of the National Energy Research Scientific Computing Center (NERSC) supported by the Office of Science of the U.S. Dept. of Energy under Contract No. DE-AC02-05CH11231. I also acknowledge the use of computing facilities provided by CGCA and the UWM High Performance Computing (HPC) services.

The (almost) five years in Milwaukee have gone by before I realized. But it has contributed a lot to my understanding of physics, and the current state of research in gravitational-wave (GW) astronomy and astrophysics. It has been a unique experience being a part of the first few years of discovery of what may become (in some sense it already has) routine GW astronomy. Part of my reason to pursue graduate school in the U.S. was the graduate level coursework offered in most U.S. universities which is something I thoroughly enjoy. While my research is broadly in astronomy/astrophysics, I have taken the advantage of the breadth of courses offered at UWM. I would like to thank the UWM physics faculty for the amazing graduate level coursework. A few of my favorite lectures were those in GW astrophysics and data analysis by Jolien Creighton, stellar/high-energy astrophysics by David Kaplan/Phil Chang, statistical field theory by Daniel Agterberg, quantum field theory by John Friedman/Phil Chang, and general relativity by Patrick

¹ <https://dcc.ligo.org/LIGO-P2000128>

Brady. Also, in particular, thank you Alan Wiseman for the amazing two-semester course on electromagnetism. I am still able to commit from memory (and probably be able to in future) the expression,

$$\frac{1}{|\mathbf{x} - \mathbf{x}'|} = \sum_{lm} \frac{4\pi}{2l + 1} \frac{r_{<}^l}{r_{>}^{l+1}} Y_{lm}^{*'} Y_{lm}.$$

I am grateful to my doctoral advisor, Patrick Brady, for guiding me during this time, for giving novel ideas in research, giving a sense of where the field is headed, supporting me to travel to (many) conferences and face-to-face meetings, and giving me the freedom to work. I am also grateful to Jolien Creighton and David Kaplan for co-advising me during this time, and for being the go-to people for research related queries. Indeed, the last few years of the second and third observing runs have been *super*-eventful.

I would like to thank Shaon Ghosh, who overlapped with me in space, time, and research in both GW and astronomy front. Thank you for being a mentor and an amazing colleague. There are several work/personal experiences that come to memory, including the morning frenzy of August 17, 2017.² I would like to thank Leo Singer, working with whom I learned several computational tools, tricks, and best practices which will be useful in my future career. I would like to thank Shasvath Kapadia for the work in the low-latency classification we shared during the third observing run. For the work related to iPTF, I would specially like to thank Chris Cannella for all the help and conversations, work and otherwise, while at Caltech during the inception of the work in Chapter 5. I would also thank Mansi Kasliwal for hosting me during my visit, Peter Nugent for the guidance at every step of the project, Lin Yan, Uli Fiendt and Angie Van Sistine for helpful discussions.

Thank you Siddharth Mohite, Brandon Piotrkowski, Logan Prust, Satyanshu Kumar, Chandramouli Banerjee, Ignacio Magaña, Chaoran Zhang, Alex McEwen, Casey McGrath, Ian Brown, Caitlin Rose, Christian Horst, Christian Parsons, Dan Murray for being amazing people around me for work/fun related everything. I would like to thank Adil Amin, for being a great friend and roommate for the last four years, always willing to be ears

²The first merging binary neutron star GW170817 was discovered on this day.

when needed. I will miss the late night working on problem sets, getting pizza at Sal's, the amazing coffee at Eighth Note coffee house and the entertaining conversations there. I would like to thank my *peeps* – Ashani Dasgupta, Bapun K Giri, Mrinmayi Kulkarni, and Sarwat Sharif – for the friendship and support. Let's say, we have been in it together.

I would like to thank the UWM physics and CGCA staff for making it unknowingly easy to navigate certain steps related to travel and communication with the administration. In particular, thank you Heidi Matera for all your help in travel related complexities and otherwise.

Finally, I would like to thank my parents, Debasish and Suchita, for their constant support, love, advice, inspiration, and for always emphasizing to strive for excellence. Last but not the least, I would like to thank my long time friend and now fiancée, Sanchari Datta, for being through thick and thin, and (more importantly) for sheltering me during the ongoing COVID-19 pandemic, which finds me stuck in-shelter in Dallas, TX to finish writing up this thesis.

... A good question is, of course, the key by which infinite answers can be deduced ...

Isaac Asimov, *Foundation's Edge*

মহাবিশ্বে মহাকাশে মহাকাল-মাবে

আমি মানব একাকী ভ্রমি বিশ্বয়ে, ভ্রমি বিশ্বয়ে।

(In the midst of vastness of the Universe, and eternal time,
I the human alone wander in wonder.)

রবীন্দ্রনাথ ঠাকুর, *গীতবিতান*

(Rabindranath Tagore, *Geetobitan*)

“... Forget all this talk about ‘deflection’ and ‘force of gravitation.’ I am in a spaceship ... Do I feel any ‘force of gravitation’? Not at all ... Then why talk about it? Recognize that the spaceship and I traverse a region of spacetime free of all force ...”

The student from MTW (pp. 5 of [Misner et al., 1973](#))

Chapter 1

The Story So Far

In 1916 Albert Einstein published his relativistic theory of gravity – general relativity (GR) ([Einstein, 1916](#)). That light should bend around massive objects was the first prediction of GR to be verified by Arthur Eddington and his team ([Dyson, Eddington, & Davidson, 1920](#)). In 1916 Einstein also showed that GR allowed wavelike solutions which he called gravitational waves. He estimated the strength of these waves and noted that there was no scope to detect them with the available technology at the time. It took about 40 years for scientists to understand the physical nature of gravitational waves. [Peters & Mathews \(1963\)](#) first calculated the gravitational radiation from a binary star system. The discovery of the binary pulsar PSR1913+16 by [Hulse & Taylor \(1975\)](#), and continued observation of its orbital decay by [Taylor & Weisberg \(1989\)](#) provided compelling indirect evidence damping caused by gravitational-wave emission as predicted by GR for a binary orbit. The 1993 Nobel Prize in physics was awarded to Hulse and Taylor for this discovery.

Experimental efforts to directly measure gravitational waves were first attempted using resonant mass bar detectors by [Weber \(1960\)](#). Unfortunately, the sensitivity of these detectors was far from what would be needed to capture astrophysical sources. The idea of laser interferometry for this purpose was first reported by [Gertsenshtein & Pustovoit \(1963\)](#). In 1972 Rainer Weiss presented an experimental design of an “electromagnetically



Figure 1.1 Aerial views of the Advanced LIGO and Advanced Virgo detectors. Each of the LIGO detectors have 4 km long arms. The Virgo detector has 3 km long arms. The long arms house a modified Michelson interferometer to detect gravitational waves. From left: LIGO Hanford, LIGO Livingston, and Virgo. Figures credits: www.ligo.org & www.virgo-gw.eu.

coupled broadband gravitational antenna”¹ that eventually led to the construction of the Laser Interferometer Gravitational-wave Observatory (LIGO).² Initial LIGO started operations in the mid 2000s, with an upgrade to Advanced LIGO commissioned in 2015. Almost after a century since the initial prediction, gravitational waves from a binary black hole (BBH) merger were directly observed by the twin LIGO detectors in 2015 ([Abbott et al., 2016c](#)). The 2017 Nobel Prize in Physics was awarded to Rainer Weiss, Kip Thorne, and Barry Barish for the inception of LIGO and their contribution to the observation of gravitational waves.

1.1 Advanced LIGO and Advanced Virgo

The U.S. based, 4 km long, initial LIGO detectors were approved in the 1990s and finished construction over the early years of the turn of the century. The French-Italian, 3 km long, initial Virgo detector was also approved and constructed in a similar time frame. The initial LIGO and Virgo detectors jointly analysed data between 2005–2007 in what is known as the fifth science run (S5) for LIGO, and Virgo Scientific Run (VSR1) for the Virgo detector ([Abadie et al., 2010](#)).³ The detectors reached GW strain sensitivities $\sim 10^{-21}$, with LIGO at a distance sensitivity of $\gtrsim 30$ Mpc for a pair of $1.4M_{\odot}$ optimally

¹<https://dcc.ligo.org/LIGO-P720002/public>

²<https://dcc.ligo.org/LIGO-M890001/public>

³Previous observing runs S1–S4 was performed only by the LIGO detectors.

oriented binary neutron star (BNS) system. The Virgo detector reached a horizon distance of $\simeq 8$ Mpc for the same. Expectedly, based on the rate estimates of such binary mergers, no gravitational waves were detected with the initial observatories. The detectors were upgraded to Advanced LIGO (aLIGO) (Aasi et al., 2015) and Advanced Virgo (AdV), (Acernese et al., 2014) with almost an order of magnitude improvement in overall strain sensitivity, and better sensitivity to lower frequencies of GW inspiral at the start of its observing runs.

1.1.1 The First & Second Observing Runs

Advanced LIGO began its first observing run (O1) in September 2015. On September 14, 2015 at 09:50:45 UTC, the twin LIGO detectors observed, for the first time, GWs from a BBH merger at ~ 400 Mpc (Abbott et al., 2016c). This observing run saw two more stellar-mass BBH mergers, GW151012 and GW151226. The AdV detector was in commissioning period during this time.

The second observing run for aLIGO was conducted from November 30, 2016 to August 25, 2017. AdV started its observations in August 2017. This observing run saw the detection of 10 confirmed BBH mergers. This was a sharp increase since O1. It also saw the first ever gravitational-wave detection from the coalescence of a BNS, GW170817 (Abbott et al., 2018). Electromagnetic (EM) counterparts in the forms of gamma-rays (GRB 170817A), optical and radio/X-ray (AT 2017gfo) afterglows were observed concordantly from the source in a timeframe of seconds to months, even years after the merger (Abbott et al., 2017; Mooley et al., 2018; Hajela et al., 2019). The exhaustive observations carried out across EM and high-energy spectrum were unprecedented. It bore proof to the decade-long hypothesis that merging compact objects are progenitors of high-energy astrophysical phenomena like GRBs and kilonovae (Lattimer & Schramm, 1974; Li & Paczyński, 1998).

1.1.2 2017: The Dawn Of Multi-messenger Astronomy

The hypothesis that compact object collisions could create the environment for launching high-energy astrophysical phenomena is not recent. In 1974, [Lattimer & Schramm](#) had proposed that NS-BH mergers had the potential to tidally break the neutron star, and create the environment for launching a short GRB. In 1998, [Li & Paczyński](#) hypothesized a rapidly evolving (~ 1 day) optical transient, a kilonova,⁴ associated with merging binary neutron stars (BNS). Almost four decades after the initial hypothesis, the detection of photons in conjunction with gravitational waves (GWs) from GW170817 gave the first observational evidence of the hypothesis.

Joint observations in astronomy have been performed before. A notable one being the observation of neutrinos from the core-collapse supernova, SN 1987A, where the optical counterpart was observed a few hours after the detection of neutrinos by the Kamiokande-II and the Irvine-Michigan-Brookhaven detectors on February 23, 1987. The follow-up operations for GW170817 was, however, unprecedented. It was the first success story of the long effort to jointly observe both GW and EM emission from astrophysical sources. During O2, LIGO/Virgo had memoranda of understanding with 88 groups across more than 20 countries to follow-up GW candidates. Infrastructure was set up to exchange information over the Gamma-ray Coordinate Network (GCN)⁵ to enable multimessenger observations of astrophysical events. This included machine readable notices to provide automated follow-up opportunities to robotic ground and space-based facilities. Basic information about the discovered GW candidate, like the inferred time of merger, participating instruments, sky localization, probability of having a NS, or some remnant matter post merger was provided with the notices. The O2 follow-up campaign was a comprehensive effort in astronomy and astroparticle physics.

The participating facilities employed a variety of observing strategies. All-sky searches

⁴Originally called a *macronova*. The more modern term *kilonova* was coined by [Metzger et al. \(2010\)](#).

⁵<https://gcn.gsfc.nasa.gov/>

were performed by high-energy instruments, and neutrino detectors. These used spatio-temporal information about the GW candidate to match internal databases about potential candidates near the trigger time. Wide field surveys used tiling, and/or galaxy catalog targeted searches based on the GW sky localization distributed with the notices. Deep field/spectroscopy instruments pursued medium latency follow-up operations post identification of candidates. Long term follow-up was done in X-ray and radio. In case of GW170817, such operations continued for over a year. A complete description of the O2 LIGO/Virgo EM follow-up campaign is given in [The LIGO Scientific Collaboration et al. \(2019\)](#). The discovery of GW170817 heralded a new era in organized joint observational efforts in EMGW astronomy. It showcased the rich science that is possible by studying multiple messengers from the same source (see Sec. 2.3 for a brief summary of the scientific impact). It gave the impetus to the current efforts in multi-messenger astronomy.

1.1.3 The Third Observing Run

The LIGO/Virgo third observing (O3) run started on April 1, 2019. The observing run came to an end on March 27, 2020.⁶ For the first time, the LIGO/Virgo candidate discoveries were broadcasted publicly over the GCN.⁷ Several improvements were made to the detectors during the break between O2 and O3. The volume averaged BNS inspiral was ~ 140 Mpc for L1, ~ 120 Mpc for H1, and ~ 50 Mpc for V1. A total of 56 GW candidates have been reported publicly. This is more than a five-fold increase compared to events from O1 & O2 combined. Also, the duty cycle of the detectors have improved significantly with at least two detectors being operational for $\gtrsim 80\%$ of this run duration, and three detectors being so $\sim 50\%$ of the duration (see Fig. 1.2). This produced some extremely well localized candidates in O3.^{8 9} Additional data products were provided to aid follow up

⁶Scheduled to end on April 30, 2020. However, detector operations were suspended on March 27, 2020 due to ongoing COVID-19 pandemic situation.

⁷<https://emfollow.docs.ligo.org/userguide/>

⁸<https://gracedb.ligo.org/superevents/S200311bg/view/>

⁹<https://gracedb.ligo.org/superevents/S190814bv/view/>

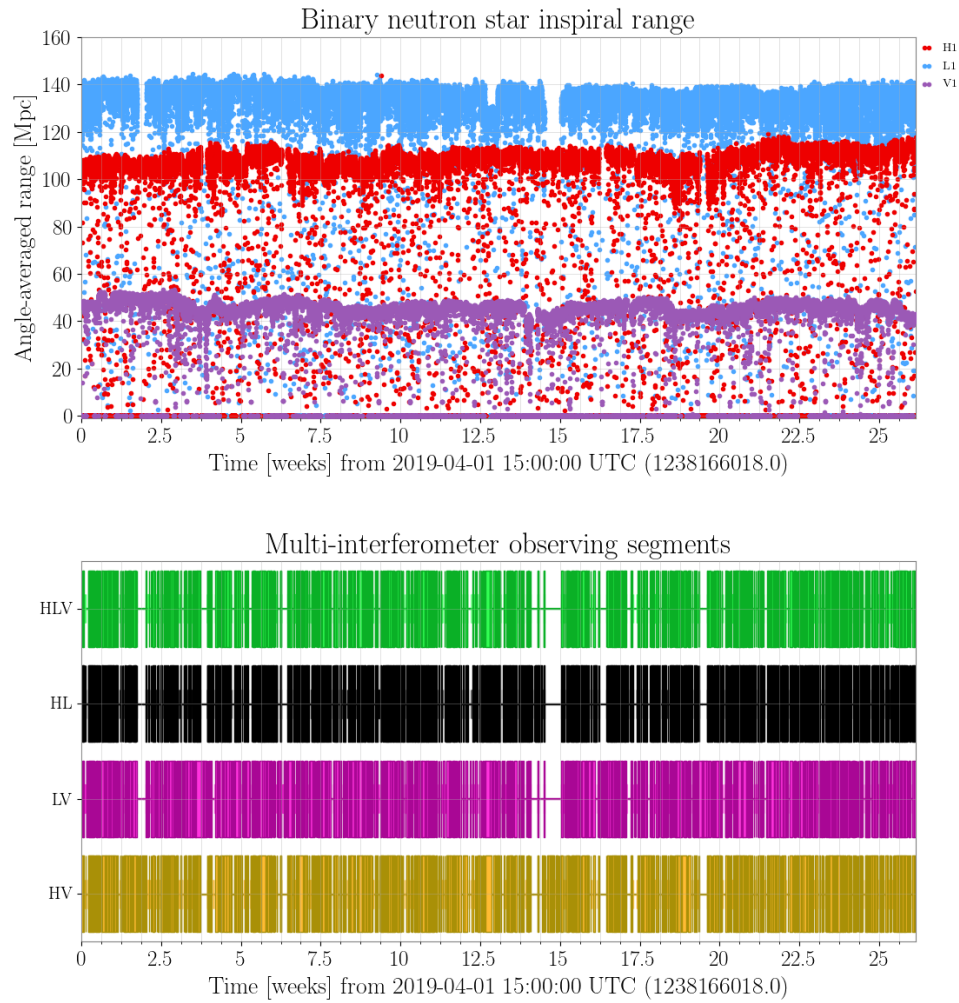


Figure 1.2 **Upper panel:** This figure shows the angle and volume averaged inspiral range for binary neutron star (BNS) systems for the first half of the LIGO/Virgo third observing run (O3). **Lower panel:** Coincident detector observation durations. Credits: LIGO detector characterization summary (<https://ldas-jobs.ligo.caltech.edu/~detchar/summary/>).

operations. Also, the distribution of alerts, and their latency improved significantly with the usage of new tools, and allocation of more resources for this purpose.

1.2 The Time-Domain Sky

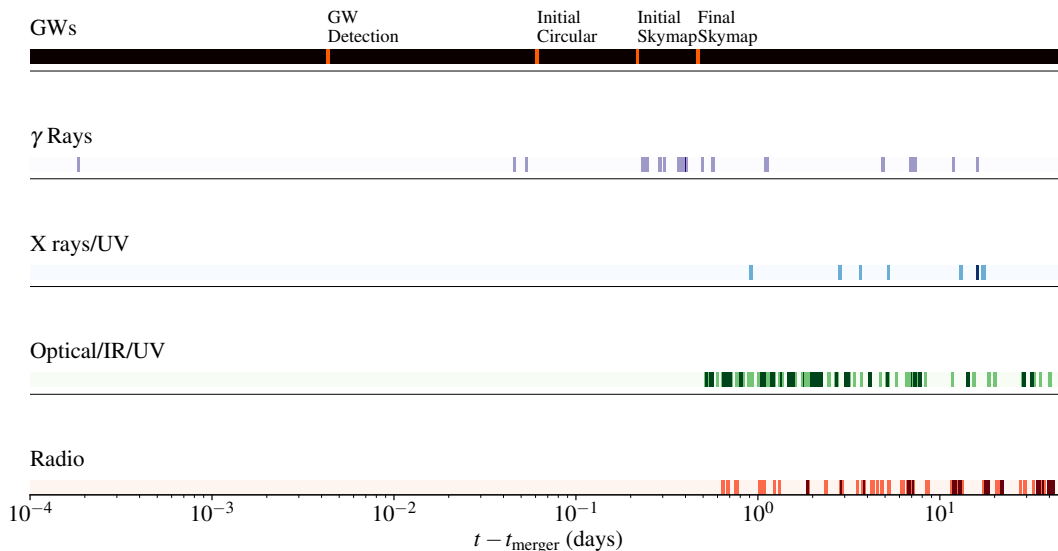


Figure 1.3 A timeline of GCN notices following the hours after the merger of the binary neutron star (BNS) system, GW170817, the discovery of concordant gamma-rays, GRB 170817A, and the optical and near infrared counterpart, AT 2017gfo.

Simultaneous with the development of ground based GW detectors, the last two decades have brought about a revolution in the field of time-domain optical astronomy with experiments like Pan-STARRS, (Kaiser et al., 2010) Sloan Digital Sky Survey, (Sako et al., 2007) the ATLAS survey, (Shanks et al., 2015) the Catalina survey, (Drake et al., 2009) the All-Sky Automated Survey for Supernovae, (Holoien et al., 2019) the Palomar and intermediate Transient Factory (PTF), (Law et al., 2009) and Zwicky Transient Facility (ZTF) (Kulkarni, 2016) performing all sky searches with rolling cadence to locate transients. Next generation surveys like Vera Rubin Observatory (Ivezić et al., 2008) are expected to make significant additions to already existing catalogs with wide-deep-fast searches. Current and upcoming telescope facilities are consistent with the timeline of LIGO/Virgo operations,

and plan to participate in the follow-up efforts of GW sources (see [Graham et al. \(2019\)](#), for example).

The impact of such time-domain, robotic surveys have been significant in discovering transients. Thousands of supernovae, for example, have been added to the catalogs, and new classes of transients are being discovered. Among the latter are fast radio bursts, fast X-ray transients, superluminous supernovae, and kilonovae to name a few. Many such transients have compact object progenitors. GWs can accompany, or be precursors of their progenitor dynamics. This goes beyond the sources being observed by the ground based GW network today. Current pulsar timing experiments, like the North American Nanohertz Observatory for Gravitational Waves (NANOGrav) ([Jenet et al., 2009](#)), will be able to probe the regime of GW emission from supermassive BH inspirals. The Laser Interferometer Gravitational-wave Antenna (LISA) ([Amaro-Seoane et al., 2017](#)) will be able to probe their mergers. Future ground based detectors will be able to see BNS mergers out to high redshifts ($z \gtrsim 1$). GW parameter estimation along with photometric and spectroscopic data will be invaluable to infer the high energy astrophysics of the compact object. High redshift multi-messenger astronomy will be crucial for future cosmological observations. Therefore, the synergy between EM and GW facilities is an exciting prospect in the coming decade.

1.3 Organization Of Thesis

We have reached an era when GW detection is routine. It is possible to do astronomy with them. Joint detections requires robust infrastructure to deliver candidate information and data products to external partners to carry out follow-up observations. Along with better detectors, the requirement of computing resources and cyber infrastructure is also increasing. So is the need for new and efficient algorithms to handle this stream of astrophysical data. Among others, the prospects of using of machine learning is increasingly appar-

ent to enable future discoveries. In this thesis I present my work with the LIGO/Virgo collaborations and the ZTF collaboration to allow multi-messenger astronomy.

The organization of the thesis is as follows. In Chapter 2, I discuss sources of GWs, and the principle of detecting them using laser interferometry. I briefly review some EM counterparts possible from compact objects – GRBs, supernovae and kilonovae. In Chapter 3, I give details about the low-latency source property estimation of LIGO/Virgo compact binary coalescences (CBCs). The source properties provide a realtime inference of the CBC having a counterpart and is a part of the realtime notices circulated by LIGO/Virgo during the previous and current operations. In Chapter 4, I give details about a tiling strategy for the ZTF telescope used in the follow-up operations of the GW sources. In Chapter 5, I give details about characterizing the detection efficiency of transient surveys considering the intermediate Palomar Transient Factory (iPTF) as a case study. The detection efficiency is the missing piece in the determination of transient rates from archival data. Conclusions and the roadmap ahead is presented in Chapter 6.

Chapter 2

Multi-messenger Astronomy With Gravitational Waves

2.1 Compact Binary Coalescences

Compact binary coalescences (CBCs) are one of the loudest sources of GWs that can be detected by the advanced ground based GW detectors today. The frequency evolution is between few tens to few hundred Hz. By compact objects, we refer to neutron stars and black holes. Although white dwarfs are also compact objects, such mergers are not observable by ground based detectors since their frequency evolution does not lie in the sensitive frequency band of the ground-based detectors. In this section we give order of magnitude estimates of quantities like the frequency evolution, time to coalescence, total flux, frequency evolution and so on. Also, a brief description of the interaction of the ground based interferometers with incoming GWs is presented. It should be mentioned that to model the binary inspiral accurately in the strong gravity regime, higher order post-newtonian corrections have to be taken into account. Finally, black-hole perturbation theory and numerical relativity simulations are needed to capture the merger and ringdown phase.

2.1.1 GWs in Linear Approximation

The emission of GWs from a system causes a perturbation, $h_{\mu\nu}$, in the spacetime. In the linear approximation and assuming propagation of waves over a flat spacetime, the spacetime metric is written as,

$$g_{\mu\nu} = \eta_{\mu\nu} + h_{\mu\nu}, \quad (2.1)$$

where $\eta_{\mu\nu} = \text{diag}(-c^2, +1, +1, +1)$, is the flat spacetime metric. The expression for the metric perturbation, to first order, is given by (see, for example, Chapter 3 of [Creighton & Anderson, 2011](#)),

$$h_{ij}^{\text{TT}}(t) = \frac{2G}{c^4 r} \ddot{I}_{ij}^{\text{TT}}(t - r/c), \quad (2.2)$$

where G is the gravitational constant, c is the speed of light, r is the distance to the source and I_{ij} is the quadrupole moment of the mass distribution, ρ , producing the GWs given by,

$$I^{ij} = \int x^i x'^j \rho(t - r/c, x') d^3 x'. \quad (2.3)$$

The superscript “TT” denotes the *transverse-traceless* gauge where the metric perturbation can be written in the form of Eq. (2.2). The coordinate freedom of the GR field equations guarantees that such a gauge exists. The metric perturbation can be transformed into this gauge after being evaluated in some other coordinate system. In what follows, we will assume this gauge, i.e., the metric perturbation is transverse to the direction of propagation and is traceless and avoid the “TT” superscript. This result of Eq. (2.2) is of primary importance, which says GW radiation in GR is produced by a time varying mass quadrupole moment of the source, unlike EM radiation where a time varying electric dipole moment of charge distribution can produce radiation. The retarded time in the right hand side of Eq. (2.2) is due to the propagation at the speed of light over a distance r . The energy flux

carried by GW is given by (Isaacson, 1968a,b),

$$\frac{dE_{\text{GW}}}{dt dA} = -\frac{c^3}{32\pi G} \langle \dot{h}_{ij} \dot{h}^{ij} \rangle \quad (2.4)$$

$$= -\frac{G}{8\pi c^5 r^2} \langle \ddot{I}_{ij} \ddot{I}^{ij} \rangle, \quad (2.5)$$

where the $\langle \dots \rangle$ denotes integration over several GW wavelengths. The GW luminosity is given by,

$$L_{\text{GW}} = -\frac{dE_{\text{GW}}}{dt} = \frac{G}{5c^5} \langle \ddot{I}^{ij} \ddot{I}_{ij} \rangle. \quad (2.6)$$

For order of magnitude calculations, we will drop the pre-factors and write Eqs. (2.2, 2.6) as,

$$h \sim \frac{G}{c^4 r} \ddot{I}, \quad (2.7)$$

$$L_{\text{GW}} \sim \frac{G}{c^5} \ddot{I}^2. \quad (2.8)$$

Applying the above expression for, say, a $1.4 - 1.4M_{\odot}$ BNS system at 40 Mpc, emitting GWs at 100 Hz (orbiting each other at $\omega_{\text{orb}} = 50\text{Hz}$), orbital separation $a = \sqrt[3]{GM/\omega_{\text{orb}}^2} \sim 150\text{km}$, we have,

$$\begin{aligned} h &\sim \frac{G}{c^4 r} M a^2 \omega_{\text{orb}}^2 \\ &\sim 10^{-22} \end{aligned} \quad (2.9)$$

This is an optimistic detection scenario given the $\sim 10^{-23}$ strain sensitivity of the current detectors around ~ 100 Hz regime. The luminosity emitted is,

$$L_{\text{GW}} \sim 10^{51} \text{ erg s}^{-1}. \quad (2.10)$$

This is an estimate of the luminosity at a fixed frequency. It is insightful to cast the expression in a slightly different form using, $\ddot{I} \sim Mv_{\text{orb}}^2/T \sim Mv_{\text{orb}}^3/a$ in Eq. (2.8),

$$L_{\text{GW}} \sim \frac{G}{c^5} \left(\frac{M}{a}\right)^2 v_{\text{orb}}^6 \quad (2.11)$$

$$\sim \left(\frac{c^5}{G}\right) \left(\frac{GM}{c^2 a}\right)^2 \left(\frac{v_{\text{orb}}}{c}\right)^6 \quad (2.12)$$

$$= (3.6 \times 10^{51} \text{erg s}^{-1}) \left(\frac{\kappa}{0.1}\right)^2 \left(\frac{v_{\text{orb}}}{0.1c}\right)^6 \quad (2.13)$$

Here, $T \sim a/v_{\text{orb}}$ is the typical time scale of the dynamics of the quadrupolar component of motion, and a is the typical length scale of the system. The quantity, $\kappa = (GM/c^2 a)$, is the compactness of the system. The upper limit being, $\kappa \approx 0.5$, corresponding to a BH. This form shows the two essential ingredients required for efficient GW emission – compact systems, moving at a fraction of the speed of light. Also note that the pre-factor, $(c^5/G) = 3.6 \times 10^{59} \text{erg s}^{-1}$, is a fundamental upper limit of GW luminosity from any system. In case, the system is in virial equilibrium, like a binary orbit, $GM/a = v^2$, which changes Eq. (2.12) to,

$$L_{\text{GW}} \sim \left(\frac{c^5}{G}\right) \left(\frac{v_{\text{orb}}}{c}\right)^{10}. \quad (2.14)$$

2.1.2 Evolution Of The Orbit

Consider a binary system as shown in Fig. 2.1. The masses are assumed to be point mass systems. The orbit is assumed to be circular.¹ The expression for the instantaneous GW luminosity is given by (see Section 3.5 of [Creighton & Anderson, 2011](#)),

$$L_{\text{GW}} = \frac{32}{5} \eta^2 \left(\frac{c^5}{G}\right) \left(\frac{v}{c}\right)^{10}, \quad (2.15)$$

¹Eccentric orbits increase the emitted GW luminosity but the qualitative features are unchanged.

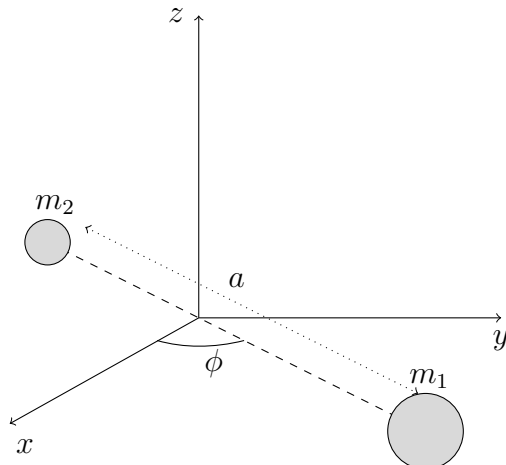


Figure 2.1 Figure showing a binary orbit. The primary (secondary) mass labeled as m_1 (m_2). The orbital separation is denoted by a , with the center of mass at the origin of the coordinate system. The orbit is assumed to be circular.

where $\eta = m_1 m_2 / (m_1 + m_2)^2$, is the symmetric mass ratio of the system, which has a maximum value of 0.25. The total energy of the system is,

$$E = -GM\mu/2a, \quad (2.16)$$

$$= -\mu v_{\text{orb}}^2/2, \quad (2.17)$$

where, $M = (m_1 + m_2)$, $\mu = m_1 m_2 / (m_1 + m_2)$, and $v_{\text{orb}} = a\omega_{\text{orb}}$, are the total mass, reduced mass, and orbital velocity respectively. As the binary orbit shrinks, $\{E, v\} \rightarrow -\infty$, with $L_{\text{GW}} = -dE/dt$. This gives the time to coalescence,

$$t_c = \frac{5}{32\eta} \frac{GM}{c^3} \int_{v_0/c}^{\infty} \frac{d(v_{\text{orb}}/c)}{(v_{\text{orb}}/c)^9} \quad (2.18)$$

$$= \frac{5}{256\eta} \frac{GM}{c^3} \left(\frac{\pi GM f_{\text{GW}}^0}{c^3} \right)^{-8/3}. \quad (2.19)$$

Here, $v_0 = \pi f_{\text{GW}}^0 a$ is an arbitrary starting value of the orbital velocity, corresponding to a starting GW frequency f_{GW}^0 . The fundamental mode of GW frequency is twice the orbital frequency, $f_{\text{GW}} = 2f_{\text{orb}}$. Thus, the $1.4 - 1.4M_{\odot}$ BNS system emitting GWs $\simeq 100$ Hz,

considered in the previous section, will coalesce is ≈ 2.16 s. However, if the same system is considered starting at $\simeq 30$ Hz, the time to coalescence ≈ 1 minute. The frequency evolution as a function of time can be evaluated using,

$$\frac{df_{\text{GW}}}{dt} = \frac{df_{\text{GW}}}{dv} \frac{dv}{dt} \quad (2.20)$$

$$= \left(\frac{3v}{G\mu M\pi} \right) \left(-\frac{dE}{dt} \right) \quad (2.21)$$

$$= \frac{96}{5} \pi^{8/3} \left(\frac{G\mathcal{M}_c}{c^3} \right)^{5/3} f_{\text{GW}}^{11/3}. \quad (2.22)$$

where the newtonian expression, $f_{\text{GW}} = 2f_{\text{orb}} = v_{\text{orb}}^3/GM\pi$, and Eq. (2.17) has been used in the first line. The quantity, $\mathcal{M}_c = (m_1 m_2)^{3/5}/(m_1 + m_2)^{1/5}$, is the *chirp mass* of the system, and determines the phase evolution of the orbit. Integrating Eq. (2.22),

$$f_{\text{GW}}(t) = \frac{1}{\pi} \left(\frac{5}{256} \right)^{3/8} \left(\frac{c^3}{G\mathcal{M}_c} \right)^{5/8} \frac{1}{(t_c - t)^{3/8}}. \quad (2.23)$$

This shows the *chirping* behavior where the frequency increases rapidly as one approaches coalescence. The GW phase is,

$$\varphi_{\text{GW}}(t) = \int_t^{t_c} 2\pi f_{\text{GW}}(t') dt' \quad (2.24)$$

$$= 2\varphi_c - \left[2 \left(\frac{c^3(t - t_c)}{5G\mathcal{M}_c} \right)^{5/8} \right], \quad (2.25)$$

where φ_c is the coalescence phase of the orbit. Laser interferometry is primarily sensitive to the phase, and the above equation shows that at newtonian order, the chirp mass, \mathcal{M}_c , is the only parameter of the system that be extracted from the phase.

Spectrum of CBCs

The frequency domain evolution of the GW signal from a CBC is important from a data analysis perspective. Many matched filtering techniques use frequency domain waveform

families to search for signals. The newtonian chirp waveform, as a function of time is given by,

$$h(t) = a_{\text{GW}}(t) \times \cos[\varphi_{\text{GW}}(t)] \quad (2.26)$$

$$= \left[\frac{G\mathcal{M}_c}{c^2 r} \left(\frac{5G\mathcal{M}_c}{c^3(t_c - t)} \right)^{1/4} \right] \times \cos \left[2\varphi_c - 2 \left(\frac{c^3(t_c - t)}{5G\mathcal{M}_c} \right)^{5/8} \right]. \quad (2.27)$$

The frequency domain evolution is obtained via a fourier transform,

$$h(f) = \int_{-\infty}^{+\infty} h(t) \exp[2\pi i f t] dt \quad (2.28)$$

$$= \int_{-\infty}^{+\infty} a_{\text{GW}}(t) \exp[i\psi(t)] dt, \quad (2.29)$$

where, $\psi(t) = 2\pi i f t \pm \varphi_{\text{GW}}(t)$. Consider the quantity, $x = G\mathcal{M}_c/c^3$, appearing in Eq. (2.27). For typical stellar mass binaries, $x \sim 10^{-6} - 10^{-5}$ s. This is much smaller compared to typical $(t_c - t)$ values, which are $\sim 10^{-3} - 10$ s. The amplitude in Eq. (2.27) goes as $\sim [(t_c - t)/x]^{-1/4}$, while the phase goes as $\sim [(t_c - t)/x]^{5/8}$. Hence, the phase is a faster oscillating function compared to changes in the amplitude. The integral can then be evaluated using saddle point approximation as,

$$h(f) = \int_{-\infty}^{+\infty} a(t_{\text{sp}}) \exp i \left[\psi(t_{\text{sp}}) + \frac{1}{2}(t - t_{\text{sp}})^2 \ddot{\psi}(t_{\text{sp}}) \right] dt \quad (2.30)$$

where $\dot{\psi}(t_{\text{sp}}) = 0$ at $(t_c - t_{\text{sp}}) = (4\pi f/5)^{-8/3} (c^3/5G\mathcal{M}_c)^{5/3}$. This gives,

$$h(f) = \left[a_{\text{GW}}(t_{\text{sp}}) \left(\frac{2\pi}{\ddot{\varphi}_{\text{GW}}(t_{\text{sp}})} \right)^{1/2} \right] \exp \left[-\frac{i\pi}{4} + i\psi(t_{\text{sp}}) \right] \propto f^{-7/6} \quad (2.31)$$

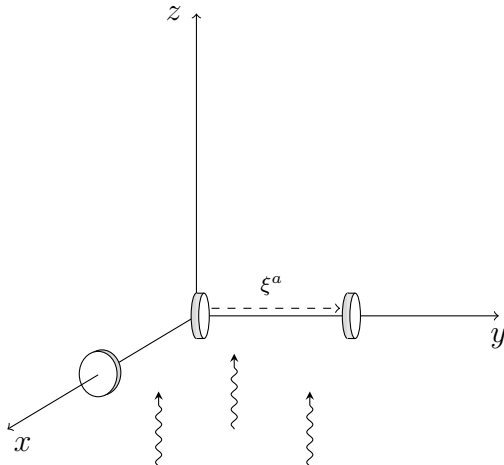


Figure 2.2 The figure shows plane GWs propagating along the z -axis, with two test particles, believed to be test masses along the y -axis. The strain induced in the test masses is given by Eq.(2.39). A third test mass is also shown along the x -axis in reference to the typical setup of the Michelson interferometer.

2.1.3 Interaction With Detectors

Gravitational waves have the physical effect of causing strain in materials they pass through. In case of ground-based detectors like LIGO/Virgo, this is measured by the interference pattern in a modified Michelson interferometer (see Fig. 2.2 for an illustration). In order to see the effect, consider a plane GW passing along the z -axis. The metric perturbation, in terms of the two GW polarizations, h_+ and h_\times , is written as,

$$h_{\mu\nu} = \begin{pmatrix} 0 & 0 & 0 & 0 \\ 0 & h_+ & h_\times & 0 \\ 0 & h_\times & -h_+ & 0 \\ 0 & 0 & 0 & 0 \end{pmatrix}. \quad (2.32)$$

The line element looks like,

$$ds^2 = -c^2 dt^2 + (1 + h_+) dx^2 + (1 - h_+) dy^2 + 2h_\times dx dy + dz^2. \quad (2.33)$$

The strain induced by the GW is like a tidal effect i.e., a relative displacement, caused due to geodesic deviation in the presence of GWs. An observer at the origin of Fig. 2.2 sees the relative motion between oneself and the nearby geodesics of the other test masses via equation of geodesic deviation given by,

$$\frac{d^2\xi^i}{dt^2} = -R^i{}_{0j0}\xi^j. \quad (2.34)$$

The relevant terms in the Riemann curvature tensor are,

$$R^0{}_{101} = -\frac{1}{2}\ddot{h}_+ \quad (2.35)$$

$$R^0{}_{102} = -\frac{1}{2}\ddot{h}_\times. \quad (2.36)$$

Consider a plane wave incident on a pair of test particles, as shown along the y -axis of Fig. 2.2. These could be thought of as test masses of ground-based GW detectors with a displacement vector, $\xi^i = (0, 0, L, 0)$, between them. The equation of motion due to the GWs is,

$$\ddot{\xi}^y(t) = -R^2{}_{010}\xi^1 - R^2{}_{020}\xi^2 \quad (2.37)$$

$$= -\frac{1}{2}\ddot{h}_+(t)L \quad (2.38)$$

$$\Rightarrow \xi^y(t) = \left(1 - \frac{1}{2}h_+(t)\right)L, \quad (2.39)$$

where t is the proper time measured by the observer moving with the test mass. In the strict sense, the test masses in ground based detectors are not in free fall, since they are suspended via wires to compensate for earth's gravity. But considering motion in the horizontal plane, they are almost in free fall.²

A typical ground-based GW interferometer consists of a Michelson interferometer as

²There are certainly, non stationary noise sources like thermal noise, shot noise, violin modes to name a few.

shown in Fig. 2.2. The light propagates along null geodesics along the arms. Considering only the + polarization and propagation along the y-axis, we have,

$$dt = \pm \left(\frac{1}{c}\right) \left(1 - \frac{1}{2}h_+\right) dy, \quad (2.40)$$

where the \pm corresponds to the to and from travel from the origin respectively. The cavity is sensitive in the regime where the time period of the GWs is much smaller than the round trip light travel time, $2\pi/\omega_{\text{GW}} \ll 2L/c$. In other words, the wavelength of the GWs is much larger than length scale of the detectors. The typical wavelengths of the GW ~ 100 Hz is $\sim 10^3$ km, which is much larger than the \sim km long arms of the current detectors. Thus, the metric perturbation is almost constant during the round trip of the light. Integrating Eq. (2.40), the light travel time is,

$$\Delta t = \frac{2L}{c} - \frac{L}{c}h_+. \quad (2.41)$$

Thus, the path difference attributed due to the GW is,

$$c\Delta t = \Delta L = -h_+L, \quad (2.42)$$

$$\Rightarrow \frac{\Delta L}{L} = -h_+. \quad (2.43)$$

The path length $2L/c$ in Eq. (2.41) is canceled by interference with light from the other arm of the Michelson interferometer, along the x -axis in Fig. 2.2. Hence, the GW strain is directly obtained from the phase readout of the cavity. Note that in reality the Michelson interferometer setup is more complex and Fig. 2.2 is simply an illustration. ³

³See <https://www.ligo.caltech.edu/page/ligos-ifo> for a more realistic illustration.

2.2 High Energy Astrophysics From Compact Objects

Several EM transient phenomena, like supernovae, pulsars, gamma-ray bursts, fast radio bursts, are associated with compact objects. As discussed in the previous chapter, compact object mergers can be luminous in EM spectrum in the presence of matter post merger. The dynamics of matter in the violent aftermath of a merger can launch various messengers. In this section, some of the EM counterparts relevant for this thesis are discussed in brief. The high-energy astrophysics is complex. Only a brief overview is presented here, with pointers to review articles in the literature.

2.2.1 Gamma-ray bursts

Gamma-ray Bursts (GRBs) were discovered serendipitously in the 1960s by the *Vela* satellites that aimed to watch over nuclear tests being performed on a terrestrial site (Klebesadel et al., 1973). Routine discoveries were made by the Burst and Transient Source Experiment (BATSE) instrument in the 1990s. As the name suggests, GRBs are bursts of gamma rays with peak energies in the few hundred keV to \sim MeV having a duration $\sim 10^{-2}$ s to $\sim 10^5$ s. Bursts with duration $<$ ($>$) 2s are categorized as short (long) GRBs. Observed fluences range between 10^{-4} erg cm $^{-2}$ to 10^{-7} erg cm $^{-2}$. The total energy output is comparable to supernovae, $\sim 10^{51}$ erg, but it is emitted in few tens of seconds. The physics of the bursts are an area of research, but it is widely accepted that such bursts involve highly relativistic material, with Lorentz factor, $\Gamma = 1/\sqrt{1 - v^2/c^2} \sim 100$. The radiation comes primarily from synchrotron emission, and from inverse compton scattering of the photons.

Regarding their progenitors, the long GRB population is connected to massive star origin. They are typically associated with type Ic supernovae, and reside in star forming host galaxies. On the other hand, the short GRB population is characterized by the absence of a supernova association. Their host galaxies range from early-type to star-forming galaxies. Their offset from the galaxy core is much larger compared to long GRBs,

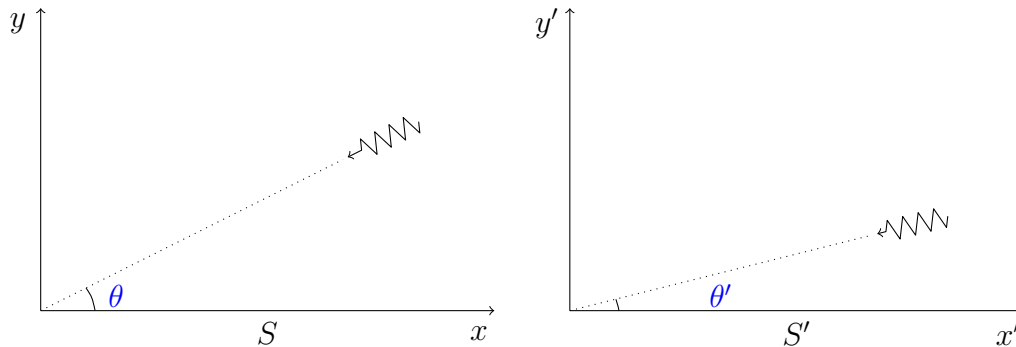


Figure 2.3 Consider a photon emitted by a source in the proper frame, denoted by S , at an angle θ . The S' observer moves at a constant velocity v along the x . The angle at which the moving observer sees the photon is θ' . In case of ultra-relativistic velocities, the angle $\theta' \approx 1/\Gamma$, where $\Gamma = \sqrt{1 - v^2/c^2}^{-1/2}$. The frame S could be interpreted as the rest frame of an electron where it gives off radiation at an angle θ . In the lab frame, the observed angle of radiation is at θ' . Hence, radiation emitted isotropically in the proper frame, can be observed as being beamed.

or supernovae. The median redshift of short GRBs is $z \sim 0.48$, as compared to the median redshift of $z \sim 2$ for the long GRB population (Berger, 2014). Although hypothesized decades back (see Sec. 1.1.2), observation of GRB170817A as a counterpart of GW170817 gave the observational evidence that merging NSs are progenitors of at least some short GRBs. Although other possibilities like NSBH mergers, rotational energy of magnetars, accretion induced collapse of proto NSs are possible (Narayan et al., 1992; Metzger et al., 2008; Bernardini, 2015). These facts make the short GRB population an interesting case to study. Their association with merger of compact binaries make them a MMA candidate for gamma-ray detectors. The association with afterglows in the X-ray, optical and radio make them candidates for corresponding telescopes. In this section, a review of the basic physics of GRBs are presented. Most of the material is adapted from Piran (2005); Longair (2011); Gehrels & Mészáros (2012).

Relativistic Beaming

A key ingredient of GRBs is the doppler beaming of the radiation. This is a characteristic of ultra-relativistic motion, and can be illustrated in a few steps. Consider the situation in Fig. 2.3. Here, a photon emitted by a source at an angle θ in the proper frame is observed at an angle θ' by an observer moving with velocity v towards the source (or source moving towards observer as a corollary), represented by S' . For example, S can be considered to be a frame that is instantaneously at rest with a radiating charge, that is otherwise moving with respect to the laboratory, a typical situation for a synchrotron radiation. The amount of beaming is obtained using the velocity addition formula,

$$u'_x = \frac{u_x - v}{1 - u_x v/c^2}, \quad (2.44)$$

$$u'_y = \frac{1}{\Gamma} \frac{u_y}{1 - u_x v/c^2}. \quad (2.45)$$

Using $(u_x, u_y) = -c(\sin \theta, \cos \theta)$ for the photon velocity in S , and $(u'_x, u'_y) = -c(\sin \theta', \cos \theta')$ in S' , we get the angles,

$$\sin \theta' = \frac{1}{\Gamma} \frac{\sin \theta}{1 + \beta \cos \theta}, \quad (2.46)$$

$$\cos \theta' = \frac{\cos \theta + \beta}{1 + \beta \cos \theta}, \quad (2.47)$$

where $\beta = v/c$, and $\Gamma = 1/\sqrt{1 - \beta^2}$. In the limit of $\Gamma \gg 1$, the first equation above gives,

$$\theta' \sim 1/\Gamma. \quad (2.48)$$

This gives the important result that for a radius R giving off radiation, the observer sees the radiation from a size $\sim R/\Gamma$.

Relativistic Jet

In case of BNS or NSBH mergers, the central engine post merger (likely BH) would launch a burst of intense radiation from energy of the in-falling material left behind from the aftermath. Part of this material is accreted, while a larger fraction is ejected in a jet along the rotation axis in $\sim 5 - 10$ degree angular extent. The rotating debris could also extract rotational energy of the BH via the [Blandford & Znajek \(1977\)](#) mechanism. The interaction of the jet with the external material results in dissipation of the kinetic energy into a non-thermal spectrum of acceleration changes that emit via synchrotron radiation.

Synchrotron Radiation

Charged particles are accelerated during the dissipation of kinetic energy due to internal shocks in the expanding material, or external shocks with the circumburst medium. The prompt GRB comes from the former, while the afterglows are from the latter. Particles are accelerated as they repeatedly cross a shock. The radiation is emitted primarily via synchrotron radiation. For a relativistic electron, the spectrum goes as (see Sec. 8.4 of [Longair, 2011](#)),

$$F_e(\nu) \propto \begin{cases} \nu^{1/3} & ; \nu < \nu_c \\ \exp(-\nu/\nu_c) & ; \nu > \nu_c \end{cases}, \quad (2.49)$$

where the critical frequency, $\nu_c \approx \Gamma_e^2 \nu_g$, is the frequency at which maximum power is emitted. Here, $\nu_g = eB/2\pi m_e$ is the non-relativistic gyro-frequency of the electron. The complete spectrum depends on how the relativistic electrons are distributed. A power law distribution of electron energy is generally considered,

$$N(E)dE \propto E^{-p}dE. \quad (2.50)$$

The spectrum for a single electron, given in Eq. (2.49) along with the distribution of relativistic electrons, determine the observed spectra. It turns out that the lower energy part of the spectrum is independent of the distribution of relativistic electrons. Higher energy electrons deposit most of their energy near the synchrotron frequency, $\nu_c \propto \Gamma^2 \propto E^2$. Hence, the population of electrons at that energy will contribute to the spectrum. We have,

$$F_{\text{sync}}(\nu) \propto \begin{cases} \nu^{1/3} & ; \nu < \nu_c \\ \nu^{-p/2} & ; \nu > \nu_c. \end{cases} \quad (2.51)$$

Short Gamma Ray Bursts

The duration of the GRBs detected by the BATSE instrument fell into two distributions – the fewer short GRBs around ~ 0.2 s and the long GRBs around ~ 20 s, with a boundary at ~ 2 s. The advent of the Swift Observatory (Gehrels & Swift Team, 2005) made significant addition to the short GRB population, and identifying host galaxies. The discovery of GW170817 gave the first observational evidence that binary neutron star mergers are the progenitors of at least some short GRBs. GRB 170817 A was, however, slightly different from the typical short burst. The spectrum was much softer with $E_{\text{peak}} = 185 \pm 62$ keV, and a best-fit spectral index, $\alpha = -0.62 \pm 0.40$ (Goldstein et al., 2017). Values from the BATSE short GRB sample are $\langle E_{\text{peak}} \rangle = 355 \pm 30$ keV and $\langle \alpha \rangle = -0.58 \pm 0.10$ (Ghirlanda et al., 2004). Afterglows of short GRBs were detected in the X-rays, optical, NIR and radio bands starting from the Swift era. However, multi-band afterglow observations are needed to understand the properties, like jet opening angles. The study of short GRBs, its afterglows, and the possibility of simultaneous GW detection make it an ideal candidate for multi-messenger astronomy.

Type	Characteristics
Ia	absence of hydrogen; presence of silicon lines
Ib	absence of hydrogen; presence of helium lines
Ic	absence of hydrogen and helium lines; weak silicon lines
IIP	has a plateau in light curve
IIL	has a linear decrease in light curve
IIn	has narrow features compared to usual broad emission features in spectra
Ilb	has SN II properties at early times, and SN Ib/c properties at late times

Table 2.1 The table lists the subcategories of SNe I/II and the basis of such a classification. The content is taken from Table 13.1 of Longair (2011).

2.2.2 Supernovae

Many interesting high energy astrophysics originate from stellar endpoints. The endpoint of nuclear burning in massive stars $\gtrsim 8M_{\odot}$ is associated with stellar collapse to form a neutron star, or a black hole. The collapse may be associated with release of large bursts of energy $\sim 10^{53}$ erg, known as supernovae (SNe). Their occurrence is more frequent than the other high-energy astrophysical phenomena mentioned here. Time domain surveys today, discover thousands of SNe in their typical few years duration. The most recent, closest one is SN 1987A that exploded in the Large Magellanic Cloud in 1987 (see Sec. 1.1.2).

Supernovae are traditionally classified as Type I (SNe I) or Type II (SNe II). The SNe II are characterized by the presence of hydrogen Balmer lines in the optical spectrum at maximum light, while the SNe I do not. Further subdivisions are tabulated in Table 2.1. Later in the thesis, detection efficiency of supernova lightcurves are computed. In this section, we highlight the important features of their lightcurves.

Core Collapse Supernovae

The endpoint of stellar burning of a massive star is an iron core $\sim 1.4M_{\odot}$ at a temperature of about $\sim 10^9$ K. Photo-disintegration of iron nuclei and inverse beta decay can trigger the onset of collapse of this iron core. Order of magnitude estimates of the energy release can be obtained from assuming the initial configuration of the core to have a radius of ~ 1000

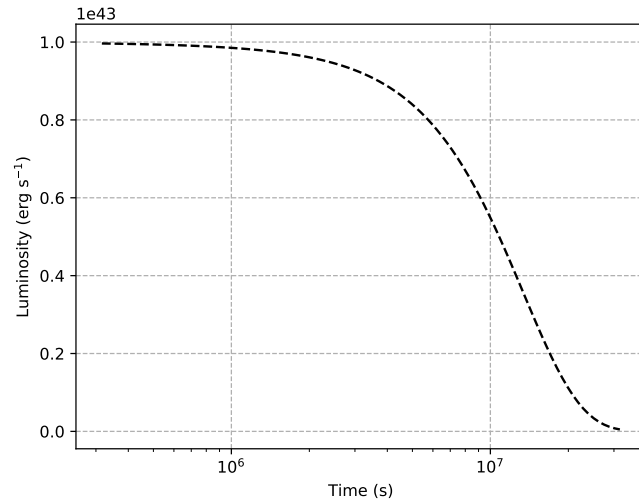


Figure 2.4 Variation in luminosity with time for the homologous expansion model, uniform opacity and density of Arnett (1980). The time variation is given by Eq. (2.54). The value of τ_m determines the decay of the supernova. Values for this plot are $L_0 = 10^{43} \text{ erg s}^{-1}$, $\tau_0 = 10^8 \text{ s}$, $\tau_m = 10^7 \text{ s}$.

km, and the final compact object having a radius of $\sim 10 \text{ km}$. The net energy released is almost equal to the gravitational binding energy of the final remnant,

$$E_{\text{bind}} \sim GM^2/R \quad (2.52)$$

$$= (5 \times 10^{53} \text{ erg}) \left(\frac{M}{1.4M_{\odot}} \right)^2 \left(\frac{R}{10 \text{ km}} \right)^{-1}. \quad (2.53)$$

The neutrinos produced by the inverse beta decay escape carrying 99% of the energy of a supernova resulting in optical energies $\sim 10^{51} \text{ erg}$. The gravitational collapse of the iron core is suddenly halted by the formation of a proto-neutron star. The *bounce* caused due to this shock expels the outer layers of the star. The end result is a deposition of the $\sim 10^{51} \text{ erg}$ near the center of the star, followed by a blast wave. The expanding layer can be modeled as homologous expansion. The evolution is determined from the radiative processes and thermodynamics of the expanding ejecta. Analytic models for the time evolution exists for simple model of the opacity. For example assuming a constant density and opacity, the

time evolution is given by (Arnett, 1980),

$$L_{\text{SN}}(t) = L_0 \exp \left[- \left(\frac{t}{\tau_0} \right) - \left(\frac{t}{\tau_m} \right)^2 \right]. \quad (2.54)$$

where τ_0 is the diffusion time, and $\tau_m = \sqrt{2\tau_0 R_0 / v_{\text{sc}}}$, R_0 being the initial radius of the ejecta, and v_{sc} the expansion velocity assumed to be constant. Typical values are $L_0 \sim 10^{43} \text{erg s}^{-1}$, $\tau_0 \simeq 10^8 \text{s}$, $v_{\text{sc}} = 1000 \text{km s}^{-1}$, giving $\tau_m \simeq 10^7 \text{s}$. An example of the time evolution with the typical values is shown in Fig. 2.4. There is a lot of variability in the SNe II lightcurves due to various additional physics. In Chapter 5, SNe Iip lightcurve are analyzed in more detail with respect to their detection efficiency by time domain surveys.

Type Ia

SNe Ia are produced due to thermonuclear detonation of carbon-oxygen white dwarfs with masses close to the Chandrasekhar limit of $\sim 1.4M_{\odot}$. Fusion reactions of carbon and oxygen are associated with intermediate elements like silicon, all the way up to ^{56}Ni . Silicon is found in the spectra near maximum light. The ^{56}Ni is converted into ^{56}Co via electron capture which eventually decays into ^{56}Fe . The later part of the light curve shows an exponential decay consistent with the radioactive decay of the ^{56}Ni and ^{56}Co . For SNe Ia the nuclear burning of carbon is ignited explosively either at the center of the star, or different spots off-center. Following which, the burning occurs in thin shells and propagates conductively as subsonic deflagrations, or via shock compression as supersonic detonations (Hillebrandt & Niemeyer, 2000). Best fit models predict an initial deflagration phase up to a density of $\sim 10^7 \text{g cm}^{-3}$, after which the detonations become dominant.

Like the case of SNe II, the ejecta can be simply modeled as homologous expansion. However, the difference from the SNe II case is the presence of a radioactive heating source which determines the decay of the lightcurve. Arnett (1982) considered a model predominantly heated by ^{56}Ni decay. The early phase of the luminosity shows a $L_{\text{SN}} \propto t^2$

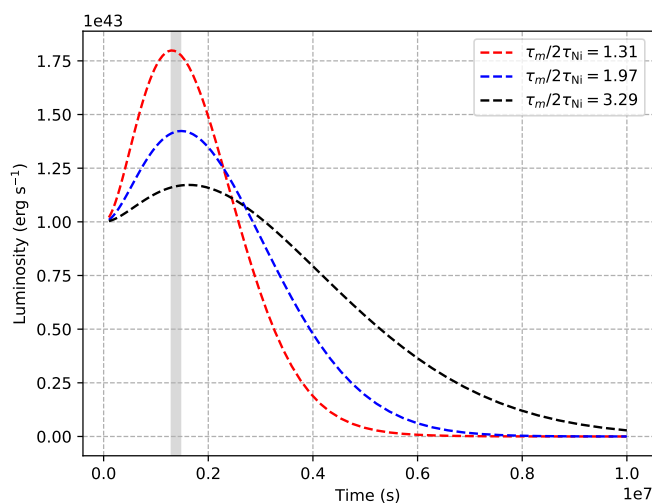


Figure 2.5 This figure shows a plot for the time variation of luminosity for a typical [Arnett \(1982\)](#) model. The 15–17 day region, which is the typical peak time for the SN Ia, is shaded. Three cases of diffusion times, controlled by the parameter τ_m (see Eq. (2.54)) are shown. Larger diffusion time increases both the time to maximum light and width of the lightcurve.

rise. For later times, decay is exponential $L_{\text{SN}} \propto \exp(-t/\tau_{\text{Ni}})$, where $\tau_{\text{Ni}} = 7.605 \times 10^5 \text{s}$ is the half life of ^{56}Ni . Examples of luminosity time variation for the [Arnett \(1982\)](#) model is shown in Fig. 2.5. The maximum light occurs when diffusion losses equal the radioactive heating. Both width of the lightcurve, and time to maximum light increases with increasing values of τ_m , as defined in Eq. (2.54). A typical time variation in the luminosity for the ([Arnett, 1982](#)) model is plotted in Fig. 2.5. SNe Ia are one of the most luminous type of supernova, with absolute magnitudes ~ -19.5 . Although slight variations exist, the lightcurves are homogeneous. Hence, SNe Ia are used as distance indicators in cosmology. The detectability of the SNe Ia lightcurves for transient surveys is considered in Chapter 5.

GWs From Core-Collapse Supernovae

While compact binary mergers are one of the strongest individual sources of GWs in the universe, asymmetric core-collapse of a massive star could also generate GWs. Hence, SNe II could potentially be associated with GW emission. The signal strength, however,

is not as strong as compact object mergers, and current ground based detectors are only sensitive to such events occurring with our own galaxy. Current estimates of galactic SNe II rate is ≈ 3.2 per century and the last such event happened ~ 100 years back (Morozova et al., 2018). Hence, there are chances of getting another such event in this era of MMA. Various complex processes, like vibrational modes of the newly formed proto-neutron star (PNS), neutrino interactions, fluid instabilities, and shocks could drive the GW emission from a CCSNe. Abdikamalov et al. (2014) have shown that the last phase of collapse, bounce, and post bounce phase produces GW emission, $h \sim 10^{-21}$, for a source at ~ 30 kpc. This is a very optimistic detection scenarios for future LIGO/Virgo searches for unmodeled sources, with a prospect of detection of a multimessenger “trifecta” of GWs, EM and neutrinos (Pajkos et al., 2019).

2.2.3 Kilonovae

Merger of compact objects involving a NS, produces an isotropic EM emission called a kilonova. The peak luminosity is about $\sim 10^{41}$ erg s $^{-1}$, about 1/100th the peak luminosity of a typical supernova. The absolute magnitudes are $\simeq -15$ as opposed to $\simeq -19.5$ of a typical SN Ia. The lightcurve peaks in a timescale of \sim day. The merger ejects some matter with a sub-relativistic velocity. Following the merger there is rapid decompression of matter at nuclear density. Rapid neutron capture produces neutron rich heavy elements in the lanthanide family, many of them radioactive. The radioactive decay of such species is responsible for heating the ejecta. This is similar to the case for SN Ia, with a radioactive heating source,

$$\varepsilon = \frac{fc^2}{\tau_{\text{rad}}} \exp(-t/\tau_{\text{rad}}), \quad (2.55)$$

where f is the fraction of unit rest mass equivalent that is converted to energy. In this case, the solution is identical to the SN I case described above. However, since there are several species produces, the resultant heating is sum of the individual species. The

distribution of half lives for heavy elements, τ_{rad} is uniform in logarithmic intervals of time (Li & Paczyński, 1998). Thus, the effective heating source is,

$$\varepsilon_{\text{tot}} = \int \varepsilon(\tau_{\text{rad}})p(\tau_{\text{rad}})d\tau_{\text{rad}} \quad (2.56)$$

$$= \frac{fc^2}{t}, \quad (2.57)$$

where $\varepsilon(\tau_{\text{rad}})$ is given by Eq. (2.55), and $p(\tau_{\text{rad}}) \propto 1/\tau_{\text{rad}}$, is the distribution of half lives of different heavy element species. Later work, however, have established the heating rate to be a steeper power-law, $\propto 1/t^{-\alpha}$, where $\alpha \approx 1.1 - 1.4$ (Metzger, 2017). The basic ingredients for the model is similar to the SN Ia calculation above. In case of the heating term from a single species, like Eq. (2.55), the rise follows a $L \propto t^2$ dependence, while the fall follows the exponential decay of radioactive species, $L \propto \exp(-t/\tau_{\text{rad}})$.⁴ In case of the power-law heat source, the late time luminosity is follows the heat source i.e., $L \propto 1/t$ (or $L \propto 1/t^\alpha$). The diffusion timescale of photons is large due to the presence of heavy elements which interact strongly with the photons. The timescale is determined by the condition when the diffusion time decreases and becomes of the order of the expansion timescale. This occurs at ~ 1.6 days (Metzger, 2017), which is significantly less than that of supernovae.

2.3 GW170817

Due to the fast decay and low intrinsic brightness of the kilonova, their existence remained a mystery until the detection of AT 2017 gfo, which was discovered as an EM counterpart of the merger of two NSs, GW170817. On August 17, 2017, the advanced LIGO and advanced Virgo detectors observed GWs from a binary neutron-star (BNS) coalescence. This was shortly followed by a spatially and temporally coincident short GRB, named

⁴Note that the treatment by Arnett (1982) & Li & Paczyński (1998) is similar when considering a single species. In particular, Eq. 21 in Li & Paczyński (1998) is identical to Eq. 44 of Arnett (1982), showing the t^2 rise.

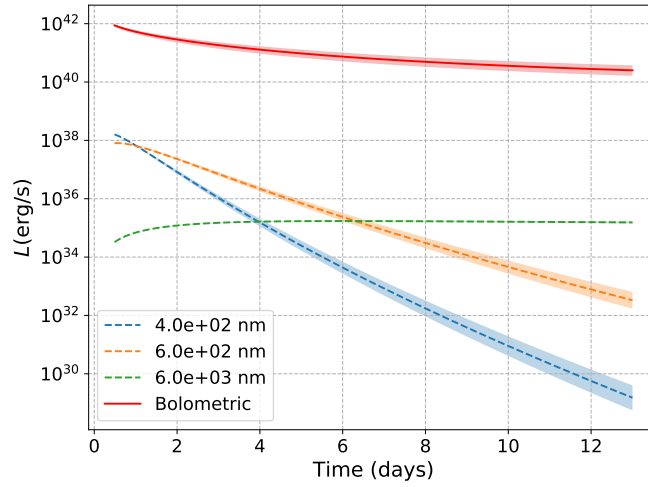


Figure 2.6 This figure shows the blackbody luminosity evolution of AT 2017gfo using the best-fit parameters from Kasliwal et al. (2017). The luminosity in three reference wavelengths are plotted. The transient evolved rapidly in the blue bands, with a slower evolution in the red bands.

GRB 170817 A. The association of the two gave the first observational evidence that BNS systems are progenitors of, at least, some short GRBs. Follow-up operations on this event were unprecedented across the EM spectrum, and led to the observation of AT 2017gfo. The multi-messenger operations on this event gave a wealth of knowledge in astrophysics and cosmology. Below are some of the important results.

- An independent measurement of the Hubble constant using the distance information from GW data, host galaxy information from EM data (The LIGO Scientific Collaboration et al., 2017).
- The off-center location constrained the progenitor of such binary systems (Abbott et al., 2017).
- Tidal deformability measurement of the neutron-stars, from GWs, was used to constraint the NS equation of state (Abbott et al., 2018). used to constraint the NS equation of state (Abbott et al., 2018).
- The photometry and spectroscopy of the kilonova constrained the jet and ejecta

properties.

Overall, this event was the first success story of the decade long effort towards joint detection of electromagnetic and gravitational wave signals. The kilonova AT 2017gfo evolved from a luminosity of $\simeq 10^{42}$ erg s $^{-1}$ at about 0.5 days to $\simeq 3 \times 10^{40}$ erg s $^{-1}$ in ten days. Effective blackbody temperature evolved from 1.1×10^4 K to about 1.4×10^3 K in ten days. The inferred ejected mass $\simeq 0.05M_{\odot}$ at a expansion velocity $\simeq 0.1c$. The infrared spectra shows the presence of lanthanide series elements, like Neodymium, synthesized via r -process (Kasliwal et al., 2017). The evolution of the luminosity based on a blackbody fit is shown in Fig. 2.6.

Chapter 3

Low Latency Inference Of EM Counterparts From LIGO-Virgo

This chapter is reproduced in part from [Chatterjee et al. \(2019a\)](#), which has been accepted for publication in The Astrophysical Journal. An online record can be found at <https://arxiv.org/abs/1911.00116>.

3.1 Motivation

The first two observing runs of the LIGO detectors, ([Aasi et al., 2015](#)) and the Virgo detector ([Acernese et al., 2014](#)) witnessed remarkable level of participation from the electromagnetic (EM) astronomy community in search for EM counterparts of gravitational wave (GW) detections from coalescing binaries ([The LIGO Scientific Collaboration et al., 2019](#); [Abbott et al., 2019](#)). As the detectors become more sensitive, the projected detection rates of such events will increase ([Abbott et al., 2018](#)). Technological improvement is not just confined to GW detectors alone. Current and upcoming telescope facilities such as the Zwicky Transient Facility ([Kulkarni, 2016](#)) and the Large Synoptic Survey Tele-

scope, (Ivezić et al., 2008) consistent with the timeline of LIGO/Virgo operations, plan to participate in the follow-up efforts (see Graham et al. (2019), for example).

Observers are interested to know about the presence of a neutron star (NS) in coalescing binaries. This is a minimum condition for there to be matter post merger. The dynamics of matter in the extreme environment of the aftermath of a compact binary merger is responsible for EM phenomena associated with GWs. Binary black hole (BBH) mergers, therefore, are not expected to have an associated counterpart, since they are vacuum solutions to the Einstein’s field equations. Even in the presence of a NS, other effects, like the equation of state (EoS) of the NS(s), or the mass and spin of the companion BH plays crucial role in the tidal disruption, and the amount of matter ejected. For a neutron star black hole (NSBH) system, tidally disrupted material from the NS could form an accretion disk around the central BH. High temperatures in the disk could lead to annihilation of neutrinos to pair produce electron-positrons, which further annihilate to power a short GRB. This could also happen via extraction of rotational energy from the BH due to the presence of magnetic field lines threading the BH horizon (Blandford & Znajek, 1977). In the case of unbound ejecta, *r*-process nucleosynthesis can power a *kilonova*. (Lattimer & Schramm, 1974; Li & Paczyński, 1998; Korobkin et al., 2012; Tanaka & Hotokezaka, 2013; Barnes & Kasen, 2013; Kasen et al., 2015) For a binary neutron star (BNS) system, even if the tidal interaction is not strong enough, the two bodies will eventually come into physical contact, resulting in shocks that expel neutron rich material. This will result in a kilonova as seen in the case of GW170817 (Abbott et al., 2017; Arcavi et al., 2017; Coulter et al., 2017; Kasliwal et al., 2017; Lipunov et al., 2017; Soares-Santos et al., 2017; Tanvir et al., 2017). The interaction of the ejecta with the surrounding medium can result in synchrotron emission, observable in X-rays and radio in weeks to months. There can be relativistic outflows, which could result in a GRB, as seen for GW170817; although, there could be cases of prompt collapse where GRB generation could be suppressed (Ruiz & Shapiro, 2017). Nevertheless, the generation of some EM messenger is highly probable. Therefore,

data products that predict the existence of matter is useful in the EM counterpart follow-up operations.

An accurate computation of the remnant matter requires general-relativistic numerical simulations of compact mergers. These are expensive, and only a few ($\lesssim 100$) such simulations have been performed to date. Also, such a simulation is not possible in the time scale of discovery, and generic target of opportunity follow-up of GW candidates. Empirical fits to the numerical relativity results, however, have been performed, and are a use case for such realtime inferences. For example, [Foucart \(2012\)](#) and [Foucart et al. \(2018\)](#) devised an empirical fit to predict the combined mass from the accretion disk, the tidal tail, and the ejecta remaining outside the final BH in case of a NSBH merger. However, it should be mentioned that such fits often require more input than what is available from the realtime GW data. For example, the fits mentioned above require the compactness of the NS, which is not a parameter inferred by the GW searches. The NS EoS, which is not constrained strongly, is to be assumed in order to infer the compactness.

The second LIGO/Virgo observing run, O2, saw the first effort to provide realtime data products to aid EM follow-up operations from ground and space based facilities ([The LIGO Scientific Collaboration et al., 2019](#)). These included sky localization maps, ([Singer & Price, 2016](#); [Singer et al., 2016a](#)) and source classification of the binary which included

1. the probability that there was at least one neutron star in the binary, $p(\text{HasNS})$, and
2. the probability that there was non-zero remnant matter, $p(\text{HasRemnant})$, considering the mass and spin of the components, based on the [Foucart \(2012\)](#) fit.

For a BNS merger, we expect some matter to be expelled (see Table 1 of [Shibata & Hotokezaka \(2019\)](#) for different scenarios). Therefore, we expect the result, $p(\text{HasNS}) = 1$; $p(\text{HasRemnant}) = 1$. On the other extreme, BBH coalescences will not lead to remnant matter, since they are vacuum solutions, i.e., $p(\text{HasNS}) = 0$; $p(\text{HasRemnant}) = 0$. Hence, $p(\text{HasRemnant})$ is more relevant for NSBH systems. Here, the mass and spin of the BH

determines the tidal disruption of the NS. Lower mass, and high spin implies a smaller innermost stable circular orbit which allows the NS to inspiral closer to BH. The tidal force exerted by the BH, which also increases with spin, then tears the NS apart. This leaves remnant matter post merger. However, if the NS is compact, or tidal forces are not sufficient enough, the NS is swallowed whole into the BH, leaving no remnant. The type and morphology of EM counterparts generated depends on the amount of matter ejected and its properties. [Pannarale & Ohme \(2014\)](#) considered the conditions for short GRB production in the context of LIGO/Virgo observations of NSBHs. More recent work has tried to understand the morphology of kilonovae from NSBH mergers considering the density structure of the ejected matter, opacity properties, the viewing angle, and other factors (see [Barbieri et al. \(2019\)](#); [Hotokezaka & Nakar \(2019\)](#), for example). However, accurate modeling is still at its infancy. Thus, the presence of remnant matter is a conservative proxy for the presence of counterparts, still more constraining than the presence of a NS component alone, albeit the model dependence i.e., the assumption of NS EoS, and the usage of a particular fit. The rationale behind computing two quantities is to give flexibility to observing partners in follow-up operations.

The main challenge in this inference, however, is to handle detection uncertainties in the parameter recovery of the realtime GW template-based searches. This was done in O2 via an effective Fisher formalism using an *ambiguity* region around the parameters of the triggered template. The algorithm used for O2 is described in Sec. 3.3.2 of [The LIGO Scientific Collaboration et al. \(2019\)](#), and briefly summarized in Sec. 3.2 below. While it accounted for statistical uncertainties, the systematic errors in the low-latency GW template based analysis were not considered. Here we consider the problem differently. We treat the problem as binary classification, and present a new technique that is based on supervised learning. This not only improves the speed and accuracy, but also removes runtime dependencies that were required during O2 operations. Also, this technique provides flexibility to incorporate astrophysical rates of binary populations in the universe.

In the third LIGO/Virgo observing run, O3, these data products (and a few more) continue to be part of the public alerts.¹ In this work, we make a slight modification to the nomenclature. The $p(\text{HasRemnant})$ quantity had been referred to as *EM bright* classification probability in [The LIGO Scientific Collaboration et al. \(2019\)](#). Here, we refer to the both these quantities collectively as *source properties*, following the O3 LIGO/Virgo public alert userguide. These values indicate the chances of the matter remaining post merger, the dynamics of which can launch EM counterparts. For example, the combination $p(\text{HasNS}) = 1; p(\text{HasRemnant}) = 0$, indicates a conservative measure of presence of matter – just the presence of NS. However, the combination $p(\text{HasNS}) = 1; p(\text{HasRemnant}) = 1$, is a stronger indication of the presence of a counterpart, albeit some model dependence.

The organization of the chapter is as follows. In Sec. 3.2 we provide a brief review of the ellipsoid-based inference used in O2. In Sec. 3.3, we present the inference using a supervised learning method called `KNeighborClassifier` ([Pedregosa et al., 2011](#)), which was trained on injection campaigns from the GstLAL search pipeline ([Messick et al., 2017](#)) used by LIGO/Virgo in routine search sensitivity analyses during O2. We test the performance of the machine learned inference.

3.2 Ellipsoid Based Inference

3.2.1 Low-latency Searches

LIGO/Virgo searches for transient GW signals fall into two broad categories: modeled compact binary coalescence (CBC) searches ([Adams et al., 2016](#); [Messick et al., 2017](#); [Chu, 2017](#); [Nitz et al., 2018](#); [Abbott et al., 2019](#)) and un-modeled burst searches ([Lynch et al., 2017](#); [Klimenko et al., 2016](#)). In this work, we are concerned with the former. The modeled searches use a discrete template bank of CBC waveforms to carry out matched filtering on the data. This is further broken down into realtime online analysis, and calibration

¹ <https://emfollow.docs.ligo.org/userguide/>

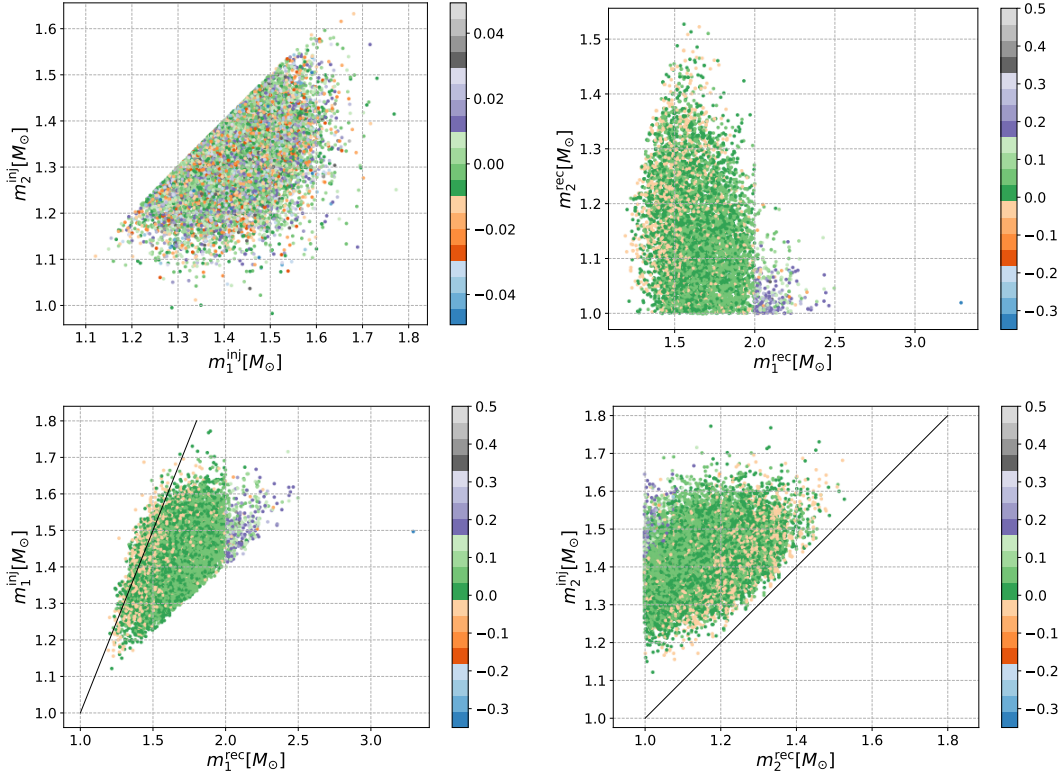


Figure 3.1 In this figure we compare the mass and spin recovery of one of the search pipelines, GstLAL (Messick et al., 2017), that meet the false alarm rate threshold of Eq.(3.2). **Upper panel:** This panel shows the (m_1, m_2) pairs of a gaussian distributed BNS population $\sim \mathcal{N}[1.33M_\odot, 0.09M_\odot]$ (see Table 3.1). The left plot shows the masses injected following a normal distribution, as mentioned in Table 3.1, colored by the injected primary aligned spin component, χ_1^z . The right plot shows the recovered masses colored by the recovered χ_1^z . It can be seen that the distribution in the recovered space is significantly different from the one in the injected space. One may also see that the recovered spin values may be higher than the injected ones, especially in the case of higher mass ratio recoveries. **Lower panel:** This panel shows the injected values of the primary and secondary masses against their recovered values for low-mass injections. This is an example where one can see the systematic effect of the primary mass being recovered at higher values than the injected values. The secondary follows the opposite trend: the recovered value is lesser than the injected values. The effect also exists at higher mass ranges. Both plots are colored by the recovered χ_1^z values. Note the recovered $m_1^{\text{rec}} > 2M_\odot$ (both panels) have higher values of recovered χ_1^z . This is because the GstLAL search uses templates with low spins for masses $\leq 2M_\odot$ and high spins above that (see Fig. 1 & 2 in Mukherjee et al. (2018) for example). Even values slightly higher than $2M_\odot$ may result in high spin values compared to the injections.

corrected offline analysis. The online low-latency searches report CBC events in sub-minute latencies. They use waveform templates that are characterized by masses, (m_1, m_2) , and the dimensionless aligned/anti-aligned spins of the binary elements along the orbital angular momentum of the binary, (χ_1^z, χ_2^z) . They report a best matching template based on an appropriate detection statistic. We call the parameters of this template, $\{m_1, m_2, \chi_1^z, \chi_2^z\}$, the *point estimate*. This data can be used for low-latency source property inference.

3.2.2 Capturing Detection Uncertainties

Since the source property inference is to be done based on the point estimates, the obvious pitfall in the inference is: How accurate are the point-estimates compared to the true parameters of the source? The primary goal of detection pipelines is to maximize detection efficiency at fixed false alarm probability. While some parameters like the chirp mass,

$$\mathcal{M}_c = (m_1 m_2)^{3/5} / (m_1 + m_2)^{1/5}, \quad (3.1)$$

on which the signal strongly depends, are measured accurately,² others like the individual mass or spin components are often inconsistent compared to the true parameters. Accurate parameter recovery is left to Bayesian parameter estimation analysis (Veitch et al., 2015; Ashton et al., 2019; Biwer et al., 2019).

Consider the case for the GstLAL search (Messick et al., 2017; Mukherjee et al., 2018; Sachdev et al., 2019) in Fig. 3.1. Here, we compare fake GW signals whose parameters we know a priori, to the recovered template i.e., point estimate, obtained from injecting the fake signals in detector noise and running the pipeline. Note that the recovered masses can sometimes be significantly different from the injected values, leading to an erroneous classification of the systems based on point-estimates alone. To alleviate this problem attempts were made to capture the uncertainty in the recovery of the parameters using

²More precisely, this is true for low-mass systems where the waveform is dominated by the inspiral phase. For heavier BBH systems, the total mass, $m_1 + m_2$, is recovered accurately.

an effective Fisher formalism (Cho et al., 2013). This method allows us to construct an ellipsoidal region of the parameter space around the point estimate that captures the uncertainty in the parameters under the Fisher approximation. This was used to create confidence regions in the parameter estimation code, RapidPE (Pankow et al., 2015) from which it was implemented in EM-Bright pipeline to construct 90% confidence regions in three dimensions – chirp mass, symmetric mass ratio and effective spin. This ellipsoidal region was populated uniformly with one thousand points (besides the original triggered point). The fraction of these ellipsoid samples which had $m_2 < m_{\max}^{\text{NS}}$ ³ constituted the $p(\text{HasNS})$ value, while the fraction that had non-vanishing disk mass, $M_{\text{disk}} > 0$ from the Foucart (2012) fit, constituted $p(\text{HasRemnant})$ value.

3.3 Machine Learning Based Inference

The method of uncertainty ellipsoids handles the statistical uncertainties of the parameters from the low-latency search pipelines. However, the underlying Fisher approximation is only suitable in the case of high signal to noise ratio, when the parameter uncertainties are expected to be Gaussian distributed (see Sec. II of Cutler & Flanagan (1994) for example). Also, it is not robust in capturing any bias that a search might have. Such trends are seen, for example, in Fig. 3.1 where the m_1 parameter is recovered to be larger than the injected value, while the m_2 parameter is recovered to be smaller.⁴

³ $m_{\max}^{\text{NS}} = 2.83M_{\odot}$ was used during O2 operations. This is the maximum allowed mass of a NS assuming the 2H EoS.

⁴In GW parameter estimation, m_1 refers to the primary (larger) mass component while m_2 refers to the secondary (smaller) mass component. Likewise, χ_1^z (χ_2^z) refers to the aligned spin component of the primary (secondary).

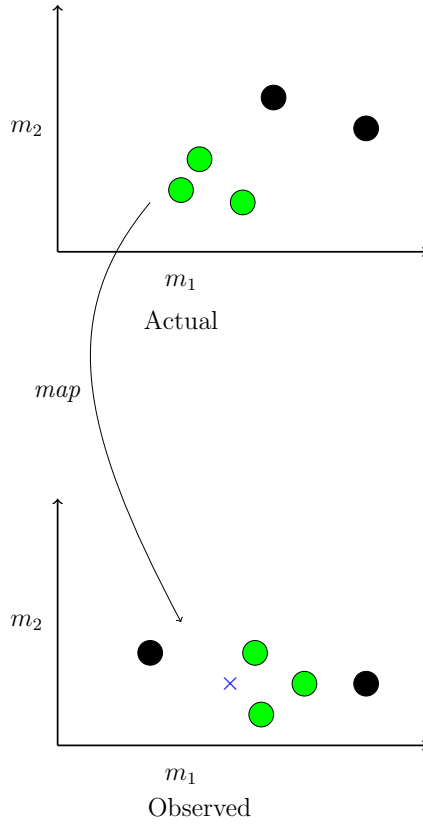


Figure 3.2 This figure is an qualitative illustration of the binary classification treatment of the problem. The top panel represent the true parameter space of binaries i.e, the injected parameters in this case, where the two colors represents satisfying either of the conditions in Eq. (3.3, 3.4). The lower panel is the parameter space of the recovery i.e., what the search reports. For the training process, the parameters in the recovered space are the features, while the label is inferred from the actual parameters. A fiducial detection during the production running is represented by the \times mark in this plane. The probability of this fiducial detection being either of the two binary classes is determined from the nearest neighbors in the recovered parameter space.

Type	Mass distribution	Spin distribution	Num. Injections
BBH	$U[\log m_1, \log m_2]$	$ \chi^{\max} = 0.99$ (Isotropic)	4.0×10^4
BBH	$U[\log m_1, \log m_2]$	$ \chi^{\max} = 0.99$ (Aligned)	1.9×10^4
BNS	$\mathcal{N}[1.33M_\odot, 0.09M_\odot]$	$ \chi^{\max} = 0.05$ (Isotropic)	1.6×10^4
BNS	$U[m_1, m_2]$	$ \chi^{\max} = 0.40$ (Isotropic)	1.6×10^4
NSBH	$U[\log m_1, \log m_2]$	$ \chi_{\text{NS}}^{\max} = 0.40; \chi_{\text{BH}}^{\max} = 0.99$ (Aligned)	1.9×10^4
NSBH	$\delta(m_1 - 5M_\odot, m_2 - 1.4M_\odot)$	$ \chi_{\text{NS}}^{\max} = 0.05; \chi_{\text{BH}}^{\max} = 0.99$ (Aligned/Isotropic)	$1.6 \times 10^4 / 1.5 \times 10^4$
NSBH	$\delta(m_1 - 10M_\odot, m_2 - 1.4M_\odot)$	$ \chi_{\text{NS}}^{\max} = 0.05; \chi_{\text{BH}}^{\max} = 0.99$ (Aligned/Isotropic)	$1.7 \times 10^4 / 1.3 \times 10^4$
NSBH	$\delta(m_1 - 30M_\odot, m_2 - 1.4M_\odot)$	$ \chi_{\text{NS}}^{\max} = 0.05; \chi_{\text{BH}}^{\max} = 0.99$ (Aligned/Isotropic)	$1.8 \times 10^4 / 1.3 \times 10^4$

Table 3.1 The table lists the different population features used in the injection campaign. This includes signals in the three categories of CBC signals - binary black hole (BBH), neutron star black hole (NSBH) and binary neutron star (BNS) categories. The BBH category has both aligned and isotropic spin distributions. The BNS category has high spinning and low spinning systems to account for isolated high spinning neutron stars and galactic binaries. The NSBH category, includes δ function distributions along with uniform in log mass distribution. The U, \mathcal{N}, δ imply uniform, normal and delta function distributions respectively. These injections densely sample possible populations of binaries. The number of found injections that passed the FAR threshold in Eq. (3.2) used in training are listed in the right-most column. The campaign uses the SpinTaylorT4 approximant for BNS injections, and effective one body calibrated to numerical relativity SEOBNR approximant for NSBH and BBH injections.

Such uncertainties are more often the dominant source of error in this inference. While they decrease as the significance increases, they may be pronounced otherwise. Capturing and correcting such selection effects can be done by supervised machine learning algorithms. By injecting fake signals into real noise, performing the search, and comparing the recovered parameters with the original parameters of injections, one gets the *map* between the injected and recovered parameters. This is qualitatively illustrated in Fig. 3.2. Given a broad training set, the supervised algorithm learns this map. The training features are recovered parameters obtained after running the search, however, the labels of having a NS or remnant are determined from the injected values. It should be highlighted that we are not using machine learning to predict the recovered parameters from the injected values, or vice versa. Rather we use it for binary classification, correcting for selection biases that could have, otherwise, given an erroneous answer from the point estimate. We return the probability that the binary had a component less than $3M_{\odot}$, which we assume to be a conservative upper limit of the NS mass, and the probability that it had remnant matter based on the Foucart et al. (2018) (hereafter F18) expression.

3.3.1 Injection Campaign

In this study, we use a broad injection set that well samples the space of compact binaries. The distribution of the masses and spins is tabulated in Table 3.1. The injections are simulated waveforms placed in real detector noise at specific times. The BNS injections use the SpinTaylorT4 approximant (Buonanno et al., 2009), while NSBH and BBH injections use the SEOBNR approximant (Bohé et al., 2017). We consider the injections made in two detector operations from O2 (see Table A.1 for times). The population contains uniform/log-uniform distribution of the masses, and both aligned and isotropic distributions of spins. It was used for the spacetime volume sensitivity analysis for the GstLAL search in Abbott et al. (2019). In particular, injection campaigns were conducted for all astrophysical categories (BNS, NSBH, BBH) to analyze search sensitivity. We use the

results, as a by product, to train our algorithm.⁵

For an injection campaign, as this one, fake GW signals are put in real detector noise, followed by which the search is run, just as in the case of analyzing the production data. The injections maybe recovered based on the noise properties, and the GW intrinsic (masses and spins) and extrinsic (distance, sky location etc.) parameters. Since we are using real data, the dynamic variation of the power spectral density is taken into account (see Table A.1 for the stretch of data used, and the splitting of the data into chunks). Not all injections are found by the searches, partly because of the signal strength, or from having them at a sky location where the detectors are not sensitive. The search reports triggers coincident signal across multiple detectors, simultaneously getting a high detection statistic. The triggers are assigned a false alarm rate (FAR) based on the frequency of background triggers that are assigned an equal or more significant value of the detection statistic. If the time of an injection coincides with the time of recovery of a trigger, the injection is considered found. For this study, we further subsample to the set where the FAR of the recovered triggers corresponding to found injections is less than one per month,

$$\begin{aligned}\text{FAR} &\leq 1/1 \text{ month} \\ &= 3.85 \times 10^{-7} \text{Hz.}\end{aligned}\tag{3.2}$$

This leaves us with $\sim 2.0 \times 10^5$ injections to train our supervised algorithm. The breakdown into different populations is shown in Table 3.1. This FAR threshold is reasonable since the LIGO/Virgo public alerts in the third observing run consider a false alarm rate threshold of one per two months further modified by a trials factor which consider the number of independent searches (see <https://emfollow.docs.ligo.org/userguide/>).

⁵The other search in Abbott et al. (2019)(see Sec. VII therein), PyCBC, conducted broad campaigns for BBH population only. The method presented here, however, can be extended to any general CBC search given suitable training data.

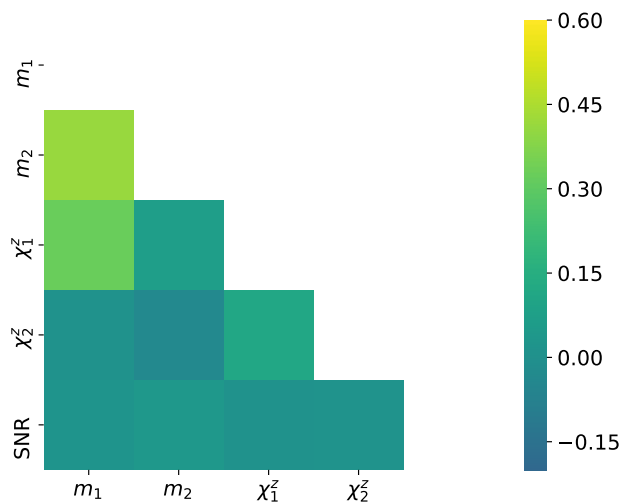


Figure 3.3 This is the correlation matrix of the recovered parameters that form our training set. The masses are expected to be correlated since there is a preference towards detecting heavier masses. The primary spin shows a strong correlation with the primary mass, however, the secondary spin recovery is not as correlated with the secondary mass. The signal-to-noise is mildly correlated with the remaining parameters. as expected since it is a detector frame parameter independent of the source properties.

3.3.2 Training Features and Performance

For the HasNS quantity, to label an injection as having a NS, we use,

$$m_2^{\text{inj}} \leq 3M_{\odot}. \quad (3.3)$$

The value $\approx 3M_{\odot}$ has been regarded as a traditional and conservative upper limit for the NS maximum mass. The limit comes from the causality condition of the sound speed being less than the speed of light. The exact numbers, however, differ based on how the high core density is matched to the low crustal density, which is of the order of the nuclear density. If the low density is known to about twice the nuclear density, one obtains the $\approx 3M_{\odot}$ upper limit (see, for example, [Rhoades & Ruffini, 1974](#); [Kalogera & Baym, 1996](#); [Lattimer, 2012](#)). Observational evidences of pulsars obey this limit (see Table 1 of

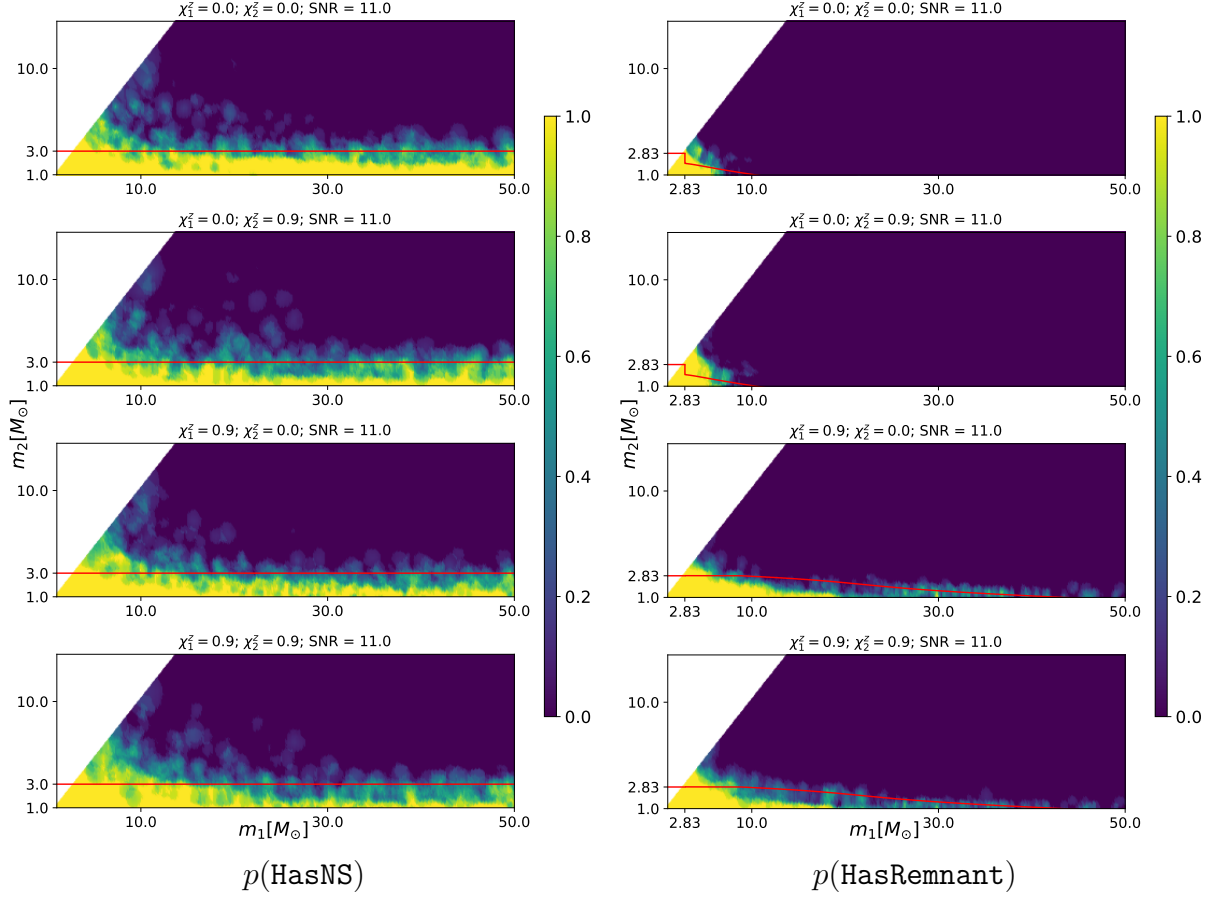


Figure 3.4 This figure shows the predictions of the *trained* binary classifier upon performing a parameter sweep on the (m_1, m_2) values. Note that each point on the plots is analogous to a *point-estimate*. We feed the trained classifier with arbitrary recovered parameter values and evaluate the predictions. **Left panel:** $p(\text{HasNS})$ predictions on the parameter space. We sweep over the masses, keeping the spin and SNR values fixed in each individual plot, incrementing the former as we move down. The horizontal line corresponds to $m_2 = 3M_\odot$ around which we expect a *fuzzy* region due to the detection uncertainties. Also, it is to be noted that the performance does not get affected by much upon increasing spin values since our original classification did not depend on it. Small changes are, however, expected due to correlation between the parameters during recovery (see Fig. 3.3). **Right panel:** $p(\text{HasRemnant})$ predictions on the parameter space. The region denoting non-zero remnant matter shows a more constrained classification about presence of matter compared to just having a NS in the binary. Also, note that unlike $p(\text{HasNS})$, $p(\text{HasRemnant})$ is strongly affected by the primary spin, as expected. The red curve in this panel represents the contour $M_{\text{rem}}(m_1^{\text{rec}}, m_2^{\text{rec}}, \chi_1^{\text{z rec}}) = 0M_\odot$, calculated from recovered parameters using Eq.(4) of Foucart et al. (2018). Note that the M_{rem} expression applies to NSBH systems and require a NS EoS which sets a maximum mass for the NS. In this study, we use the 2H EoS (Kyutoku et al., 2010) which has a maximum mass of $2.83M_\odot$. Mass components above this maximum mass are considered BHs which do not leave remnant matter upon coalescence. This explains the kink in the red curve in the top two panels.

Lattimer, 2012). The total mass of the GW170817 system, $\approx 2.74M_{\odot}$, also provides an observational upper limit. Although the system could have undergone prompt collapse to form a BH, ejecting some mass prior to it (see Sec. 2.2 of Friedman (2018), and references therein for a discussion). Some GW template based searches, also, regard the $3M_{\odot}$ to be the upper boundary for placing BNS templates (Nitz et al., 2018). Thus, Eq. (3.3) is conservative and fundamental inference about the presence of a NS. However, we should mention that the presence of compact objects apart from BNS, NSBH, and BBH which satisfy Eq. (3.3) would be included in this inference. Our inference is only based on the secondary mass, and we do not prejudge the nature of the object.

For the `HasRemnant` quantity, to label an injection as having remnant matter, we use the F18 empirical fit to check for non-vanishing remnant matter (see Eq. (4) therein for expression),

$$M_{\text{rem}}(m_1^{\text{inj}}, m_2^{\text{inj}}, \chi_1^z \text{inj}) > 0. \quad (3.4)$$

The F18 fit requires the compactness of the NS, and hence an EoS model. For this work, we use the 2H EoS (Kyutoku et al., 2010), which has a maximum NS mass of $2.83M_{\odot}$. Note that this value is not to be confused with the value mentioned in Eq.(3.3), which is the value considered for the `HasNS` categorization. The value $2.83M_{\odot}$ for `HasRemnant` comes from the usage of a particular model EoS. We use the condition in Eq. (3.4) only for the injections which have primary mass above the $2.83M_{\odot}$ and secondary mass below this value i.e., NSBH systems based on this EoS. The injections having both masses less than $2.83M_{\odot}$ are labeled as having remnant, while those with both masses above this value are labeled as not having remnant, based on the assumption that BNS mergers will always produce some remnant matter, while BBH mergers will never do so. The 2H is an unusually stiff EoS resulting in NS radii $\sim 15 - 16$ km, but it errs towards larger values of the remnant matter, and therefore is a conservative choice in the sense of not misclassifying a CBC having remnant matter as otherwise, due to uncertainty in the EoS.

Fraction	Misclassification % $p(\text{HasNS})$			Misclassification % $p(\text{HasRemnant})$		
	Uniform	Inverse distance	Mahalanobis metric	Uniform	Inverse distance	Mahalanobis metric
0.1	3.21	3.38	4.24	4.04	4.34	3.77
0.2	3.03	2.98	3.80	3.65	3.62	3.28
0.5	2.91	2.96	—	3.00	2.92	—
0.9	2.83	2.80	—	2.65	2.64	—
1.0	2.83	2.82	—	2.59	2.59	—

Table 3.2 The table lists the percentage misclassification when using a threshold of $p(\text{HasNS}/\text{HasRemnant}) = 0.5$ to classify a binary as EM bright as a function of the fraction of the dataset used for training and testing purposes. Out of the fraction of the total dataset used (left most column), we train using 90% and test on the remaining 10%, cycling the training/testing set to have predictions on all points in the set. The *uniform* and *inverse distance* weighting of the nearest neighbors are used in all cases. We see that the answer starts to converge when using $\gtrsim 50\%$ of the total dataset. In light of verifying correlations (shown in Fig. 3.3) between parameters not affecting the prediction and the impurity, we trained using the *Mahalanobis* metric (*Mahalanobis, 1936*) in the parameter space mentioned in Eq.(3.5)^a. The misclassification does not change significantly based on the weighting scheme or the metric used.^b

^a See <https://scikit-learn.org/stable/modules/generated/sklearn.neighbors.DistanceMetric.html> for the implementation in the `scikit-learn` framework.

^b Cross-validation when using the Mahalanobis metric is expensive and was performed for small fractions of the total training data.

We can restrict to the part of the parameter space on which the classification strongly depends on. We choose the following set as training features:

$$\boldsymbol{\beta} = \{m_1, m_2, \chi_1^z, \chi_2^z, \text{SNR}\}. \quad (3.5)$$

The reason for using more parameters than those which are used to label the injections is because the recovered parameters have correlations (see Fig. 3.3). For example, the masses are expected to be positively correlated since the chirp mass is recovered fairly accurately and is an increasing function of the individual masses. There can also exist biases in the recovery due to degeneracies in the space of CBC GW signals. For example, high spin recovery is associated with high mass ratio. Regarding the choice of the feature set to be used, the masses and primary spins are natural since they are the intrinsic properties of the binary on which the source properties depend. As for a detection specific property, we use the signal to noise ratio, SNR, since it captures the general statistical uncertainty in the recovered parameters.

With this set, we use the machinery of supervised learning provided by the `scikit-learn` library (Pedregosa et al., 2011) to train a binary classifier based on the search results. Once trained, the classifier outputs a probability $p(\text{HasNS})$ or $p(\text{HasRemnant})$ given arbitrary but physical values of $\boldsymbol{\beta}$. We tested the performance using two non-parametric algorithms: `KNeighborsClassifier` and `RandomForestClassifier`, both provided in the `scikit-learn` library. We found that the former outperforms the latter in our case and is used for this study.⁶ We train it using 11 neighbors – twice the number of dimensions plus one to break ties. The collection of parameters of a point-estimate is a point in this parameter space. To obtain the probability of this point having a secondary mass $\leq 3M_\odot$ or having some remnant matter based on F18 expression, we use the nearest neighbors

⁶The nearest-neighbor algorithm also fits best with the intuition of a map by which the injected parameters, with the right labels, are *carried* over to the recovered set rather than a decision tree made by relational operations (which look like “linear cuts”) in the parameter space at every *branch* of a decision tree.

from the training set, weighting them by the inverse of their distance from the fiducial point,

$$p(\text{HasNS}/\text{HasRemnant}) = \frac{\sum_{\text{HasNS}/\text{HasRemnant}} w_K}{\sum w_K}, \quad (3.6)$$

where the numerator (denominator) goes over neighbors that satisfy Eq.(3.3, 3.4) (all neighbors) of the fiducial point, and $w_K = 1/d_K$ ($w_K = 1$) for the inverse distance (uniform) weighting. We also used the *Mahalanobis* metric (Mahalanobis, 1936) in the space of β where distance, and therefore, nearest neighbors are determined via,

$$d_K = (\mathbf{x} - \tilde{\mathbf{x}})^T \Sigma^{-1} (\mathbf{x} - \tilde{\mathbf{x}}), \quad (3.7)$$

where $\tilde{\mathbf{x}}$ is the mean and Σ is the covariance matrix of the training set. This is done in the light of handling correlations. We, however, find that the metric or weighting scheme used does not affect the result significantly (see Table 3.3.2).

3.3.3 ROC Curve

Threshold	TP(HasNS)	FP(HasNS)	TP(HasRemnant)	FP(HasRemnant)
0.07	0.999	0.144	0.995	0.106
0.27	0.995	0.096	0.979	0.040
0.51	0.986	0.061	0.949	0.014
0.80	0.959	0.028	0.894	0.003
0.94	0.900	0.010	0.822	0.001

Table 3.3 The table lists some example values of true positive and false positive numbers for changing values of the threshold used in Fig. 3.5. The column containing threshold values correspond to the colorbar in both panels. The true positive and false positive values are to be read off based on HasNS/HasRemnant case.

In the case of perfect performance, one expects the trained algorithm to predict $p(\text{HasNS}) = 1$ ($p(\text{HasRemnant}) = 1$) from the recovered parameters of the fake injections which originally had a NS (had remnant matter). On the other hand, in absence a NS component

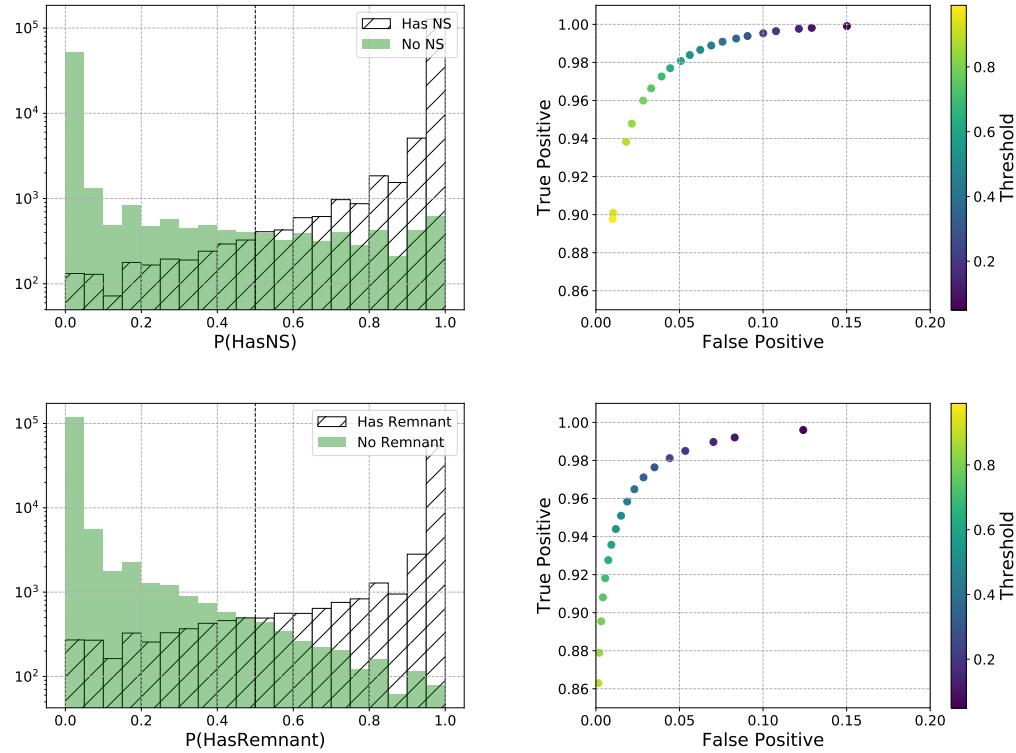


Figure 3.5 This figure shows the receiver operating characteristic curve for the classifier. It shows the true-positive against the false positive as a function of the threshold to classify binaries as having an NS or having remnant matter. **Top panel:** The left figure is a histogram of the $p(\text{HasNS})$ values for the injections which represented a binary that had an NS and for those that did not. In the limit of perfect performance, the values for the former (latter) should be at $p(\text{HasNS}) = 1$ ($p(\text{HasNS}) = 0$). The true positive and false negative performance is decided based on the threshold that is applied to make the decision. For example, using the value of $p(\text{HasNS}) = 0.5$ (dot-dashed vertical line) would imply that all the values to the right of the line are decided as having a NS. While such a decision captures most of the true NS bearing binaries, one can notice a small misclassification fraction. The right figure shows the fractions as a function of this threshold. **Bottom panel:** Similar plots as the top panel except that the values correspond to the binary having remnant matter after merger.

we also do not expect any remnant matter and hence expect $p(\text{HasNS}/\text{HasRemnant}) = 0$. In order to test the accuracy of the classifier we trained the algorithm on 90% of the dataset and tested it on the remaining 10%, cycling the training/testing combination on the full dataset. The results are shown in Fig. 3.5. While most of the binaries are correctly classified as shown in the histogram plot (left panel) for the two quantities, there is a small fraction which does not end up getting perfect score ($p(\text{HasNS}) = 1$). The choice of threshold value to consider a binary suitable for follow-up operations would result in an impurity fraction. For example, if we use $p(\text{HasNS}) \geq 0.5$, shown as a dashed vertical line in the upper left panel of Fig. 3.5, the contribution of the “No NS” histogram to the right of that line constitutes the false-positive. The variation of the efficiency with the false-positive as a function of the threshold applied is shown in right panels of Fig. 3.5. Some example values are listed in Table 3.3. The threshold could be set depending on the desired efficiency or, alternatively, the false positive to tolerate. We would like to highlight that the ROC curve depends on the relative rates of the different astrophysical sources. In this injection campaign each population has been densely sampled, without considering the relative rates. However, the current methodology works given an injection campaign curated based on astrophysical rate estimates of mergers as more observations are made.

The predictions of a parameter sweep on the (m_1, m_2) values is shown in Fig. 3.5. Considering, the $p(\text{HasNS})$ plot, a perfect performance of the search would have rendered the region under the vertical line of $m_2 = 3M_\odot$ as $p(\text{HasNS}) = 1$. In reality, we expect a fuzz around the $m_2 = 3M_\odot$ line, as shown in the figure. The $p(\text{HasRemnant})$ is behaving as expected with respect to the increasing spin values, increasing the region having non-vanishing remnant mass boundary.

Chapter 4

Sky Tiling For The Zwicky Transient Facility

This chapter is reproduced in part from [Ghosh et al. \(2017\)](#), published under the title *Hunting Electromagnetic Counterparts of Gravitational-wave Events Using the Zwicky Transient Facility* in Publications of the Astronomical Society of the Pacific © 2017 The Astronomical Society of the Pacific. This is an author-created, un-copied version of an article accepted for publication in Publications of the Astronomical Society of the Pacific. The publisher is not responsible for any errors or omissions in this version of the manuscript or any version derived from it. The Version of Record is available online at <https://doi.org/10.1088%2F1538-3873%2Faa884f>.

Sky-localization of gravitational wave (GW) events detected by LIGO-Virgo interferometers often cover hundreds of square degrees. The first direct detection of GW from a coalescing binary black hole (BBH), GW150914, was localized in the sky (90% confidence

interval) over an area of 630 square degrees at the time of the alert (Abbott et al., 2016b). Events with a lower signal to noise such as GW151226, have larger sky-localization area, in excess of 800 square degrees (Abbott et al., 2016a). The sky-localization for triggers with lower significance (which could be the case for non-BBH triggers) could potentially be larger, often spanning over a thousand square degrees. The Zwicky Transient Facility (ZTF) (Bellm, 2014) with its ~ 50 square degrees field-of-view (FOV) would need tens of pointings to get a single observation over the 90% credible region. We expect ZTF to reach a limiting magnitude of $r = 20.5$ in 30 seconds. Kilonovae, which are EM emissions from r -process nucleosynthesis triggered by coalescing binaries of neutron star(s) (Li & Paczyński, 1998), continue to have light-curve models with a lot of uncertainties. Estimates of the absolute magnitudes of kilonovae range from -12 to -15 (Roberts et al., 2011; Tanaka & Hotokezaka, 2013). For sources at 200 Mpc this corresponds to apparent magnitudes of ~ 21.5 to 24.5 in the R-band. Thus if the desired depth is higher than the standard depth of $r = 20.5$ for gravitational-wave events, much larger integration time could be required. Furthermore, a single observation may not be enough to identify transients. Observations at two different epochs, preferably with two different filters will most likely be necessary to get sufficient photometric information necessary to discern the actual electromagnetic (EM) counterpart of the gravitational wave triggers from a myriad of false positive (Cowperthwaite & Berger, 2015). The first step towards such observation is an efficient sky-tiling method that will allow us to set up an observing strategy for any given event. In this paper, we present a sky-tiling method that is applicable for telescopes with wide fields of view and fixed tile coordinates, where, the fields at which the telescopes can point to are predefined. This is helpful for image subtraction required for transient identification. We used specifications of the ZTF telescope obtained from Bellm (2014) for this work. Note that this is a sky-tiling strategy study, and therefore we did not take into account observing conditions such as geographic location of the telescope, the visibility conditions like phases of the moon and weather. Some of these aspects have been studied

in the recent past (Rana et al., 2017; Srivastava et al., 2017). A detailed work related to the intermediate Palomar Transient Factory is presented in chapter 5.

4.1 Tiling Strategies

Sky-localization information of the alerts from LIGO-Virgo comes in the form of HEALPix (Hierarchical Equal Area isoLatitude Pixelisation) sky-map Singer et al. (2016b). Each pixel has the probability of the gravitational-wave source being located at the center of the pixel, computed from the GW strain data of the interferometer. The observation of the sky-localization regions involves strategically tiling the sky, where each tile corresponds to the footprint of the field of view of the telescope. The localization probability contained in a single tile is given by the sum of all the pixels that lie within its boundaries. We describe two strategies for sky-tiling.

4.1.1 The Contour-covering Strategy

This is the most commonly used strategy when it comes to EM follow-up of GW triggers Kasliwal et al. (2016); Soares-Santos et al. (2016); Smartt et al. (2016). It is also a sub-optimal one, especially when the tile coordinates are predefined on a fixed grid in the sky Ghosh et al. (2016). However, given the simplicity of the concept, we discuss this first. From the sky-maps one can construct the smallest 90% confidence interval for the source localization. If we enclose this region(s)¹ by contour(s), we can define a 90% credible region resembling patch(es) in the sky. Contour-covering tiles (CC-tiles), as the name suggests, are the smallest number of tiles that are required to enclose this 90% credible region. For ZTF, the tile coordinates are predefined in the sky, thus, the set of tiles that cover a given 90% confidence interval is unique. Note that the CC-tiles will always cover more than 90% localization probability due to finite size of the telescope’s FOV. However,

¹Note that the smallest 90% confidence region might be multi-modal over the sky.

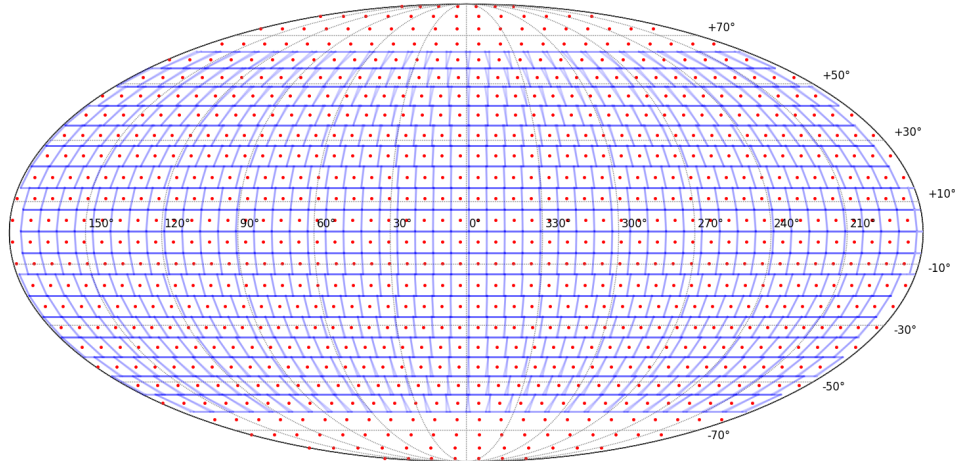


Figure 4.1 Planned tile locations for ZTF: The red points are the tile centers and the blue squares are the tile boundaries. We do not show the tile boundaries for the tiles at large declination values (near the poles) as the boundaries (approximated as sides of trapezoids) get severely distorted near the poles.

any additional localization that the CC-tiles cover is incidental and is most often not the best use of additional observation time or the ideal way to cover an additional area.

4.1.2 The Ranked Tiling Strategy

There exists a more natural way of tiling the sky that suits any particular telescope whose observing fields are predetermined. Instead of covering the contour, we can compute the sky-localization probability enclosed by all the tiles in the sky shown in Fig. 4.1. We then rank the tiles based on their localization probabilities and then choose from the top of these ranked tiles the set of tiles whose cumulative probability sum is $\geq 90\%$. We implemented two distinct algorithms to do this:

Tagging pixels to tiles

Two observed facts about the ZTF tiles motivated this method. First, the ZTF tiles are placed in such a way (Fig. 4.1) that there are no gaps in the sky. This means that there are no orphan pixels, i.e., every HEALPix pixel will be within a tile. Second, ZTF’s rectangular

FOV on a spherical sky-surface means that each tile will always have some overlap with neighboring tiles, with the overlap getting larger near the celestial poles. Both of these features of the ZTF tiles help us to adopt an algorithm, where we loop through the pixels, and for each of them we search for the nearest tile center. We assign each pixel to its nearest tile center and then compute the accumulated probability for each tile. This leads to the required ranked tiles, which are the list of tiles in descending order of probability values contained within the tiles. Looping over the pixels ensures that we are not double counting pixels in the overlap regions.

Greedy algorithm

This is a modification of the algorithm above:

1. For each tile, integrate the probability over the tile and sort the tiles based on these values.
2. Beginning with the highest value, include that tile in the list of those to cover and increment the summed probability.
3. Zero out the probability for that whole tile so that the sky area is not repeated
4. Recompute the integrated probabilities with the updated sky map, resort and repeat step 2 until the required probability is reached.

Ranked tiling is however computationally slower than the contour-covering method in selecting the tiles required to cover 90% localization. This is because in the contour covering method we know the location of the pixels of interest as shown in Sec. 4.1 based on the contour of the confidence interval. If we can label these pixels (using a pixel ID for example), then all that is required beyond that is to find the tiles that have these labeled pixels. However, speed of the ranked tiling can be vastly improved by pre-computing which pixels belong to each tile. This mapping of the pixels to tiles on the predefined grid needs to be

done once for a given telescope. For example, the densest (hence most computationally expensive) sky-maps require close to an hour for the computation of the ranked tiles. However, we achieve a speed up in the computation by 100 times upon pre-computation, making the computation time requirement comparable to the contour-covering method. Thus, the present analysis uses the pre-computation mentioned above. We show in Fig. 4.2 the performance of the CC-tiling and ranked-tiling strategies in generating the ZTF pointings for a simulated event.

4.2 Contour Covering vs. Ranked Tiling

Having described the two methods of tiling (ranked and contour covering), we present the result of a study that was conducted over 475 simulated GW events. These events were obtained from the sky-localization study of binary neutron star coalescences from the simulation of 2016 LIGO-Virgo noise data [Singer et al. \(2014\)](#), which is a mix of two- and three-detector networks appropriate for early ZTF operations. In Fig. 4.3, we compare the area of the 90% credible region covered by the ranked-tiling strategy with that needed to actually cover the simulated GW event location. If the sky-localizations are consistent, then $\sim 90\%$ of the events, depicted by red stars, should be below the black line. For comparison we also include the sky-localization searched area vs 90% coverage in blue dots. This reflects the consistency of the sky-maps themselves. We find that 89.6% of the black crosses, and 88.9% of the red circles fall below the dashed black line. Thus, the localization probability enclosed in the GW sky-maps is consistent with the actual location of the source, and the ZTF tiles gives reasonably similar results (slightly worse due to discrete size FOV of the telescope which is significantly larger than the unit HEALPix pixel size).

We then compared the ranked-tiling and contour-covering algorithms for all the 475 events using expected ZTF tiles. To quantify the comparison, we compute the number of tiles required by the two methods to cover the 90% localization confidence interval for the

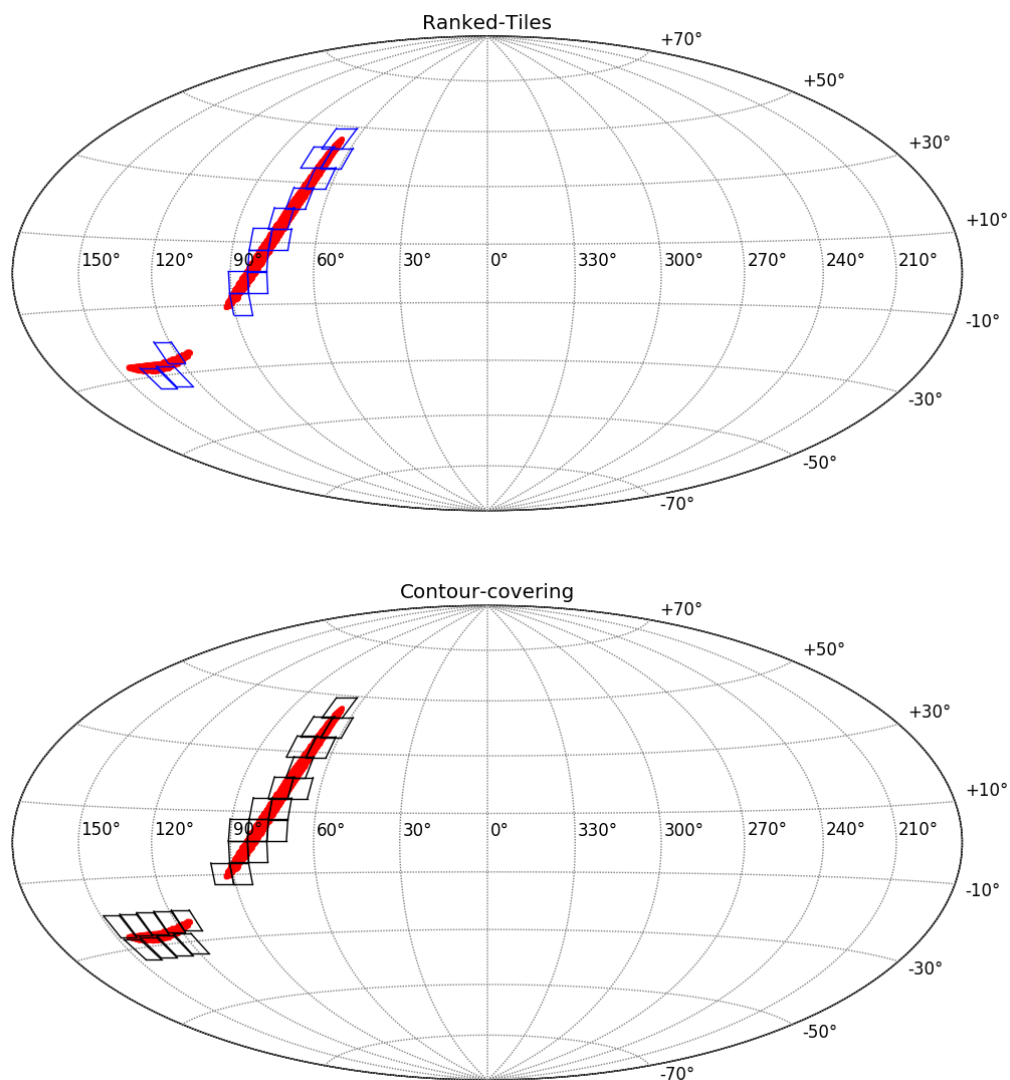


Figure 4.2 Comparison between ranked tiles (top) and contour-covering tiles (bottom) for a simulated gravitational-wave sky-localization (event number 632720 from [Singer et al. \(2014\)](#)). In this case we note that the 15 ranked tiles (blue) required to cover the 90% confidence interval in sky-localization are a subset of the 26 contour-covering tiles (black).

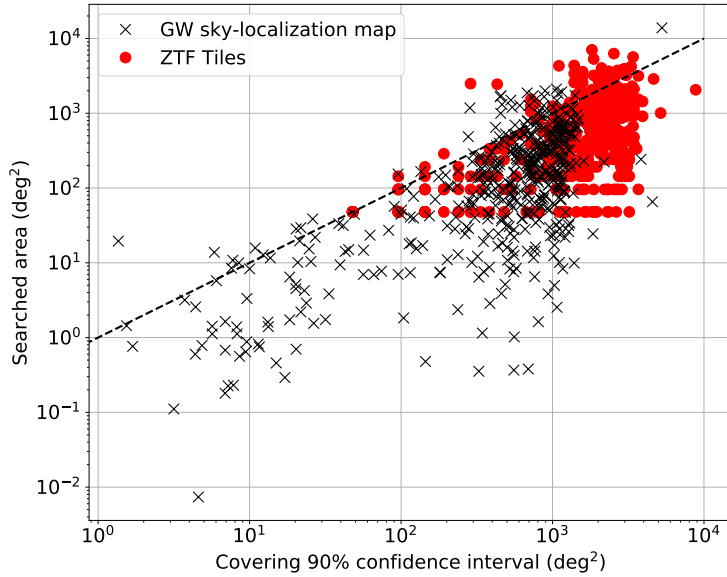


Figure 4.3 Comparison of sky area searched to cover 90% of the probability using a ranked-tiling strategy (horizontal axis) with the area searched to actually cover the simulated gravitational wave event (vertical axis). This is shown for both the original location. The blue dots correspond to the original sky-localizations data obtained from the HEALPix sky-maps (blue dots) and the ZTF tiles (red stars).

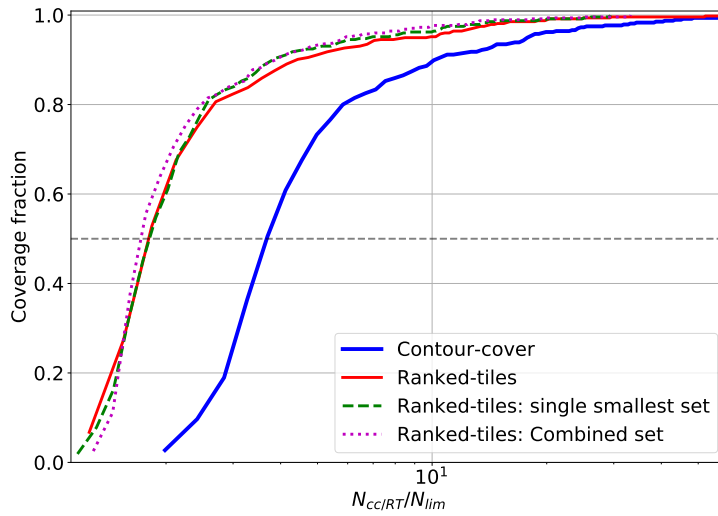


Figure 4.4 Cumulative histogram of the ratio of N_X to N_{lim} for different strategies and tile sets: contour-covering (solid blue), ranked tiling with one tile set (solid red), ranked tiling with the smallest of two sets (red dashed) and ranked tiling with a combined set (red dot-dashed). Ranked tiles with single smallest set shows the case where ranked-tiling algorithm was implemented for two sets of tiles and the smallest was chosen. Ranked tiles combined set is the case where we implemented the greedy ranked-tiling algorithm to obtain the ranked-tile set from the two sets of tiles.

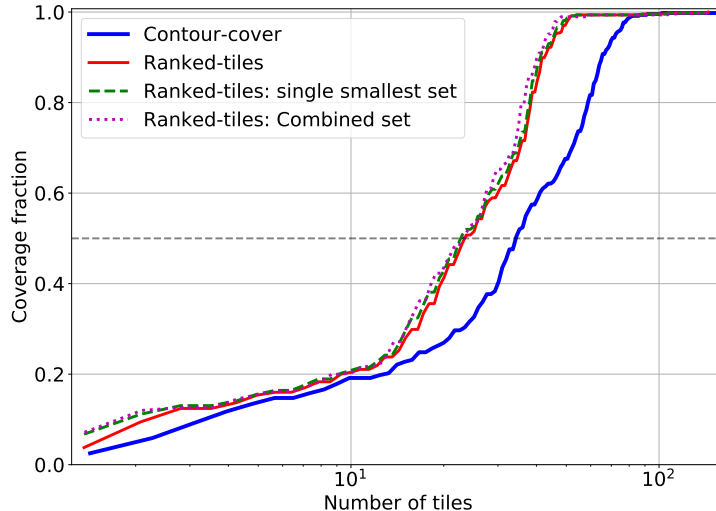


Figure 4.5 Cumulative histogram of coverage fraction as a function of number of tiles covered according to various tiling methods. We note that all the ranked-tiling strategies give consistently better result than the contour-covering technique.

ranked tiles (N_{RT}) and the 90% credible region for the contour-covering tiles (N_{CC}). For each event we also define a packing-fraction, which is the limiting number of tiles required to cover the 90% confidence interval N_{lim} ,

$$N_{\text{lim}} = \frac{N_{\text{pix}} \times A_{\text{pix}}}{A_{\text{fov}}}, \quad (4.1)$$

where N_{pix} is the number of HEALPix pixels in the 90% localization region, A_{pix} is area of each pixel, together giving the area of the 90% localization region, and A_{fov} is the area of the field-of-view of the telescope. Dividing N_{CC} and N_{RT} by N_{lim} provide a metric for comparison of the tiling methods with the minimal limiting case. This quantity is plotted on the horizontal axis of Fig. 4.4 where we histogram the result of the tiling by the two methods. Larger values of N_X/N_{lim} , where $X = CC$ or RT , indicate greater deviation from the limiting value and hence poorer coverage by the tiles. The median value of N_X/N_{lim} for the ranked tiles is 1.91, compared to 3.89 for contour-covering tiles. This indicates that for the binary neutron star sky-localizations obtained from Singer et al. (2014) the ranked-tiling strategy’s performance is ~ 2 times better than the CC-tiling. Note that in Kasliwal

Tiling strategy	Median N_X/N_{lim}
Contour cover	3.89
Contour cover (optimized)	2.60
Ranked-tiling	1.91
Ranked-tiling (smallest)	1.86
Ranked-tiling (combined)	1.79

Table 4.1 The table shows the performance of the different tiling strategies to cover the gravitational wave localizations.

& Nissanke (2014) the factor N_{CC}/N_{lim} was computed to be around 2.6, although those authors used a different set of simulations and optimized set of CC-tiles. The CC-tiles in our study does not allow for any optimization and are closer to the strategy that will be adopted by ZTF.

ZTF is expected to include two sets of tiles, with the second set offset from the first by half a tile in Right Ascension. We conducted the same analysis as above for the two tile-sets. For each event we conducted the study using the two sets independently and chose the one that gives the smaller number of tiles, with a median N_{RT}/N_{lim} of 1.86: just a 2.6% improvement over the basic ranked-tiles case. If we apply the greedy algorithm to select tiles from both the sets simultaneously, the value of N_{RT}/N_{lim} becomes 1.79: a 6.7% improvement over the basic ranked-tiles case. It is clear that there is limited room for further improvement, as the ratio is already getting close to 1. We also show the cumulative histogram of the number of tiles required to reach a given coverage fraction for all the method in Fig. 4.5. We note that the simple ranked-tiling method gives reasonably similar results using a single set to those incorporating the two tile sets to create the ranked tiles. In Table 4.1 we summarize the result of this study. The first column shows the tiling strategy, where ranked-tiling (smallest) is the strategy where we use two sets of tiles and find the ranked tiles for both the sets independently, then we choose for each event the set with the minimum number of tiles. Ranked-tiling (combined) is the strategy where the two sets of tiles were used together to find a single set of non-overlapping ranked tiles for each

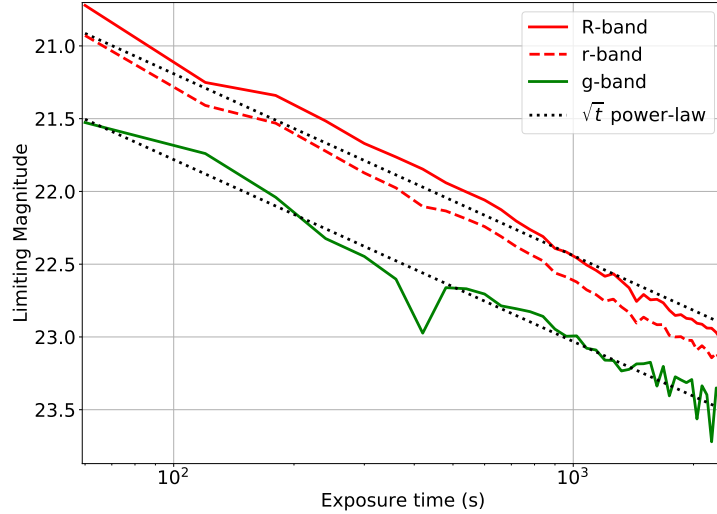


Figure 4.6 Assumed integration time vs. limiting magnitude for ZTF, based on the g- and R-band PTF data. PTF g-band and R-band are shown by the green and red solid lines respectively. We converted the R-band limiting magnitude to r-band limiting magnitude using Lupton (2005). We also show the expected $S/N \sim \sqrt{t}$ behavior for comparison.

event. Contour covering (optimized) is the number obtained from Kasliwal & Nissanke (2014). The second column shows the median of N_X/N_{lim} for each method. Note that this is a separate simulation of binary neutron star coalescence, conducted with LIGO-Virgo design sensitivity noise curve. Thus, this number is purely for reference of previous studies and should not be compared quantitatively with the other numbers in this study.

4.3 Depth vs. Coverage

We have restricted our analysis until now to coverage of sky-localization regions. Given the large size of the GW sky-localizations, covering the 90% confidence interval in general could be a challenging task on its own. However, any statement on detectability of EM-counterpart also needs to incorporate discussion of depth of the observation. For the present analysis we use the PTF integration time-limiting magnitude data as a proxy for the ZTF analysis; while ZTF may go somewhat deeper in the same observing time due to an improved detector, assuming the PTF characteristics will be a conservative assumption.

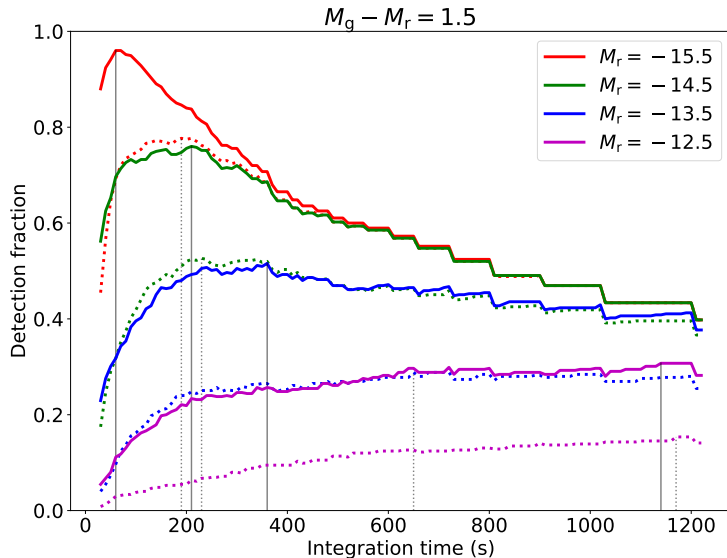


Figure 4.7 The detection fraction as a function of the integration time per pointing. The total observation time is two hours. Based on results obtained from [Rosswog et al. \(2017\)](#) we chose $M_g - M_r = 1.5$. We present the results for four model lightcurves, $M_r = -12.5$ (in magenta), -13.5 (in blue), -14.5 (in green) and -15.5 (in red). The dotted lines are for corresponding $M_g = M_r + 1.5$. The vertical black lines denotes the integration time required to reach maximum detectability. If the maximum is not reached during the observation then we set the integration time maxima at 20 minutes. If kilonovae are intrinsically dim, observing deeper improves detection efficiency, while for models that allows for brighter light-curves, we observe that a detectability-maxima is reached in 100-300 seconds of observation.

We show in [Fig. 4.6](#) the relationship between these two quantities. Note that PTF uses g-band and R-band magnitudes. We converted the R-band magnitude to r-band magnitude by using conversion relation provided by [Lupton \(2005\)](#)². If we know the distance of the injected BNS sources and their (intrinsic) absolute magnitudes, we can compute their expected apparent magnitude. Sources whose apparent magnitudes are lower than the limiting magnitude are detectable if the source location is covered by the tiles. In this work, we used a set of absolute magnitude models for kilonovae from [Rosswog et al. \(2017\)](#). Specifically, we noted that an absolute magnitude difference of $\sim 1 - 2$ between M_g and M_r is predicted theoretically for early-time kilonovae light-curves. Thus, in our analysis, we did the following:

²<https://www.sdss3.org/dr10/algorithms/sdssUBVRITransform.php>

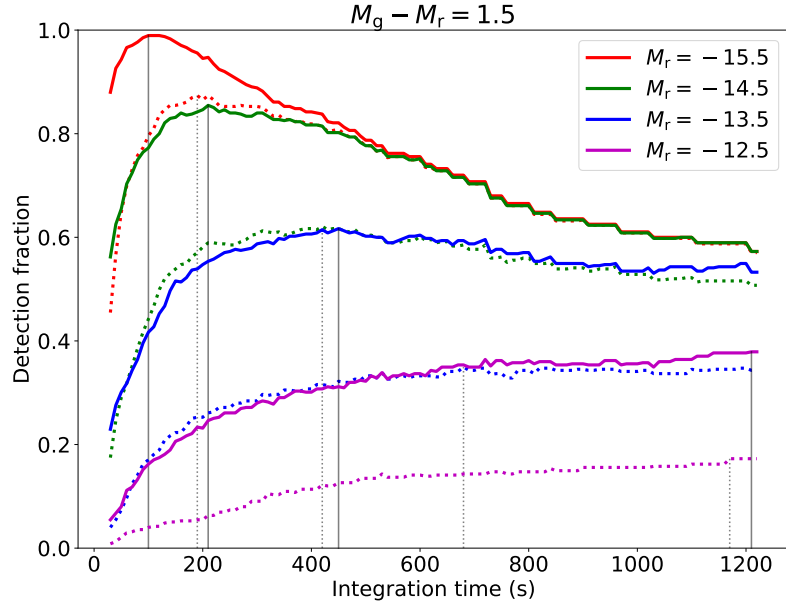


Figure 4.8 The detection fraction as a function of the integration time per pointing. The total observation time is four hours. The color and the style of the lines follows the convention set in Fig. 4.7.

- We considered $M_g - M_r = 1.5$ and chose four values of M_r : $(-15.5, -14.5, -13.5, -12.5)$
- Assumed three total observation times of two hours, four hours, and six hours, motivated by typical observation duration that may be available to observers in a given night of observation. These correspond to Fig. 4.7, Fig. 4.8 and Fig. 4.9 respectively.
- Scheduled the observation based on the rank, starting with the highest ranked tile until total observing time is exhausted or the location of the event is found (i.e., the event location is within the ranked tiles that have been covered).
- The time spent per tile was progressively increased from 30 seconds (the shortest expected ZTF exposure) to 20 minutes.

The source is considered detected when the source location is covered by and observed at a depth greater than what is required to reach the source at the injected distance (for the given model of absolute magnitude). Since, too large of an integration time would not allow us to cover the localization area efficiently, and too wide an attempted coverage

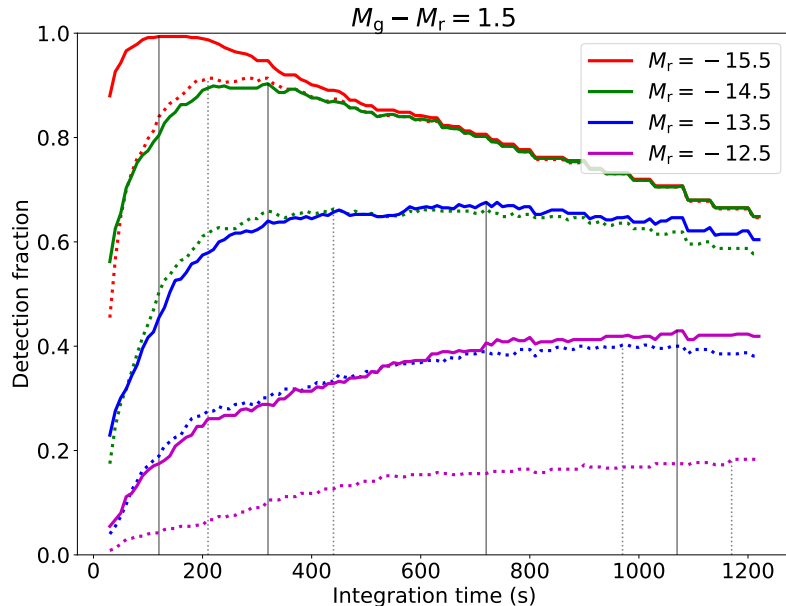


Figure 4.9 The detection fraction as a function of the integration time per pointing. The total observation time is six hours. The color and the style of the lines follows the convention set in Fig. 4.7.

would prevent us from reaching the required observation depth, there may exist an optimal integration time for such observation. The goal of this study is to search for this optimal integration time for observation of GW triggered kilonovae with expected brightness. In Figs. 4.7, 4.8, and 4.9 we show the results for all the cases

We observe that if kilonovae are intrinsically brighter, we will be able to observe the sky-localizations with lower integration time ($\sim 100 - 300$ seconds) to achieve maximum detection efficiency. With increasing total observation time, we can afford to increase the integration time to get to higher detection efficiencies that were inaccessible for observation scheduled for shorter total times. This can be seen in the right-ward progression of the peak of each curve from Fig 4.7 to Fig. 4.9. If kilonovae are intrinsically weaker, then we need to invest longer time per pointing, for any given total observation time, to reach a detectability-maxima. For the dimmest models in our experiment, we did not find a maxima within 20 minutes of per-pointing integration time. For such cases, we constrained the maxima to the detection efficiency value corresponding to integration time of 20 min-

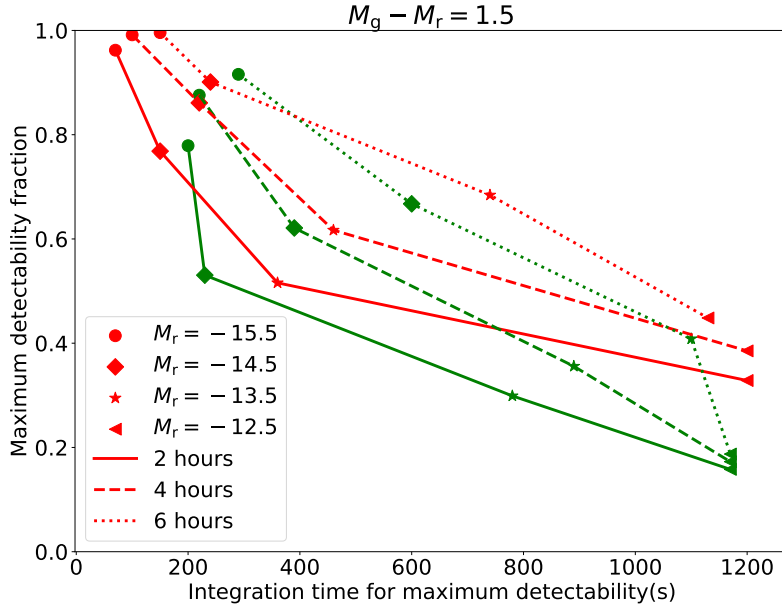


Figure 4.10 The maximum detectability fraction as a function of the integration time required to reach this detectability fraction. The red and green lines are for r -band filters and g -band filters respectively. The solid, dashed and dotted lines show the variation of the maximum detectability as a function of integration time for two, four and six hours of observations respectively. The circle marker shows the maximum detectability for $M_r = -15.5$, diamond marker shows the same for $M_r = -14.5$ and the star and triangle markers shows the maximum detectability for $M_r = -13.5$ and -12.5 respectively, with the corresponding values for M_g obtained by setting $M_g = M_r + 1.5$.

utes. In Fig. 4.10 we summarize the results of this analysis, where we plot the maximum detectability fraction as a function of the integration time required to reach maximum detectability for all the cases discussed above. Thus, we note that a minimum of ~ 100 seconds of integration time is essential for ZTF to achieve maximum detectability of the counterparts of GW if kilonovae are intrinsically bright. Greater integration times are required to achieve the detection efficiency maxima if kilonova brightness is more modest.

In this study we have made two very simplifying assumptions (other than the assumptions on the absolute brightness of the sources). Firstly, we did not include any light-curve evolution. This can be easily incorporated. However, given the time-scales (≤ 6 hours) we are considering in your analysis, including more information about the light-curves which varies in many hours to days time-scale does not seem very essential. Secondly, once again

we assumed no constraints based on day-night or part of the sky visible from a given location. We also did not consider that the sky-localization itself will be moving across the sky over the course of the observation. These will be addressed in our future studies.

Chapter 5

Toward Rate Estimation For Transient Surveys

This chapter is reproduced in part from [Chatterjee et al. \(2019b\)](#), which was published under the title *Toward Rate Estimation for Transient Surveys. I. Assessing Transient Detectability and Volume Sensitivity for iPTF* in The Astrophysical Journal © 2019 The American Astronomical Society.

5.1 Motivation & Challenges

The last two decades have brought about a revolution in the field of time-domain optical astronomy with experiments like Sloan Digital Sky Survey, ([Sako et al., 2007](#)) the Palomar and intermediate Transient Factory (PTF), ([Law et al., 2009](#)) the Catalina survey, ([Drake et al., 2009](#)) Pan-STARRS, ([Kaiser et al., 2010](#)) the ATLAS survey, ([Shanks et al., 2015](#)) Zwicky Transient Facility (ZTF) ([Kulkarni, 2016](#)) and the All-Sky Automated Survey for Supernovae ([Holoien et al., 2019](#)) performing all sky searches with rolling cadence to locate

transients. The timescale of these transients varies from a few minutes, like M dwarf flares, up to a few weeks or months, like supernovae.

Studying transient rates is essential to understand the progenitor systems and environments they occur in. For example, while core-collapse supernovae are associated with more recent massive stars, type Ia supernovae occur in both younger and older populations (Maoz & Mannucci, 2012). The distribution of transients in space and time helps us understand metal enrichment, galaxy formation and the overall evolution of the universe. The classification and compilation of transients from the surveys provide a rich dataset which can be used to make statements about their rates and population. Next generation surveys like the Large Synoptic Survey Telescope (Ivezić et al., 2008) are expected to make significant additions to already existing catalogs with wide-deep-fast searches.

A quantitative assessment of the transient detectability by the survey is an essential component required to study transient rates. A survey could miss the observation and confirmation of transients for reasons of being intrinsically dim, occurring when the instrument was not observing, poor weather conditions and so on. Therefore, it is crucial to understand the circumstances under which the survey is sensitive in recovering transients. The transient detectability leads to the calculation of a spacetime sensitive volume to particular to the calculation of a spacetime sensitive volume to particular transient types. This depends on properties of the source and its environment, like its brightness or its host galaxy brightness. The instrument cadence and observing schedule are also expected to contribute significantly. A fast cadence is necessary to capture the evolution of, say, an M dwarf flare which last a few minutes, as opposed to a supernova, which evolves for a couple of months.

We consider the intermediate Palomar Transient Factory (iPTF), the successor of PTF and predecessor of ZTF. As a first step, we assess the efficiency of the real-time image subtraction pipeline. We insert fake transients with varying properties into the original iPTF images and then run the pipeline to test recovery. This forms our *single-epoch*

detectability. While this step is similar to the work done for the PTF pipeline by [Frohmaier et al. \(2017\)](#), our analysis differs in final data product for the single-epoch detectability. We make use of supervised machine learning to train a classifier on missed and found fake transients reported by the pipeline to make predictions about the detectability of an arbitrary transient. For completeness, we note that the performance of the survey in the galactic plane is expected to be different from the high latitude fields and requires a separate analysis. The analysis presented in this paper could be applied to only galactic fields to obtain the detection efficiency in the galactic plane. Here, we study the detectability in the high latitude fields or, alternatively, of transients of extra galactic origin. Under such a consideration, this step is independent of the transient type. The multi-epoch observation and detection of a transient can be done using the single-epoch detectability at each epoch. The use of machine learning in this case has advantages in the areas of computing time, determination of systematic errors, ease of improving accuracy at the cost of computing time when required, and handling correlation between training parameters. As a second step, we consider the transient lightcurve evolution. We simulate transient lightcurves in spacetime and use the iPTF observing schedule in conjunction with lightcurves in spacetime and use the iPTF observing schedule in conjunction with this classifier to get the epochs at which the transient is detected. We restrict to type Ia and type IIp supernova lightcurves in this work, the former being the primary result. For the type Ia supernovae (SNe Ia), we impose a minimum number of five epochs of detection brighter than 20th magnitude with at least two during the rise and at least two during the fall of the lightcurve to be a “confirmed” SN Ia. The simulated SNe Ia are used to do a Monte-Carlo integral over spacetime to obtain the space-time SNe Ia are used to do a Monte-Carlo integral over spacetime to obtain the space-time volume sensitivity. For the type IIp supernovae (SNe IIp) lightcurves, the procedure is the same, except we consider a IIp lightcurve recovered if there are at least five epoch observations brighter than 20th magnitude within a span of three weeks during the “plateau” phase.

5.2 The intermediate Palomar Transient Factory

The intermediate Palomar Transient Factory (iPTF) was a survey operated at the Palomar Observatory between late 2012 and early 2017. It had two filters: R (centered at 6581 Å) and g (centered at 4754 Å). It performed fast-cadence experiments resulting in about 300 – 400 exposures on a good night with a nightly output of about 50 – 70 GB. The images were processed by the real-time image subtraction pipeline to report transients within minutes latency. Details are presented in [Nugent et al. \(2015\)](#) and [Cao et al. \(2016\)](#). Here, we give a brief description.

The iPTF real-time image subtraction pipeline (henceforth ISP) was hosted at the National Energy Research Scientific Computing Center (NERSC). A complete exposure of 11 working CCDs was transferred to NERSC immediately after data acquisition to search for new candidates. The pipeline preprocessed the images to remove bias and correct for flat-fielding. It solved for astrometry and photometry, and performed image subtraction using the HOTPANTS algorithm ([Becker, 2015](#)). New candidates were assigned a *real-bogus* classification score between 0 and 1 corresponding to bogus and real respectively ([Bloom et al., 2013](#)). Additionally, candidates would be cross-matched to external catalogs to remove asteroids, active galactic nuclei (AGNs) and variable stars.

5.3 Single-epoch Efficiency

In order to quantify the performance of the iPTF ISP, we perform an end to end simulation using fake transients. We inject fake point source transients in the iPTF images, and then run the pipeline on both the original images and the faked ones. The transients are either missed or found by the ISP. This forms the detectability. We find the efficiency by binning up the parameter space and taking ratio of found to total transients in them. Regarding the mnemonic in subsequent sections, we make a distinction between the terms *detectability* and *efficiency*. Detectability is a decision taken in the sense of a yes/no, while, efficiency

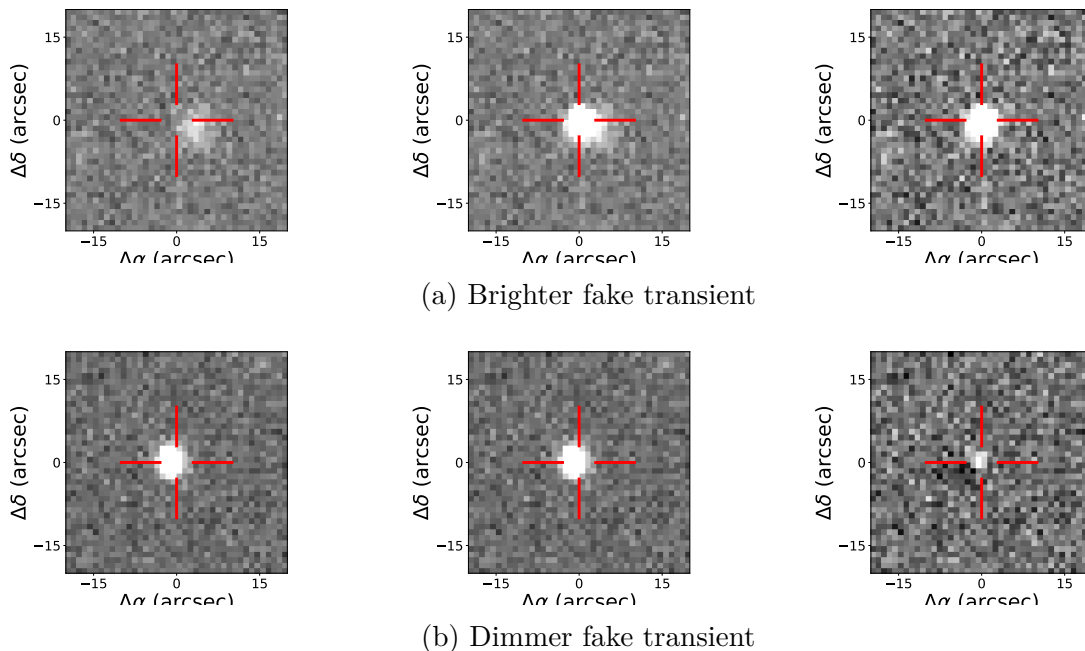


Figure 5.1 An example of an injected transient and the corresponding difference image thumbnail obtained after the image subtraction. The leftmost thumbnail (both panels) is from the original image, the middle thumbnail is a result after a transient is injected, the right thumbnail shows the difference image. The location of the cross-hair is the approximate location where the transient was injected.

is the ratio mentioned above. The former is a binary decision, either of $\{0, 1\}$, while the latter is a quantity $\in [0, 1]$.

5.3.1 Point Source Transients

We follow the *clone stamping* technique used by [Frohmaier et al. \(2017\)](#) for PTF to perform our fake point source injections. The parameters describing these fake transients are *single epoch* - they represent the intrinsic properties of the object and observing conditions at a particular epoch. In other words, here we assess the detectability given the transient was in the field of view of the instrument.

The computational cost for performing injections into all iPTF images and running ISP on them is significant. Therefore, we carry out the process in a single iPTF field 100019.

We choose this field since the distribution of transient population in this field is an accurate representation of the transient population in the sky observed from Palomar (see Fig. 1 of Frohmaier et al. (2017)).

The fake injections are *bright* stars chosen from each original image. These are objects having the following properties:

$$\begin{aligned} m_* \in [13.5, 16] \quad ; \quad \text{CLASS_STAR} \in [0.5, 1.0] \\ \text{FWHM} \in [1.0, 3.0] \quad ; \quad \text{ELLIP} \in [0.0, 0.3]. \end{aligned} \tag{5.1}$$

Here m_* is the apparent magnitude, `CLASS_STAR` is a quantity having a value between 0 (not star-like) and 1 (star like). `FWHM` is the full width at half maximum, in pixels. `ELLIP` is the ellipticity of the object. These quantities are reported after running `SExtractor` (Bertin, E. & Arnouts, S., 1996) on the original images. The reason we choose objects in this range is because we want the point spread function (PSF) to be well estimated, which is the case for bright stars having a high signal to noise ratio $\gtrsim 100$ ($m_* \leq 16$). At the same time we want to avoid pixel saturation, and therefore select stars with $m_* \geq 13.5$. Objects falling in a 50 pixel wide edge boundary are left out since they could potentially be affected by image subtraction artifacts.

A square of side length ~ 9 arc seconds ¹, centered around the star and local-background subtracted, constitutes a *stamp*. A stamp containing any other object apart from the source star is avoided. The local-background refers to that reported by `SExtractor`. The stamp is scaled by an appropriate scaling factor to create a point source transient of desired magnitude. Each transient is allocated a host galaxy ². We follow Frohmaier et al. (2017) regarding the location in the host and place our stamp at a random pixel location within a elliptical radius ³ of 3 pixels. This value contains sufficient amount of the flux

¹More precisely, 9 pixels. 1 pix. $\approx 1.01''$.

²About 50 fake transients were injected in each image; 90% having an associated host galaxy, 10% away from any host galaxy. In this study we only use the injections in host galaxies.

³`KRON_RADIUS` in `SExtractor`

from the galaxy.

This procedure is performed on all the images in field 100019 of iPTF, ten-fold, with a total of $\approx 2.24 \times 10^6$ injected transients. The transient magnitudes are chosen uniformly between 15th and 22nd magnitude with the constraint that the stamp is one magnitude fainter than the original star. We only re-scale to fainter magnitudes because we do not want artifacts like noise residuals from the average background subtraction to be scaled up as noise spikes.

Therefore, m_{inj} follows:

$$m_{\text{inj}} \sim \begin{cases} U(15, 22) & ; m_* \in (13.5, 14) \\ U(m_* + 1, 22) & ; \text{otherwise} \end{cases}. \quad (5.2)$$

An example of an injected transient in a galaxy and the new object recovered by the ISP is shown in Fig. 5.1.

5.3.2 Recovery Criteria

The recovery efficiency ε is defined as the ratio of the number of injections recovered in a part of the parameter space to the total number of injections in that part. Let our injections be described by parameters $\boldsymbol{\lambda}$, then:

$$\varepsilon(\boldsymbol{\lambda}) = \frac{N_{\text{rec}}(\boldsymbol{\lambda})d\boldsymbol{\lambda}}{N_{\text{tot}}(\boldsymbol{\lambda})d\boldsymbol{\lambda}} \quad (5.3)$$

The quantity in the numerator and denominator is the number of recovered and total injections respectively $\in (\boldsymbol{\lambda}, \boldsymbol{\lambda} + d\boldsymbol{\lambda})$. Here $\boldsymbol{\lambda}$ includes both intrinsic source properties of the transient and its environment along with the observing conditions. Examples of intrinsic properties include the magnitude of the transient and the surface brightness of the host galaxy where as those for observing conditions include airmass or sky brightness. While we control fake transient brightness, the observing conditions are those of the images

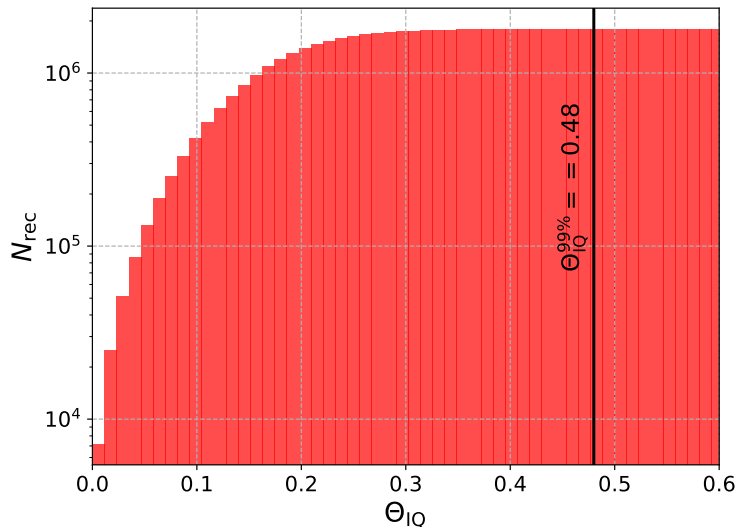


Figure 5.2 The figure shows the cumulative histogram of the quantity Θ_{IQ} , defined as the ratio between the astronomical seeing of the image to that of the reference image as given in Eq.(5.4). The threshold value $\Theta_{IQ}^{99\%} = 0.48$ corresponds to the 99% percentile. We place a constraint of this value when the objects recovered by the pipeline are spatially cross matched to an injected transient.

themselves. Since images across the full survey time are used, the parameter space of the observing conditions is automatically spanned. We determine recovery based on the spatial cross matching of the injections with new objects reported after running the ISP. To determine the tolerance to be imposed during the cross-matching, we define Θ_{IQ} as

$$\Theta_{IQ} = \frac{\sqrt{(x_{inj} - x_{rec})^2 + (y_{inj} - y_{rec})^2}}{\Phi}, \quad (5.4)$$

where Θ_{IQ} is the distance between the injected and the recovered sources in units of the seeing, Φ .

We choose the threshold of Θ_{IQ} such that 99% of the found injections lie within this threshold, which has a value of $\Theta_{IQ}^{99\%} = 0.48$ (see Fig. 5.2). We also impose real-bogus score threshold, $RB2 \geq 0.1$ on the new object. This threshold on RB2 is inspired from survey operation thresholds. Out of the $\approx 2.24 \times 10^6$ injections, we recover $\approx 1.62 \times 10^6$.

5.3.3 Marginalized Efficiency

In this section we discuss the results of the injection campaign mentioned above. We first show some of the *single parameter* efficiencies as a comparison with those obtained for PTF (see Fig. 5 of Frohmaier et al. (2017)). For the joint multi-dimensional detectability, our analysis differs from Frohmaier et al. (2017). We treat the problem of detecting a transient in a single epoch as a *binary classification* problem and use the machinery of supervised learning to predict whether a transient is detected in that epoch.

5.3.4 Single Parameter Efficiencies

The *single parameter* efficiency is the marginalized version of Eq. (5.3). Suppose our parameter of interest is θ and the other “nuisance” parameters are given by $\boldsymbol{\gamma}$, such that in Eq. (5.3), $\boldsymbol{\lambda} = \{\theta, \boldsymbol{\gamma}\}$. The single parameter efficiency is

$$\varepsilon(\theta) = \frac{\left[\int_{\boldsymbol{\gamma}} N_{\text{rec}}(\theta, \boldsymbol{\gamma}) d\boldsymbol{\gamma} \right] d\theta}{\left[\int_{\boldsymbol{\gamma}} N_{\text{tot}}(\theta, \boldsymbol{\gamma}) d\boldsymbol{\gamma} \right] d\theta}. \quad (5.5)$$

In Fig. 5.3 we show the single parameter efficiencies. The expected trend of missing faint transients is seen in the plot for m_{inj} . We find that the recovery efficiency starts to drop for transients by the 20th magnitude and sensitivity is almost nil by the 22nd magnitude.

5.3.5 Multi-dimensional Detectability

In this section, we make a selection of parameters from the full parameter set, $\boldsymbol{\lambda}$, to those on which the detectability depends strongly. In other words, the detectability is a multi-variate function of all the possible parameters which influences the detection of a transient. We identify the minimal set which captures maximum variability. There can be

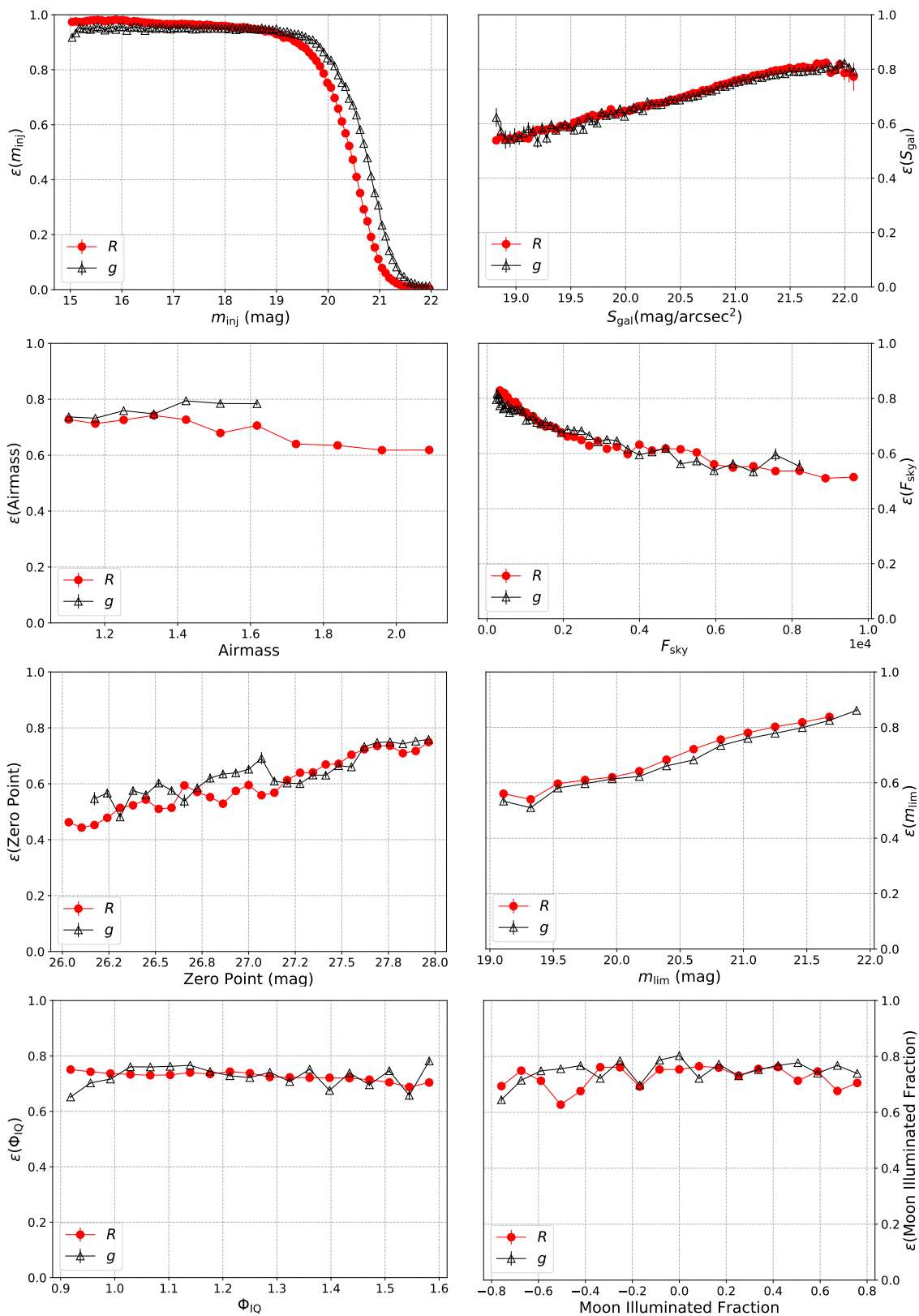


Figure 5.3 The filter specific single parameter efficiencies, defined in Eq. 5.5 are shown here. The top two panels are the intrinsic properties of the transient while the remaining are observing conditions.

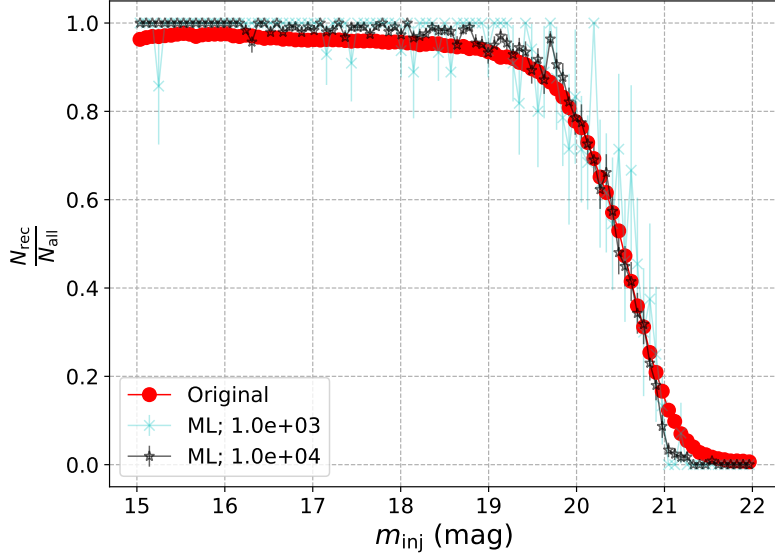


Figure 5.4 Comparison between single parameter efficiency of transient brightness as predicted by trained single-epoch classifier in Eq. (5.7) versus the distribution obtained from the ISP. The original curve has $\sim 10^6$ points used to train the classifier. The ML curves are made by binning the predictions made by the single-epoch classifier on a few thousand random points sampled from the parameter space of the injections (see Eq. (5.6)). Two cases for 10^3 and 10^4 points are shown. We see that the behavior of the classifier converges to that of the ISP within a small sample size ($\lesssim 1\%$ compared to the size of original distribution; see Appendix B for other parameters)

correlations among a pair of parameters. For example, the sky-brightness, F_{sky} and the limiting magnitude, m_{lim} , are correlated - a bright sky hinders the depth and results in a low value of limiting magnitude. The variation of the marginalized efficiencies shown in Fig. 5.3 assist us with the choice of such a parameter set. Since the trend in the single parameter efficiencies are similar to those from PTF, we select the parameters considered by Frohmaier et al. (2017) with a minor difference in the usage of the galaxy surface brightness directly, as used in Frohmaier et al. (2018), in place of the F_{box} ⁴ parameter used in the former. This is justified because our fakes were injected in galaxies.

⁴Background subtracted flux in a 3x3 box in the location of transient.

Training %	Testing %	Avg. mis-classification
75 %	25 %	5.776 %
80 %	20 %	5.760 %
85 %	15 %	5.745 %
90 %	10 %	5.758 %

Table 5.1 The table shows the average misclassification obtained for the `KNearestNeighbor` classifier. The complete dataset contains $\approx 2.24 \times 10^6$ fake point source injections of which $\approx 1.62 \times 10^6$ ($\approx 6.2 \times 10^5$) are found (missed) by the ISP. This is split into respective training and testing fractions. The right-most column shows the fraction of the testing set for which the predictions made by the classifier, trained on the corresponding training fraction differed from the actual value. The misclassification does not change significantly as the size of training data is varied and is attributed mostly to systematics. We quote a conservative value of 6% as the systematic uncertainty of the classifier.

We choose, the following set to represent the dependence of detectability:

$$\boldsymbol{\beta} = \{m, S_{\text{gal}}, F_{\text{sky}}, \Phi_{\text{IQ}}, m_{\text{lim}}\}. \quad (5.6)$$

Here m is the apparent magnitude of the transient, S_{gal} is the host galaxy surface brightness, F_{sky} is the sky brightness, Φ_{IQ} is the ratio of the astronomical seeing to that of the reference image and m_{lim} is the limiting magnitude. The quantities m and S_{gal} are natural in capturing detectability. Sky brightness affects the detectability in a strong way, as is apparent from Fig. 5.3. The Φ_{IQ} parameter captures the variability of the atmosphere. Finally, the limiting magnitude, m_{lim} , although correlated with F_{sky} , captures longer exposure times and status of instrument electronics.

With this set, we use the machinery of supervised learning provided by the `scikit-learn` library (Pedregosa et al., 2011) to train a binary classifier based on the results of the ISP. Once trained, the classifier outputs a probability of detection given arbitrary but physical values of $\boldsymbol{\beta}$. We denote this trained classifier by $\hat{\epsilon}$:

$$\hat{\epsilon} = \hat{\epsilon}(m, S_{\text{gal}}, F_{\text{sky}}, \Phi_{\text{IQ}}, m_{\text{lim}}). \quad (5.7)$$

The `scikit-learn` library provides a suite of classifiers. We choose the non-parametric `KNearestNeighbor` classifier based on speed and accuracy given our large volume of training data. Our complete dataset comprises of $\sim 2.24 \times 10^6$ fake point source injections of which $\sim 1.62 \times 10^6$ ($\sim 6.2 \times 10^5$) are found (missed) by the ISP. We train the classifier using 11 neighbors - twice the number of dimensions plus one to break ties. The observation of a fiducial transient is a point in this parameter space. To decide if that point is “missed” or “found”, we use a majority vote from the nearest 11 neighbors. To cross-validate the performance, the dataset is split into a training set containing 90% of the full dataset, and a testing set containing the remaining 10%. We verified that increasing the number of neighbors does not significantly increase the correctness of predictions made by the classifier. We note that one could use a different threshold for this classification. For example, a different option could be to use greater than 3 “found” neighbors to call the arbitrary point as found. However, it comes at a cost of misclassification. From the predictions of the classifier on the testing set, we find the systematic uncertainty of the classifier to be $\approx 6\%$ i.e. 6 out of 100 predictions made by the classifier is expected to be either true negative or false positive cases. The result does not change much if the size of the training and testing set is varied (see Table 5.1). A comparison between the predictions made by the trained classifier and the original ISP efficiency with the transient magnitude is presented in Fig. 5.4. We see that the behavior of the ISP is reproduced by feeding the classifier with only a few thousand points randomly chosen from the parameter space.

5.4 Type Ia Supernova

Type Ia supernovae are one of the well studied transients in the literature. After the advent of robotic transient surveys, there have been significant additions to the catalog of SNe Ia. They are produced due to thermonuclear detonation of carbon-oxygen white dwarfs with masses close to the Chandrasekhar limit of $\sim 1.4M_{\odot}$. A brief description of the generic

ingredients are given in Sec. 2.2.2. They are remarkably homogeneous in their intrinsic brightness, time, and color evolution. The lightcurve rises to peak light in ~ 20 days with absolute magnitude ~ -19.3 . There are correlations between some of the properties of the lightcurve. For example, brighter SNe Ia have broader width of the lightcurve (Phillips, 1993). Such relations are used to standardize SNe Ia to be used as distance indicators in cosmology.

5.4.1 Explosion Models

The progenitors of SNe Ia are degenerate carbon-oxygen white dwarfs in binary systems. The state of explosion is reached by mass overflow from the companion, known as the the single degenerate route, or by the merger with another white dwarf companion, the double-degenerate route. The reasons for considering the merger of white dwarfs is because they naturally provide an explanation to the absence of hydrogen in the spectra. However, the apparent homogeneity of the lightcurve is not explained as the binary components can have varied composition, mass and angular momenta. The single-degenerate route is favored model which involves an initial low mass accreting white dwarf that eventually reaches the Chandrasekhar mass at the time of explosion. The compressional heating increases the temperature of the core until a nuclear runaway reaction. At $\sim 10^9$ K, the carbon and oxygen burning is initiated resulting in the ignition of the flame. The nuclear burning occurs in thin shells that propagate via detonations and deflagrations. Several scenarios of detonation and deflagrations exist in the literature, and are reviewed, for example, in Hillebrandt & Niemeyer (2000). Subsequent hydrodynamic expansion leads to the expansion velocities $\sim 2 \times 10^4$ km s⁻¹. The star is completely disrupted leaving no compact object behind.

5.4.2 The SALT2 Model

The SALT2 model (Guy et al., 2007) is an empirical model of the photometric and spectroscopic evolution of SNe Ia. They are calibrated using nearby and distant supernovae lightcurves and spectra. The flux evolution is modeled empirically as,

$$F_{\text{SN}}(t, \lambda) = x_0 [M_0(t, \lambda) + x_1 M_1(t, \lambda)] \times \exp [c C_L(\lambda)], \quad (5.8)$$

where x_0 , x_1 , and c are the normalization, stretch, and color parameters. The function M_0 , M_1 and C_L are the average spectral sequence, first order deviations and the the color law obtained from training on known supernovae. The joint lightcurve analysis (Betoule, M. et al., 2014) using SNe from the Supernova Legacy survey (Sullivan, 2004) and the Sloan Digital Sky Survey (Sako et al., 2007) was used to place constrains on the parameters of the above model. This is used to create an ensemble of fake SNe Ia lightcurves to assess their detectability considering multi-epoch observations and the instrument cadence.

5.4.3 Lightcurve Ensemble

We simulate lightcurves with varying intrinsic properties, sky location and redshift, and use the single epoch detectability classifier mentioned in Eq. (5.7) together with the observing schedule of iPTF to determine their sensitivity. The steps are as follows:

1. We simulate lightcurves of varying intrinsic properties over spacetime. spacetime.
2. From the complete iPTF observing schedule, we determine the observations of the evolving lightcurve. This depends on the duty cycle of the instrument. On extended periods with no observations, the simulated lightcurves are missed.
3. We associate a host galaxy with the supernova by choosing a surface brightness value from the distribution of galaxy surface brightness in the survey.

4. Every time the transient is “seen” by iPTF , we feed the combination of the apparent magnitude, host galaxy surface brightness along with the observing conditions at that epoch to the trained single epoch classifier developed in Sec. 5.3. This step, in a sense, mimics the action of the ISP.
5. We call the lightcurve *recovered* when we have at least 5 found observations, all brighter than 20th magnitude, with a minimum of 2 observations on the lightcurve rise and a minimum of 2 on the fall. This is motivated by survey time discoveries.

We also consider type II supernova lightcurves for comparison. Type II supernovae are complex and are further categorized into different subtypes. We consider the IIP subtype because compared to the \sim weeks long variability of SNe Ia, IIP lightcurves vary \sim 100 days and hence is a complimentary case to study. The analysis for the IIPs, however, is simpler compared to Ias.

5.4.4 SN Ia Lightcurves

We use SN Ia lightcurves from the SALT2 model (Guy et al., 2007). In particular, we use the Python implementation of SALT2 provided in `sncosmo` library (Barbary, 2014). This model is based on observations of SNe Ia by the SDSS and SNLS surveys. The free parameters of the model include the stretch (x_1) and color (C) parameters of the SN Ia. Regarding the range of these parameters, we follow same range as Frohmaier et al. (2017) (see Table 1 and Eq.(4) therein). The ranges cover the possible lightcurve morphologies of SNe Ia (Betoule, M. et al., 2014). We show an example lightcurve, at a redshift of $z = 0.01$ with an intrinsic $M_B = -19.05$ in Fig. 5.5. When propagating the flux, we also take into account the extinction due to host galaxy dust and the Milky Way (MW) dust. We use the MW dust map by Fitzpatrick (1999) which is a part of the `sncosmo` package. For the host galaxy extinction, we use the distribution of $E(B - V)$ of SN Ia in their host galaxies (Hatano et al., 1998). Dust extinction plays a significant role in the detectability

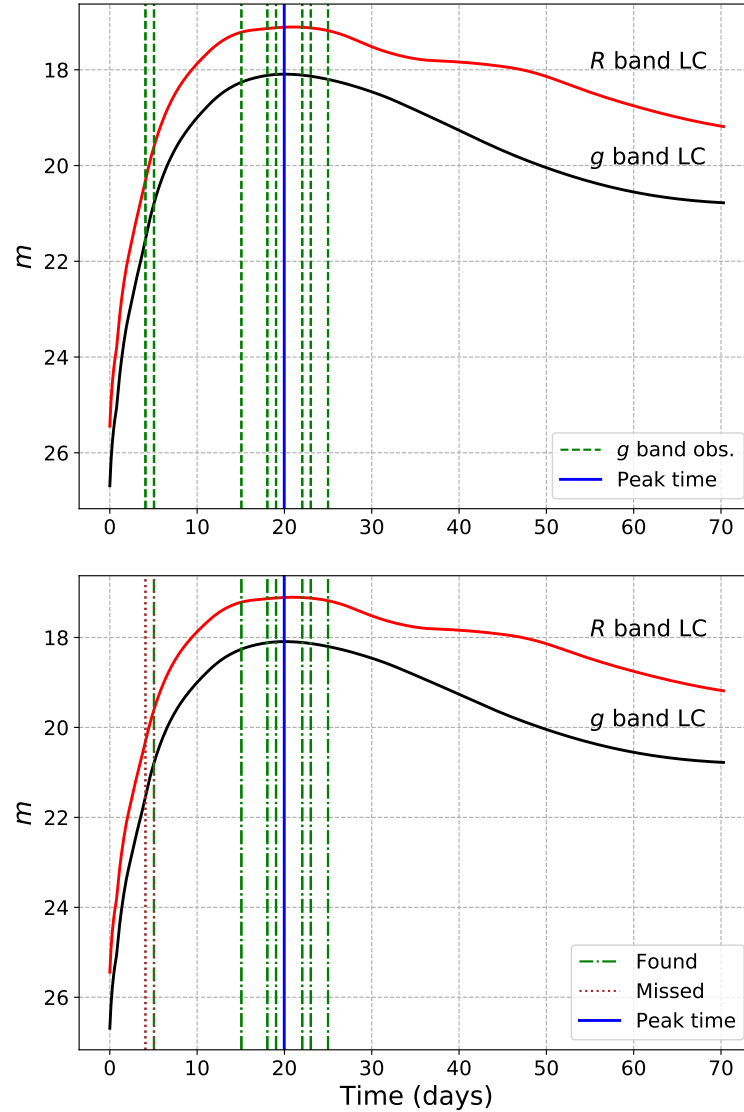


Figure 5.5 **Upper panel:** An example of a SALT2 lightcurve, with the apparent magnitude, m on the y-axis and time on the x-axis. The lightcurves in the iPTF R and g bands are shown. The observations of the telescope are shown as vertical lines. At each observation, we also have the observing conditions of the telescope from archival data. **Lower panel:** The same lightcurve is plotted, however, the vertical lines now represent the detectability from the single epoch classifier. Based on the criteria of confirming a lightcurve as SN Ia, this lightcurve was recovered.

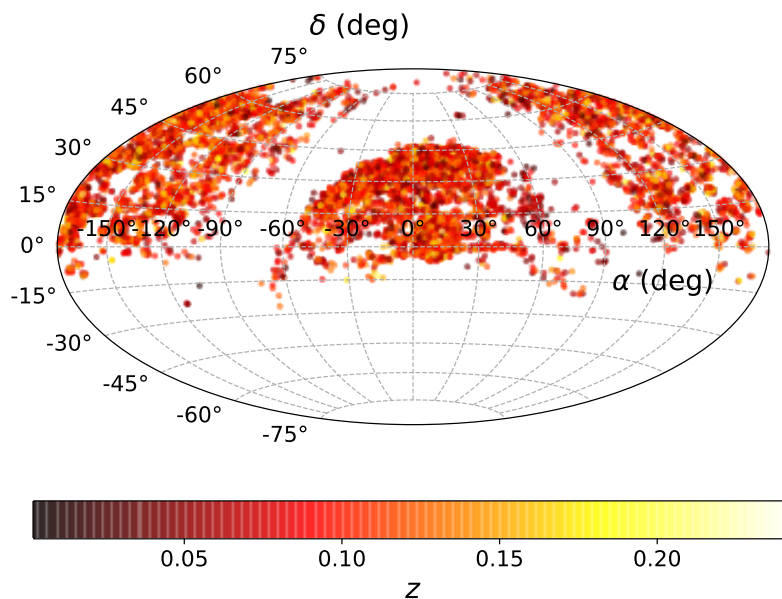


Figure 5.6 An ensemble of SN Ia lightcurves were simulated out to a redshift, $z_{\text{max}}^{\text{Ia}} = 0.28$, uniform in co-moving volume. This figure shows the distribution of the recovered SN Ia in the sky colored by the redshift. The galactic plane can be seen as the half annulus region with no detections.

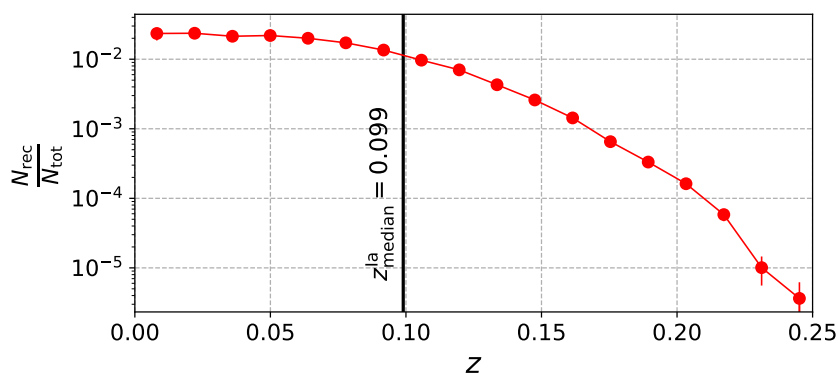


Figure 5.7 Recovery efficiency of the SN Ia lightcurves as a function of redshift, z . The median volume weighted redshift is found to be $z_{\text{median}}^{\text{Ia}} = 0.099$.

of lightcurves as the SNe can be dimmed by as much as 1 – 1.5 magnitudes.

5.4.5 SN Ia Detectability

We simulate $\approx 5 \times 10^6$ SN Ia lightcurves uniformly in co-moving volume up to redshift, $z_{\text{max}}^{\text{Ia}} = 0.28$ ⁵, uniform in peak time distribution in the observer frame. We assume a flat Λ CDM cosmology with Hubble constant, $H_0 = 69.3 \text{ kms}^{-1}/\text{Mpc}$ and matter to critical density, $\Omega_m = 0.287$ (Hinshaw et al., 2013).⁶ We associate a host galaxy surface brightness to each of these SNe using the distribution of surface brightness from iPTF data.

The epochs when the SN Ia is observed come from the iPTF observing schedule. At each observation, we obtain the transient magnitude at that epoch from the lightcurve and the observing conditions from the iPTF survey database. The single epoch classifier then tells us the epochs when the transient was detected. An example is shown in Fig. 5.5 where the vertical lines in the upper and lower panel respectively represent the observations and detections at each epoch.

5.4.6 SN Ia Space-time Sensitive Volume

To understand rates, one must have a good estimate of the survey sensitivity to particular transient types. Let Λ_{SNe} be the expected count of SNe seen during survey time. Then, with R as the intrinsic rate we have:

$$\begin{aligned} \Lambda_{\text{SNe}} &= \int f(t; \underbrace{M_B, z, \dots}_{\kappa}) \overbrace{\frac{dN}{dt_e dV_c}}^R \frac{1}{1+z} \frac{dV_c}{dz} dz dt d\kappa \\ &= R \int f(t; \underbrace{M_B, z, \dots}_{\kappa}) \frac{1}{1+z} \frac{dV_c}{dz} dz dt d\kappa \\ &= R \langle VT \rangle, \end{aligned} \tag{5.9}$$

⁵ The $z_{\text{max}}^{\text{Ia}} = 0.28$ is high enough to capture the spacetime boundary of iPTF sensitivity. Also, no simulations are done below a declination, $\delta_{\text{min}} \approx -31^\circ$ consistent with hardware limitations for iPTF.

⁶ `astropy.cosmology.WMAP9`

where the integral runs over time of observation and co-moving volume up to $z_{\max}^{\text{Ia}} = 0.28$. The *selection* function, $f(\dots) \in \{0, 1\}$, is to be interpreted as the weight assigned to regions in spacetime. The value of the selection function is a consequence of running a spacetime. The value of the selection function is a consequence of running a particular instance of SN Ia through the observing schedule and inferring detectability based on the single-epoch classifier in Eq. (5.7). Therefore, the selection function depends on the observer time, t , which captures the duty cycle and cadence. Also, it depends on the intrinsic properties of the supernova like the absolute intrinsic magnitude, M_B , the redshift, z , at which it was simulated, the sky location and so on. These are collectively represented by $\boldsymbol{\kappa}$ in Eq. (5.9). Since we have distributed the supernovae uniformly in co-moving volume, the integral is approximated in the Monte-Carlo sense:

$$\begin{aligned} \langle VT \rangle &= \int f(t; \underbrace{M_B, z, \dots}_{\boldsymbol{\kappa}}) \frac{1}{1+z} \frac{dV_c}{dz} dz dt d\boldsymbol{\kappa} \\ &\approx \frac{N_{\text{rec}}}{N_{\text{tot}}} T \int \frac{1}{1+z} \frac{dV_c}{dz} dz, \end{aligned} \quad (5.10)$$

where N_{rec} is the number of SNe recovered from this simulation campaign, N_{tot} is the total number simulated and T is the four year period of iPTF over which we performed the simulations.⁷ We obtain the result,

$$\langle VT \rangle_{\text{Ia}} = 2.93 \pm 0.21 \times 10^{-2} \text{ Gpc}^3 \text{ yr}, \quad (5.11)$$

where the error includes the $\sim 1/\sqrt{N}$ statistical error from Monte Carlo integration and the 6% systematic error of the single epoch detectability classifier computed in Sec. 5.3.5, the latter being the dominant source of error. The distribution of the detected SNe Ia in sky is shown in Fig. 5.6 colored by redshift. Using the recovered SNe Ia, the median sensitive co-moving volume is found to be 0.305 Gpc^3 . We report the redshift corresponding to this

⁷More specifically, Oct 23, 2012 to Mar 3, 2017 \Rightarrow 1592 days

value as the median sensitive redshift to SNe Ia, $z_{\text{median}}^{\text{Ia}} = 0.099$, shown in Fig. 5.7.

5.5 Other Transient Lightcurves

5.5.1 Type IIp Supernova Lightcurves

In contrast to the well-defined Ia lightcurves with their typical timescales of several weeks, we also wanted to explore longer-timescale lightcurves as a limiting case. Therefore, we consider type IIp supernovae and compute their spacetime sensitive case. Therefore, we consider type IIp supernovae and compute their spacetime sensitive volume in similar lines as Sec. 5.4.5. A brief highlight of the general features of core-collapse supernova is mentioned in Sec. . In general, type II supernovae (SNe II) vary in lightcurve morphology and are categorized in various subtypes (Li et al., 2011). Specifically, type IIp lightcurves have a distinct “plateau” feature after the rise lasting for about 100 days after explosion, as shown in Fig. 5.8. The intrinsic brightness, $M_B \sim -16.75$, is significantly lower than that of SNe Ia (Richardson et al., 2014). Among the SNe II, the IIp subclass is the most common explosion by volume. Their progenitors are thought to be red super giant stars (Smartt, 2009).

Due to their overall low intrinsic luminosity, we expect the spacetime sensitive Due to their overall low intrinsic luminosity, we expect the spacetime sensitive volume to be lower than that of the SNe Ia. When considering the Ia lightcurves in Sec. 5.4.4, the SALT2 model parameters were used to tune possible lightcurve morphologies. Here we take a simpler approach and consider a time-series model from Gilliland et al. (1999) (named `nugent-sn2p` in the `sncosmo` library) to compute the flux up to 100 days from the explosion time. Thus, while simulating the SNe IIp in spacetime, the only change to the Thus, while simulating the SNe IIp in spacetime, the only change to the lightcurve shape is the depending on the cosmological redshift and host and Milky Way extinction properties.

We simulate $\sim 9.1 \times 10^5$ SN IIp lightcurves uniform in sky location, observer time and

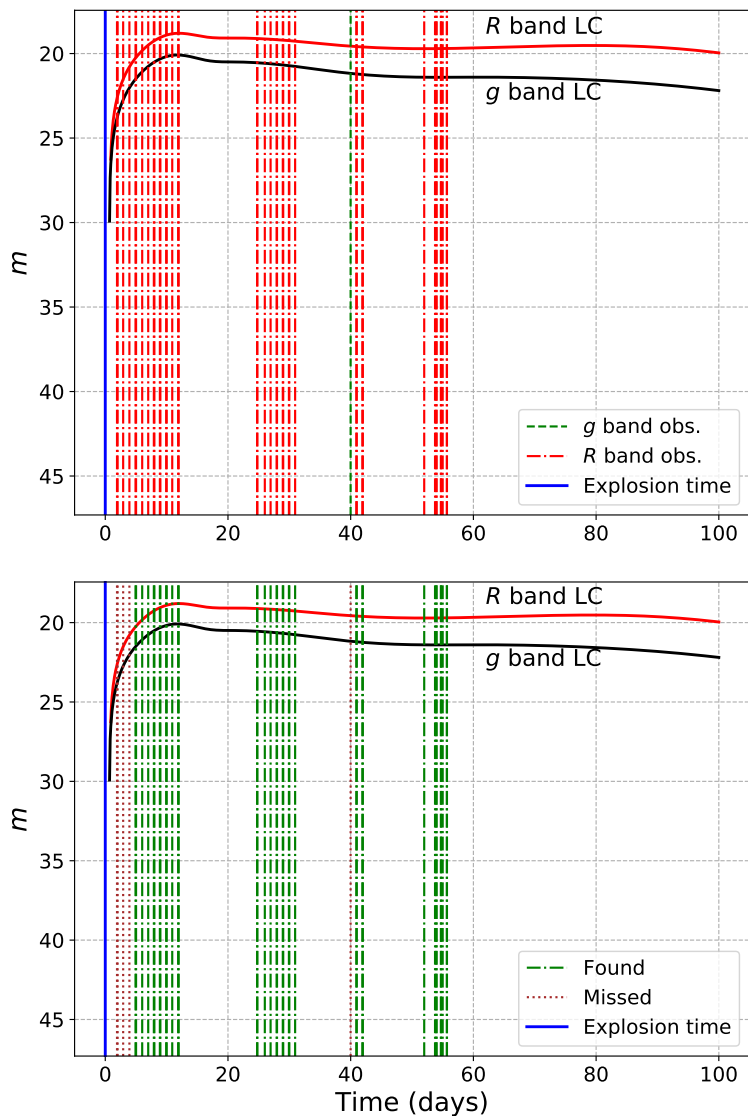


Figure 5.8 **Upper panel:** An example of a SN IIP lightcurve, with the apparent magnitude, m on the y-axis and time on x-axis. The lightcurve is shown in the iPTF R and g bands. The observations of the telescope are shown as vertical lines. **Lower panel:** The same lightcurve is plotted, however, the vertical lines now represent the recovery by single epoch classifier. One can identify the only g band observation (around 40 days) being missed due to fainter magnitude in the g band.

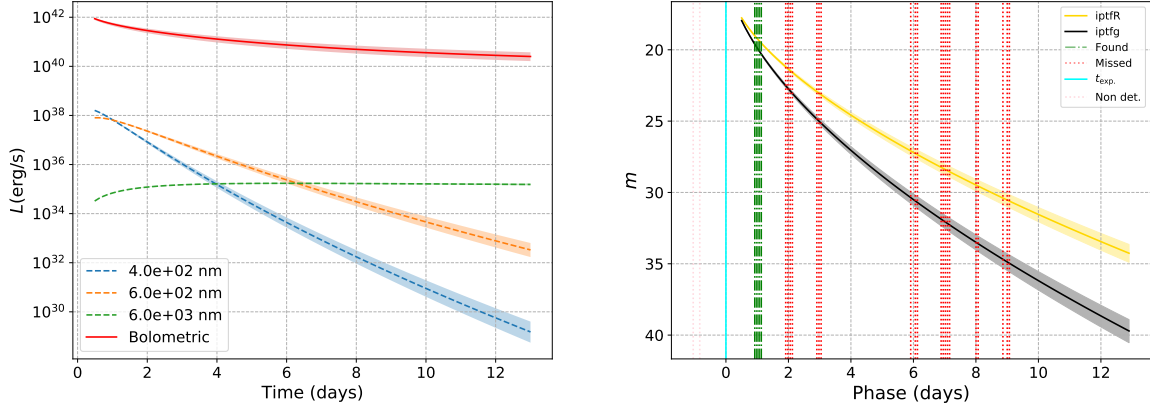


Figure 5.9 **Left panel**: This figure shows a simple model for a kilonova lightcurve. It is based on AT 2017gfo lightcurve evolution based on the best-fit blackbody parameters from Kasliwal et al. (2017). **Right panel**: The lightcurve in the iPTF R and g bands. The vertical lines represent the observations made by iPTF and whether the transient was detected each epoch of observation.

co-moving volume up to a redshift, $z = 0.1$. Like the SNe Ia, each SN IIP is assigned a host galaxy surface brightness from the surface brightness distribution of galaxies in iPTF and a $E(B - V)$ extinction value from IIP extinction distribution in Hatano et al. (1998). In this case, we use the criteria that the lightcurve must be recovered a minimum of five epochs, brighter than 20th magnitude in a span of 3 weeks within the 100 days post explosion. The iPTF observing schedule along with the single-epoch classifier is used to compute the detectability in each epoch. We obtain the result:

$$\langle VT \rangle_{\text{IIP}} = 7.80 \pm 0.76 \times 10^{-4} \text{ Gpc}^3 \text{ yr}, \quad (5.12)$$

where the error includes the statistical error from the Monte-Carlo integration and the 6% systematic uncertainty from the single-epoch classifier (see Sec. 5.3.5). The median sensitive redshift is found to be $z_{\text{median}}^{\text{IIP}} = 0.038$.

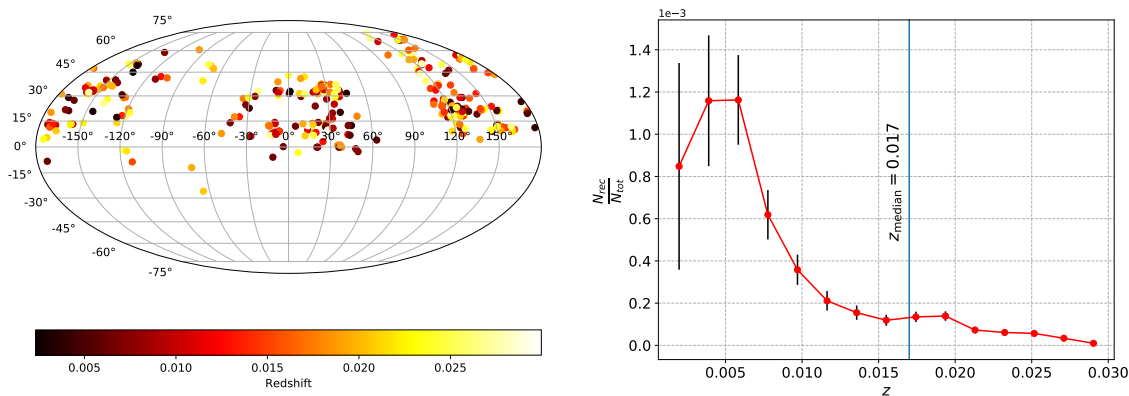


Figure 5.10 **Left panel:** This figure shows the sky location of the found kilonova lightcurves colored by their cosmological redshift, z . **Right panel:** The fractional recovery of kilonova lightcurves as a function of redshift. The volume weighted sensitive median redshift is $z_{\text{median}} = 0.017$ which corresponds to a luminosity distance of ≈ 72 Mpc.

5.5.2 Kilonova Lightcurves

The above procedure is generally applicable given a lightcurve evolution model. While supernovae have been studied extensively, transient surveys have begun to discover more interesting fast transients. After the discovery of GW170817 (see Sec. 2.3) there has been considerable interest in studying the sensitivity of transient surveys to kilonovae from their nightly operations i.e., a blind search. Given the low intrinsic luminosities and the fast decay, the spacetime sensitivity is expected to be much lower that of supernovae.

The modeling of kilonovae is at its infancy. Here we consider a simple lightcurve model based on best-fit blackbody parameters to the temperature evolution of AT 2017gfo from Kasliwal et al. (2017) shown in Fig. 5.9. Regarding the conditions for detectability, we demand at least three epoch confirmed detection consistent with fading, and a non-detection one week before the explosion time. We performed fake simulations of this model in the same lines as the SNe Ia and SNe IIP simulations. Out of the $\sim 3 \times 10^6$ simulations performed, only $\gtrsim 300$ instances were recovered. In Fig. 5.10 we show the recovered lightcurves colored by the redshift. Since the transients are distributed uniform in comoving volume, this corresponds to a $\propto z^2$ distribution along the redshift. The decreasing

efficiency and the increasing population results in a peak in the fractional recovery. The redshift corresponding to the median sensitive comoving volume gives the median sensitive redshift, $z_{\text{median}} = 0.017$. This gives a luminosity distance ≈ 72 Mpc. Thus a candidate like AT 2017 gfo at 40 Mpc would have been observed by a survey like iPTF.

5.6 Rates

5.6.1 Likelihood Calculation

In this work, we provide a methodology to assess the transient detectability taking into account the intrinsic transient properties and the observing conditions of fast cadence transient surveys. This is done by injecting fake point source transients into the images, running image subtraction on them and finding out the parameter space where they are found by the image subtraction pipeline. The joint detectability is evaluated using the machinery of supervised machine learning trained on the missed and found fake transients. This step mimics the action of the image subtraction pipeline at every epoch and forms the single-epoch detectability. Consequently, the lightcurve morphology and the survey observing schedule is used to compute the spacetime volume sensitivity of particular is used to compute the spacetime volume sensitivity of particular transients. We consider the case of the intermediate Palomar Transient Factory (iPTF) and evaluate the single-epoch detectability and then use its observing schedule to compute the spacetime volume sensitivity use its observing schedule to compute the spacetime volume sensitivity of type Ia supernovae (SNe Ia). We also do a preliminary analysis of type IIp supernovae (SNe IIp). Note that the spacetime volume sensitivity type IIp supernovae (SNe IIp). Note that the spacetime volume sensitivity could be computed for any general transient, using its lightcurve morphology; SN Ia or IIp is an example. In the case of SNe Ia, the remaining piece in the estimation of the volumetric rate is a systematic number count to be obtained via an archival search into iPTF data. While we defer this to a future work, we outline

our plan of action here.

5.6.2 Rate Posterior

The computation of the rate posterior assumes the likelihood of observing N candidate events is an inhomogeneous Poisson process (Loredo & Wasserman, 1995; Farr et al., 2015). Our *search* will filter the SN Ia population based on the model SALT2 model used previously at the expense of some contamination from other transient types, potentially with similar lightcurve morphologies. If the mean count of these impurities is Λ_0 , the likelihood function is:

$$p(N|\Lambda_0, \Lambda_{\text{SNe}}) \propto (\Lambda_0 p_0 + \Lambda_{\text{SNe}} p_{\text{SNe}})^N \times \exp(-\Lambda_0 - \Lambda_{\text{SNe}}), \quad (5.13)$$

where p_{SNe} (p_0) is the *a priori* weight that a transient is (isn't) a SN Ia after the filtering process. With a suitable choice of prior, we can use Bayes' theorem to obtain the posterior. Considering the Jeffreys' prior:

$$p(\Lambda_0, \Lambda_{\text{SNe}}) = \frac{1}{\sqrt{\Lambda_0}} \frac{1}{\sqrt{\Lambda_{\text{SNe}}}}, \quad (5.14)$$

the posterior takes the form:

$$\begin{aligned} p(\Lambda_0, \Lambda_{\text{SNe}}|N) &\propto p(N|\Lambda_0, \Lambda_{\text{SNe}}) p(\Lambda_0, \Lambda_{\text{SNe}}) \\ &\propto \frac{(\Lambda_0 p_0 + \Lambda_{\text{SNe}} p_{\text{SNe}})^N}{\sqrt{\Lambda_0 \Lambda_{\text{SNe}}}} \\ &\quad \times \exp(-\Lambda_0 - \Lambda_{\text{SNe}}). \end{aligned} \quad (5.15)$$

Integrating out the nuisance parameter, Λ_0 , we have the marginalized posterior on $\Lambda_{\text{SNe}} = R\langle VT \rangle$, or equivalently on R :

$$\begin{aligned}
 p(R|N) &= \int_0^\infty p(\Lambda_0, \Lambda_{\text{SNe}}|N) d\Lambda_0 \\
 &\propto \frac{e^{-R\langle VT \rangle}}{\sqrt{R\langle VT \rangle}} \times \left[(R\langle VT \rangle p_{\text{SNe}})^N + \frac{N}{2} p_0 (R\langle VT \rangle p_{\text{SNe}})^{N-1} \right], \tag{5.16}
 \end{aligned}$$

where we expand Eq. (5.15) and integrate, keeping terms up to linear order in p_0 since we expect that $p_0 \ll p_{\text{SNe}}$.

5.6.3 Approximate SN Ia Count in iPTF

Type Ia supernova rates have been studied earlier in the literature (Dilday et al., 2008; Gal-Yam et al., 2007; Brown et al., 2019). Deep field instruments have provided estimates of the Ia rate out to high redshift (Gal-Yam et al., 2007). The intermediate Palomar Transient Factory, being an all sky survey has a comparatively lower sensitivity to SNe Ia at $z_{\text{median}}^{\text{Ia}} = 0.099$. The SDSS-II supernova survey has estimated the volumetric SN Ia rate at $z \approx 0.1$ to be $R_{\text{SNIa}}^{\text{SDSS-II}} \sim 2.9_{-0.75}^{+1.07} \times 10^{-5} \text{Mpc}^{-3} \text{yr}^{-1}$ (Dilday et al., 2008). Using our estimate of the spacetime sensitive volume from Eq. (5.11), an estimate of the spacetime sensitive volume from Eq. (5.11), an estimate of the count of SNe Ia in iPTF is 630 – 1160. This is consistent with 1035 objects tagged “SN Ia” during the survey time.

5.6.4 Future Work

While the number of transients tagged as “SN Ia” by human scanners during iPTF survey time seem consistent with our ballpark above, the systematic uncertainty of such a classification remains unquantified. The quantities p_0 , p_{SNe} and N in Eq. (5.16) require a systematic search into the iPTF archival data to retrieve the candidate count and system-

atic errors associated with such a classification. We defer this and the computation of SN Ia volumetric rate to a future work in the series. The methodology developed here facilitates the computation of spacetime The methodology developed here facilitates the computation of spacetime volume sensitivities of general transient types. Of particular interest are the fast transients in iPTF archival data as discussed in [Ho et al. \(2018\)](#). Also, the observation of the “kilonova” resulting from the binary neutron star merger, GW170817 ([Abbott et al., 2017](#); [Abbott et al., 2017a,b](#)), star merger, GW170817 ([Abbott et al., 2017](#); [Abbott et al., 2017a,b](#)), hints towards the association of transients to binary neutron star mergers. There is no evidence of detection of such a transient in the iPTF data, in which case rate upper limits could be placed due to non-detection.

Chapter 6

Conclusion

The direct observation of GW in 2015 was a milestone in the field of gravitation. It bore truth to the century old prediction made by Einstein, and was another triumph of general relativity. It opened an entirely new messenger to study the universe, analogous to Galileo using the telescope to observe celestial bodies in the 1600s, pioneering modern day astronomy. The field has moved in leaps and bounds over the (barely) five years since the discovery. It can be said in some sense that we have moved from the era of GW discovery to GW astronomy at the time of writing. The recently concluded LIGO/Virgo third observing run reported 56 public candidates. This is more than five-fold increase in the number of events from the first and second observing runs combined and corresponds to detection of over 5 candidates per months on average during regular operating cycle. The detection of GW170817, and the unprecedented follow-up bore the first observational evidence that merger of compact binaries could have an associated EM counterpart. This meant that GW astronomy entered the sector of time-domain astronomy. Infrastructure was developed to enable rapid communication between GW and partner facilities to enable prompt follow-up of GW transients. This marked yet another milestone of the dawn of multi-messenger astronomy using GWs. Targeted observations using GWs present a unique way to hunt the rapidly evolving associated kilonova, GRB afterglows, and other

possible messengers. In this thesis, it is the prospect of multi-messenger astronomy using GWs that I research on. In particular, I focus on development of tools and infrastructure that facilitate follow-up operations for GW candidates from LIGO/Virgo. In Chapter 3 the inference of source properties from the realtime GW data is developed to assess the possibility of EM counterparts of compact object mergers. Such information is crucial for partner facilities to schedule observations. In Chapter 4, the problem of hunting these counterparts is considered from the point of view of partner facilities. A tiling strategy is developed for ZTF in the pursuit of GW events. Also, by performing a set of simulated signals, it is concluded that longer integration times for the telescope increases chances of detecting the kilonova. In Chapter 5, we study another piece of the puzzle – the detection efficiency of a survey. For a time-domain survey this depends on intrinsic properties of the transient, its photometric and spectral evolution, and also on weather conditions. A robust understanding of the detection efficiency of fast transients like kilonovae is of paramount importance to design observing strategies to succeed in hunting EM counterparts of GW transients. While we are in the era of GW astronomy, we are still not in an era of routine multi-messenger detections. In going ahead tools and strategies like those developed in this thesis will be of useful for follow-up operations.

6.1 Future Work

6.1.1 Machine Learning

Over the last decade machine learning has found importance in various avenues of physics and astronomy. Extracting signal from noise, or dealing with instrument or algorithm selection biases is common across most experiments today. A robust handle on these selection effects require large scale expensive computer simulations. Machine learning can help in this regard. Some of the work in this thesis has made extensive use of traditional open source machine learning algorithms to achieve good results. However, a natural

extension of work in Chapter 3 is to use recently popularized deep learning algorithms like convolutional neural networks to handle selection effects.

6.1.2 EoS Weighted Source Properties

The source properties in Chapter 3 used an assumption about the NS EoS. To be conservative, a stiff EoS, 2H, was chosen. The 2H is not astrophysically motivated, but was used to provide a conservative answer to the property of the binary leaving remnant matter post merger. This is because the detection uncertainty of realtime parameters are much larger compared to difference caused due to the choice of an EoS. This is to be reanalyzed in the light of new results from the third observing run. A better approach is to consider several EoS models, or to marginalize over the EoS by obtaining a weighted average of the results from using different EoS models.

6.1.3 Supernova Rates

In Chapter 5, we evaluated the spacetime sensitive volume of iPTF to SNe Ia. The rate estimation was deferred to a future work. An archival search is required to evaluate the number of candidates in iPTF that fit the SALT2 model. The procedure is laid out in Sec. 5.6.2. The archival search would give the efficiency and the impurity fraction of the search to pick out SNe Ia from archival data which is required to obtain the posterior on the rate.

6.2 Looking Ahead

The next decade promises routine multi-messenger observations using GW observations of compact binary mergers. Next generation telescope surveys like ZTF and the Rubin Observatory will be able to make deep and fast routine observations for transients. This will be complemented by $\sim 160 - 190$ Mpc sensitivity of LIGO/Virgo sensitivity in the

fourth observing run. The science output of GWs and multi-messenger observations is interdisciplinary, touching the avenues of fundamental physics, nuclear physics and gravity, to astronomy and cosmology. On the fundamental physics and gravity aspect, the joint detection of EM counterparts and GWs provide constraints on the speed of gravity, the future four-detector network will make good measurements of the GW polarization to constrain alternate gravity models. Tidal deformability measurements of GW will provide a direct method to measure the NS equation of state. This will also be complemented by EM studies of the photometric and spectroscopic evolution of the kilonova. Model selection in this regard would require input from nuclear theory and lattice quantum chromodynamics models. GWs in combination with counterpart observation will provide an independent measurement of the Hubble constant, H_0 . This is of paramount importance at this point in cosmology given the growing tension in the inferred value of H_0 from the cosmic microwave background and type Ia supernovae. Future GW-GRB coincidences will give more insight into the short GRB progenitors and the GRB engine. There are also prospects of constraining dark matter using EMGW observations, like the observation of primordial black holes which could produce binaries similar to NS masses but don't produce EM counterparts. The growing number of observations will put tight constraints on the population of compact binaries and their evolution over cosmic time. Finally, there is always the possibility of detecting the unexpected like an observation of binaries in the putative $3 - 5M_\odot$ mass-gap, objects made out of more exotic matter like quark stars, or a totally unexpected EM transient.

Appendix A

Behavior Of Trained Classifier With SNR

A.1 Parameter Sweep

In this section, we make in extension of the parameter sweep results shown in Fig. 3.4. Here we sweep over the (m_1, m_2) values but keep the values of the spins fixed, only varying the signal-to-noise (SNR). The result is shown in Fig. A.1. It is expected that the uncertainty in the recovered parameter should decrease with the increase in SNR which manifests as a decrease in the *fuzzy* region separating the *bright* ($p(\text{HasNS}) = 1/p(\text{HasRemnant}) = 1$) and *dark* ($p(\text{HasNS}) = 0/p(\text{HasRemnant}) = 0$) regions.

A.2 GstLAL Injection Sets

In this section, we report the calendar dates for the injection sets used in this study. These are tabulated in Table A.1. The chunks cover most of the duration of the observing run, although they may not be contiguous corresponding to break in the observing run. Three detector injections were performed about the last ~ 1 month of the second observing run. Thus, their length and hence the missed found injections are smaller in number. As a future

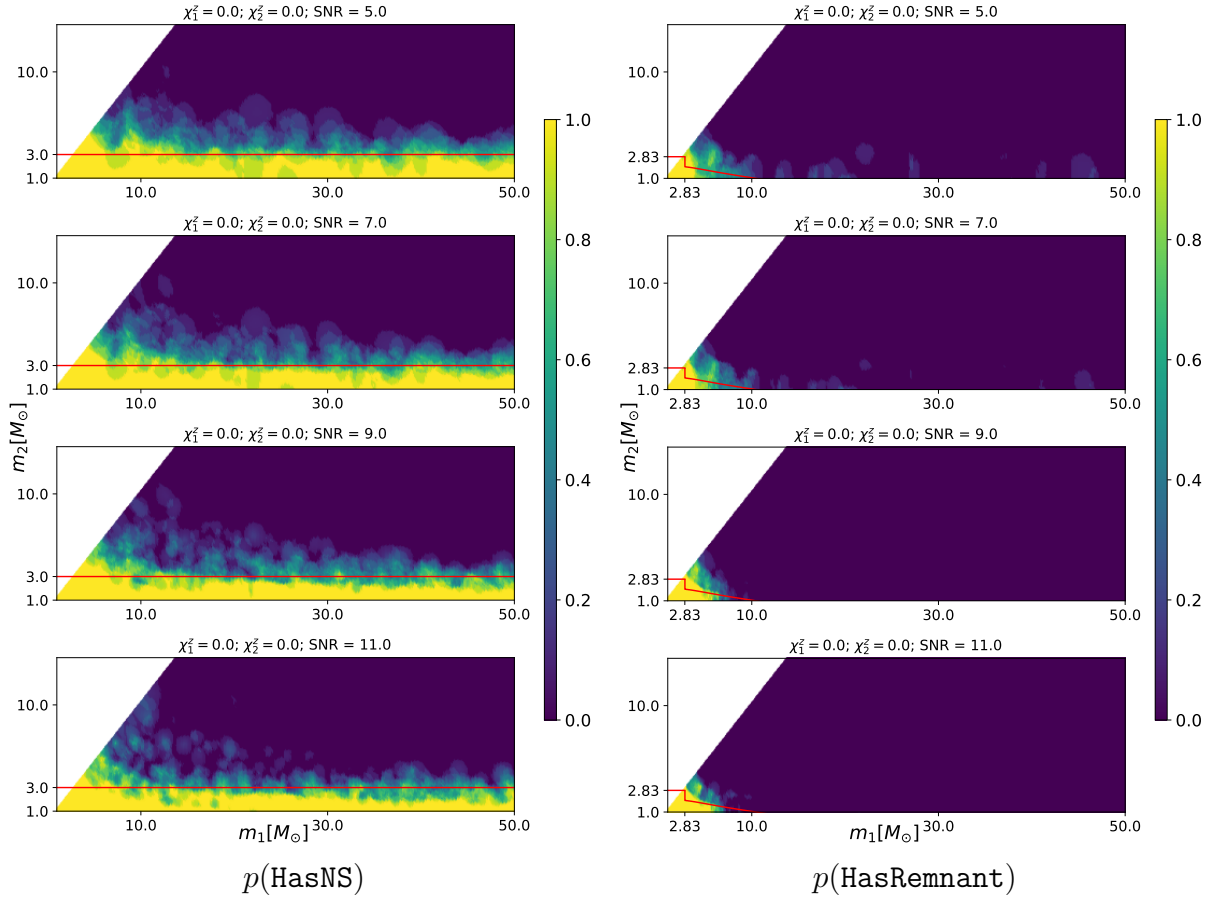


Figure A.1 This figure is an extension of Fig. 3.4. Here we see the behavior of the predictions from the binary classifiers as the signal to noise (SNR) of recovery increases. **Left panel:** Variation in $p(\text{HasNS})$ with SNR. **Right panel:** Variation in $p(\text{HasRemnant})$ with SNR.

A.2. *GstLAL Injection Sets*

GstLAL chunk	Start date	End date
Chunk 02	Wed Nov 30 16:00:00 GMT 2016	Fri Dec 23 00:00:00 GMT 2016
Chunk 03	Wed Jan 04 00:00:00 GMT 2017	Sun Jan 22 08:00:00 GMT 2017
Chunk 04	Sun Jan 22 08:00:00 GMT 2017	Fri Feb 03 16:20:00 GMT 2017
Chunk 05	Fri Feb 03 16:20:00 GMT 2017	Sun Feb 12 15:30:00 GMT 2017
Chunk 06	Sun Feb 12 15:30:00 GMT 2017	Mon Feb 20 13:30:00 GMT 2017
Chunk 07	Mon Feb 20 13:30:00 GMT 2017	Tue Feb 28 16:30:00 GMT 2017
Chunk 08	Tue Feb 28 16:30:00 GMT 2017	Fri Mar 10 13:35:00 GMT 2017
Chunk 09	Fri Mar 10 13:35:00 GMT 2017	Sat Mar 18 20:00:00 GMT 2017
Chunk 10	Sat Mar 18 20:00:00 GMT 2017	Mon Mar 27 12:00:00 GMT 2017
Chunk 11	Mon Mar 27 12:00:00 GMT 2017	Tue Apr 04 16:00:00 GMT 2017
Chunk 12	Tue Apr 04 16:00:00 GMT 2017	Fri Apr 14 21:25:00 GMT 2017
Chunk 13	Fri Apr 14 21:25:00 GMT 2017	Sun Apr 23 04:00:00 GMT 2017
Chunk 14	Sun Apr 23 04:00:00 GMT 2017	Mon May 08 16:00:00 GMT 2017
Chunk 15	Fri May 26 06:00:00 GMT 2017	Sun Jun 18 18:30:00 GMT 2017
Chunk 16	Sun Jun 18 18:30:00 GMT 2017	Fri Jun 30 02:30:00 GMT 2017
Chunk 17	Fri Jun 30 02:30:00 GMT 2017	Sat Jul 15 00:00:00 GMT 2017
Chunk 18	Sat Jul 15 00:00:00 GMT 2017	Thu Jul 27 19:00:00 GMT 2017

Table A.1 The table contains the calendar times for the GstLAL fake injection datasets.

work, we plan to re-analyze the performance of the classifier based on injection campaigns in the third observing run as they are performed.

Appendix B

Single Epoch Performance

In Fig. 5.4, we made a comparison between the marginalized single parameter efficiency for the single-epoch transient brightness from the classifier predictions. Here, we show it for the remaining parameters. While the final classifier is trained on the full dataset, to make the comparison, we train it on 90% of the total fake point source simulations we performed, as mentioned in Sec. 5.3.1. From the remaining 10% sample size, we make a random selection of points (progressively increasing), feed them to the classifier and bin the results in the same manner as in Fig. 5.3 to compare marginalized efficiency plots. These are shown in Fig. B.1 and Fig. 5.4, the latter presented earlier. We see that the behavior starts to converge to that of the ISP in a few thousand points.

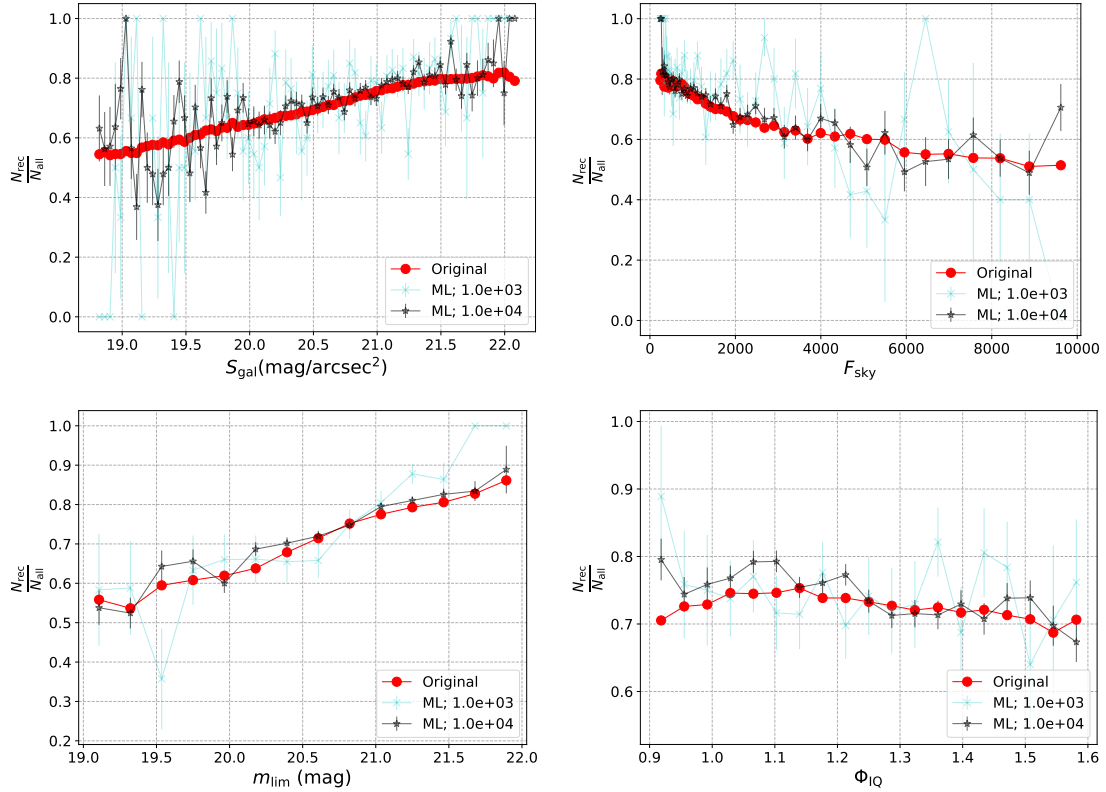


Figure B.1 This figure is an extension of Fig. 5.4. We compare the performance of the marginalized single parameter efficiency of the trained classifier compared to that of the original distributions in Fig. 5.3. We see the behavior of the ISP being reproduced by feeding the classifier a few thousand points.

Bibliography

- Aasi, J., Abbott, B. P., Abbott, R., et al. 2015, *Classical and Quantum Gravity*, 32, 074001
- Abadie, J., Abbott, B. P., Abbott, R., et al. 2010, *Physical Review D*, 82, doi:10.1103/physrevd.82.102001
- Abbott, B. P., Abbott, R., Abbott, T. D., Abernathy, M. R., et al. 2018, *Living Reviews in Relativity*, 21, 3
- Abbott, B. P., Abbott, R., Abbott, T. D., et al. 2019, *Phys. Rev. X*, 9, 031040
- . 2016a, *Phys. Rev. X*, 6, 041015
- . 2016b, *The Astrophysical Journal*, 826, L13
- . 2016c, *Phys. Rev. Lett.*, 116, 061102
- . 2017a, *The Astrophysical Journal*, 850, L39
- . 2017b, *The Astrophysical Journal*, 848, L13
- Abbott, B. P., Abbott, R., Abbott, T. D., et al. 2017, *The Astrophysical Journal Letters*, 848, L12
- Abbott, B. P., Abbott, R., Abbott, T. D., et al. 2017, *The Astrophysical Journal Letters*, 850, L40
- . 2018, *Phys. Rev. Lett.*, 121, 161101
- Abdikamalov, E., Gossan, S., DeMaio, A. M., & Ott, C. D. 2014, *Physical Review D*, 90, doi:10.1103/physrevd.90.044001
- Acernese, F., et al. 2014, *Classical and Quantum Gravity*, 32, 024001
- Adams, T., Buskulic, D., Germain, V., et al. 2016, *Classical and Quantum Gravity*, 33,

175012

Amaro-Seoane, P., Audley, H., Babak, S., et al. 2017, Laser Interferometer Space Antenna, arXiv:1702.00786

Arcavi, I., Hosseinzadeh, G., Howell, D. A., et al. 2017, *Nature*, 551, 64

Arnett, W. D. 1980, *The Astrophysical Journal*, 237, 541

—. 1982, *The Astrophysical Journal*, 253, 785

Ashton, G., Hübner, M., Lasky, P. D., et al. 2019, *The Astrophysical Journal Supplement Series*, 241, 27

Barbary, K. 2014, sncosmo v0.4.2, doi:10.5281/zenodo.11938

Barbieri, C., Salafia, O. S., Perego, A., Colpi, M., & Ghirlanda, G. 2019, *Astronomy & Astrophysics*, 625, A152

Barnes, J., & Kasen, D. 2013, *The Astrophysical Journal*, 775, 18

Becker, A. 2015, HOTPANTS: High Order Transform of PSF ANd Template Subtraction, ascl:1504.004

Bellm, E. C. 2014, in *The Zwicky Transient Facility*

Berger, E. 2014, *Annual Review of Astronomy and Astrophysics*, 52, 43

Bernardini, M. G. 2015, *Journal of High Energy Astrophysics*, 7, 64 , swift 10 Years of Discovery, a novel approach to Time Domain Astronomy

Bertin, E., & Arnouts, S. 1996, *Astron. Astrophys. Suppl. Ser.*, 117, 393

Betoule, M., Kessler, R., Guy, J., et al. 2014, *A&A*, 568, A22

Biwer, C. M., Capano, C. D., De, S., et al. 2019, *Publications of the Astronomical Society of the Pacific*, 131, 024503

Blandford, R. D., & Znajek, R. L. 1977, *Monthly Notices of the Royal Astronomical Society*, 179, 433

Bloom, J. S., Brink, H., Richards, J. W., et al. 2013, *Monthly Notices of the Royal Astronomical Society*, 435, 1047

Bohé, A., Shao, L., Taracchini, A., et al. 2017, *Phys. Rev. D*, 95, 044028

- Brown, J. S., Kochanek, C. S., Stanek, K. Z., et al. 2019, *Monthly Notices of the Royal Astronomical Society*, 484, 3785
- Buonanno, A., Iyer, B. R., Ochsner, E., Pan, Y., & Sathyaprakash, B. S. 2009, *Phys. Rev. D*, 80, 084043
- Cao, Y., Nugent, P. E., & Kasliwal, M. M. 2016, *Publications of the Astronomical Society of the Pacific*, 128, 114502
- Chatterjee, D., Ghosh, S., Brady, P. R., et al. 2019a, arXiv e-prints, arXiv:1911.00116
- Chatterjee, D., Nugent, P. E., Brady, P. R., et al. 2019b, *The Astrophysical Journal*, 881, 128
- Cho, H.-S., Ochsner, E., O’Shaughnessy, R., Kim, C., & Lee, C.-H. 2013, *Phys. Rev. D*, 87, 024004
- Chu, Q. 2017, PhD thesis, The University of Western Australia
- Coulter, D. A., Foley, R. J., Kilpatrick, C. D., et al. 2017, *Science*, 358, 1556
- Cowperthwaite, P. S., & Berger, E. 2015, *The Astrophysical Journal*, 814, 25
- Creighton, J. D. E., & Anderson, W. G. 2011, *Gravitational-wave physics and astronomy: An introduction to theory, experiment and data analysis* (Wiley)
- Cutler, C., & Flanagan, E. E. 1994, *Phys. Rev. D*, 49, 2658
- Dilday, B., Kessler, R., Frieman, J. A., et al. 2008, *The Astrophysical Journal*, 682, 262
- Drake, A. J., Djorgovski, S. G., Mahabal, A., et al. 2009, *The Astrophysical Journal*, 696, 870
- Dyson, F. W., Eddington, A. S., & Davidson, C. 1920, *Philosophical Transactions of the Royal Society of London. Series A, Containing Papers of a Mathematical or Physical Character*, 220, 291
- Einstein, A. 1916, *Annalen der Physik*, 354, 769
- Farr, W. M., Gair, J. R., Mandel, I., & Cutler, C. 2015, *Phys. Rev. D*, 91, 023005
- Fitzpatrick, E. L. 1999, *Publications of the Astronomical Society of the Pacific*, 111, 63
- Foucart, F. 2012, *Phys. Rev. D*, 86, 124007

- Foucart, F., Hinderer, T., & Nissanke, S. 2018, *Phys. Rev. D*, 98, 081501
- Friedman, J. L. 2018, *International Journal of Modern Physics D*, 27, 1843018
- Frohmaier, C., Sullivan, M., Maguire, K., & Nugent, P. 2018, *The Astrophysical Journal*, 858, 50
- Frohmaier, C., Sullivan, M., Nugent, P. E., Goldstein, D. A., & DeRose, J. 2017, *The Astrophysical Journal Supplement Series*, 230, 4
- Gal-Yam, A., Filippenko, A. V., Jannuzi, B. T., et al. 2007, *Monthly Notices of the Royal Astronomical Society*, 382, 1169
- Gehrels, N., & Mészáros, P. 2012, *Science*, 337, 932
- Gehrels, N., & Swift Team. 2005, in *American Astronomical Society Meeting Abstracts*, Vol. 207, *American Astronomical Society Meeting Abstracts*, 96.01
- Gertsenshtein, M. E., & Pustovoit, V. I. 1963, *Soviet Journal of Experimental and Theoretical Physics*, 16, 433
- Ghirlanda, G., Ghisellini, G., & Celotti, A. 2004, *Astronomy & Astrophysics*, 422, L55–L58
- Ghosh, S., Chatterjee, D., Kaplan, D. L., Brady, P. R., & Sistine, A. V. 2017, *Publications of the Astronomical Society of the Pacific*, 129, 114503
- Ghosh, S., et al. 2016, *Astron. Astrophys.*, 592, A82
- Gilliland, R. L., Nugent, P. E., & Phillips, M. M. 1999, *The Astrophysical Journal*, 521, 30
- Goldstein, A., Veres, P., Burns, E., et al. 2017, *The Astrophysical Journal*, 848, L14
- Graham, M. J., Kulkarni, S. R., Bellm, E. C., et al. 2019, *Publications of the Astronomical Society of the Pacific*, 131, 078001
- Guy, J., Astier, P., Baumont, S., et al. 2007, *Astronomy & Astrophysics*, 466, 11
- Hajela, A., Margutti, R., Alexander, K. D., et al. 2019, *The Astrophysical Journal*, 886, L17
- Hatano, K., Branch, D., & Deaton, J. 1998, *The Astrophysical Journal*, 502, 177
- Hillebrandt, W., & Niemeyer, J. C. 2000, *Annual Review of Astronomy and Astrophysics*,

38, 191

Hinshaw, G., Larson, D., Komatsu, E., et al. 2013, *The Astrophysical Journal Supplement Series*, 208, 19

Ho, A. Y. Q., Kulkarni, S. R., Nugent, P. E., et al. 2018, *The Astrophysical Journal*, 854, L13

Holoien, T. W.-S., Brown, J. S., Vallely, P. J., et al. 2019, *Monthly Notices of the Royal Astronomical Society*, 484, 1899

Hotokezaka, K., & Nakar, E. 2019, Radioactive heating rate of r-process elements and macronova light curve, arXiv:1909.02581

Hulse, R. A., & Taylor, J. H. 1975, *The Astrophysical Journal Letters*, 195, L51

Isaacson, R. A. 1968a, *Phys. Rev.*, 166, 1263

—. 1968b, *Phys. Rev.*, 166, 1272

Ivezić, Ž., et al. 2008, arXiv e-prints, arXiv:0805.2366

Jenet, F., Finn, L. S., Lazio, J., et al. 2009, *The North American Nanohertz Observatory for Gravitational Waves*, arXiv:0909.1058

Kaiser, N., Burgett, W., Chambers, K., et al. 2010, in *Ground-based and Airborne Telescopes III*, ed. L. M. Stepp, R. Gilmozzi, & H. J. Hall, Vol. 7733, *International Society for Optics and Photonics (SPIE)*, 159 – 172

Kalogera, V., & Baym, G. 1996, *The Astrophysical Journal*, 470, L61

Kasen, D., Fernández, R., & Metzger, B. D. 2015, *Monthly Notices of the Royal Astronomical Society*, 450, 1777

Kasliwal, M. M., & Nissanke, S. 2014, *Astrophys. J.*, 789, L5

Kasliwal, M. M., et al. 2016, *Astrophys. J.*, 824, L24

Kasliwal, M. M., Nakar, E., Singer, L. P., et al. 2017, *Science*, 358, 1559

Klebesadel, R. W., Strong, I. B., & Olson, R. A. 1973, *The Astrophysical Journal Letters*, 182, L85

Klimenko, S., Vedovato, G., Drago, M., et al. 2016, *Phys. Rev. D*, 93, 042004

- Korobkin, O., Rosswog, S., Arcones, A., & Winteler, C. 2012, *Monthly Notices of the Royal Astronomical Society*, 426, 1940
- Kulkarni, S. R. 2016, in *American Astronomical Society Meeting Abstracts*, Vol. 227, *American Astronomical Society Meeting Abstracts #227*, 314.01
- Kyutoku, K., Shibata, M., & Taniguchi, K. 2010, *Phys. Rev. D*, 82, 044049
- Lattimer, J. M. 2012, *Annual Review of Nuclear and Particle Science*, 62, 485–515
- Lattimer, J. M., & Schramm, D. N. 1974, *The Astrophysical Journal Letters*, 192, L145
- Law, N. M., Kulkarni, S. R., Dekany, R. G., et al. 2009, *Publications of the Astronomical Society of the Pacific*, 121, 1395
- Li, L.-X., & Paczyński, B. 1998, *The Astrophysical Journal*, 507, L59
- Li, W., Chornock, R., Leaman, J., et al. 2011, *Monthly Notices of the Royal Astronomical Society*, 412, 1473
- Lipunov, V. M., Gorbovskoy, E., Kornilov, V. G., et al. 2017, *The Astrophysical Journal*, 850, L1
- Longair, M. S. 2011, *High energy astrophysics* (Cambridge university press)
- Loredo, T. J., & Wasserman, I. M. 1995, *The Astrophysical Journal Supplement Series*, 96, 261
- Lynch, R., Vitale, S., Essick, R., Katsavounidis, E., & Robinet, F. 2017, *Phys. Rev. D*, 95, 104046
- Mahalanobis, P. C. 1936, *Proceedings of the National Institute of Science of India*, 12, 49
- Maoz, D., & Mannucci, F. 2012, *Publications of the Astronomical Society of Australia*, 29, 447–465
- Messick, C., Blackburn, K., Brady, P., et al. 2017, *Phys. Rev. D*, 95, 042001
- Metzger, B. D. 2017, *Living Reviews in Relativity*, 20, doi:10.1007/s41114-017-0006-z
- Metzger, B. D., Quataert, E., & Thompson, T. A. 2008, *Monthly Notices of the Royal Astronomical Society*, 385, 1455–1460
- Metzger, B. D., Martínez-Pinedo, G., Darbha, S., et al. 2010, *Monthly Notices of the Royal*

- Astronomical Society, 406, 2650–2662
- Misner, C. W., Thorne, K. S., & Wheeler, J. A. 1973, *Gravitation* (W. H. Freeman and Co.)
- Mooley, K. P., Frail, D. A., Dobie, D., et al. 2018, *The Astrophysical Journal*, 868, L11
- Morozova, V., Radice, D., Burrows, A., & Vartanyan, D. 2018, *The Astrophysical Journal*, 861, 10
- Mukherjee, D., Caudill, S., Magee, R., et al. 2018, arXiv e-prints, arXiv:1812.05121
- Narayan, R., Paczynski, B., & Piran, T. 1992, *The Astrophysical Journal*, 395, L83
- Nitz, A. H., Dal Canton, T., Davis, D., & Reyes, S. 2018, *Phys. Rev. D*, 98, 024050
- Nugent, P., Cao, Y., & Kasliwal, M. 2015, in *Visualization and Data Analysis 2015*, ed. D. L. Kao, M. C. Hao, M. A. Livingston, & T. Wischgoll, Vol. 9397, International Society for Optics and Photonics (SPIE), 1 – 7
- Pajkos, M. A., Couch, S. M., Pan, K.-C., & O’Connor, E. P. 2019, *The Astrophysical Journal*, 878, 13
- Pankow, C., Brady, P., Ochsner, E., & O’Shaughnessy, R. 2015, *Phys. Rev. D*, 92, 023002
- Pannarale, F., & Ohme, F. 2014, *The Astrophysical Journal*, 791, L7
- Pedregosa, F., Varoquaux, G., Gramfort, A., et al. 2011, *Journal of Machine Learning Research*, 12, 2825
- Peters, P. C., & Mathews, J. 1963, *Phys. Rev.*, 131, 435
- Phillips, M. M. 1993, *The Astrophysical Journal Letters*, 413, L105
- Piran, T. 2005, *Rev. Mod. Phys.*, 76, 1143
- Rana, J., et al. 2017, *Astrophys. J.*, 838, 108
- Rhoades, C. E., & Ruffini, R. 1974, *Phys. Rev. Lett.*, 32, 324
- Richardson, D., III, R. L. J., Wright, J., & Maddox, L. 2014, *The Astronomical Journal*, 147, 118
- Roberts, L. F., Kasen, D., Lee, W. H., & Ramirez-Ruiz, E. 2011, *The Astrophysical Journal Letters*, 736, L21

- Rosswog, S., Feindt, U., Korobkin, O., et al. 2017, *Classical and Quantum Gravity*, 34, 104001
- Ruiz, M., & Shapiro, S. L. 2017, *Physical Review D*, 96, doi:10.1103/physrevd.96.084063
- Sachdev, S., Caudill, S., Fong, H., et al. 2019, arXiv e-prints, arXiv:1901.08580
- Sako, M., Bassett, B., Becker, A., et al. 2007, *The Astronomical Journal*, 135, 348
- Shanks, T., Metcalfe, N., Chehade, B., et al. 2015, *Monthly Notices of the Royal Astronomical Society*, 451, 4238
- Shibata, M., & Hotokezaka, K. 2019, *Annual Review of Nuclear and Particle Science*, 69, null
- Singer, L. P., & Price, L. R. 2016, *Phys. Rev. D*, 93, 024013
- Singer, L. P., et al. 2014, *Astrophys. J.*, 795, 105
- Singer, L. P., Chen, H.-Y., Holz, D. E., et al. 2016a, *The Astrophysical Journal Letters*, 829, L15
- . 2016b, *The Astrophysical Journal Supplement Series*, 226, 10
- Smartt, S. J. 2009, *Annual Review of Astronomy and Astrophysics*, 47, 63
- Smartt, S. J., et al. 2016, *Monthly Notices of the Royal Astronomical Society*, 462, 4094
- Soares-Santos, M., et al. 2016, *The Astrophysical Journal Letters*, 823, L33
- Soares-Santos, M., Holz, D. E., Annis, J., et al. 2017, *The Astrophysical Journal*, 848, L16
- Srivastava, V., et al. 2017, *Astrophys. J.*, 838, 46
- Sullivan, M. 2004, *The Supernova Legacy Survey*, arXiv:astro-ph/0410594
- Tanaka, M., & Hotokezaka, K. 2013, *The Astrophysical Journal*, 775, 113
- Tanvir, N. R., Levan, A. J., González-Fernández, C., et al. 2017, *The Astrophysical Journal*, 848, L27
- Taylor, J. H., & Weisberg, J. M. 1989, *The Astrophysical Journal*, 345, 434
- The LIGO Scientific Collaboration, the Virgo Collaboration, et al. 2019, *The Astrophysical Journal*, 875, 161
- The LIGO Scientific Collaboration, The Virgo Collaboration, The 1M2H Collaboration,

et al. 2017, Nature, 551, 85

Veitch, J., Raymond, V., Farr, B., et al. 2015, Phys. Rev. D, 91, 042003

Weber, J. 1960, Phys. Rev., 117, 306

CURRICULUM VITAE

Deep Chatterjee

Center for Gravitation Cosmology and Astrophysics,
Department of Physics,
University of Wisconsin – Milwaukee,
3135 N Maryland Ave,
Milwaukee, WI 53211, USA.

Contact
Email (institute): `deep@uwm.edu`
Email (work): `deep.chatterjee@ligo.org`
Nationality: Indian

Education

2015 – 20 : Ph.D. student in Physics, U. Wisconsin-Milwaukee, USA (GPA: 3.975/4.0).

2010 – 15 : Integrated BS-MS in Physics, IISER Kolkata, India (GPA: 8.7/10.0).

Work Experience

Graduate research assistant, UW-Milwaukee Dept. of Physics – Fall 2017, 2018, 2019; Spring 2020

Graduate teaching assistant, UW-Milwaukee Dept. of Physics – Fall 2015, 2016; Spring 2016, 2017, 2018, 2019 for PHY 120, 122, 210, ASTRON 103.

Achievements

Refereed for The Astrophysical Journal.

Papastamatiou Scholarship in Theoretical Physics, Dept. of Physics, UW-Milwaukee (2019-20).

Lichtman fellowship, Dept. of Physics, UW-Milwaukee (Spring 2018).

GROWTH Internship, Caltech, Pasadena (Aug – Oct 2017).

970/990 Physics GRE (2014).

Talks

Gravitational Wave Physics and Astronomy Workshop (GWPAW), Tokyo, Japan (Oct 2019), Source Property Inference from Low-latency LIGO/Virgo Data.

Midwest Workshop on Supernovae and Transients, Columbus OH, US (Sept 2019), Toward Rate Estimation for Transient Surveys.

Rencontres de Moriond, La Thuile, Italy (Mar 2019), GW170817/GRB170817A: The Astronomy/ Astrophysics Point of View. (Invited for LIGO/Virgo Collaboration)

KICP Workshop on Supernovae and Transients, Chicago IL, US (Feb 2019), Predicting Supernova Rates Using iPTF; Estimating the transient detection efficiency.

Gravitational Wave Physics and Astronomy Workshop (GWPAW), College Park MD, US (Dec 2018), LIGO/Virgo Low-latency Public Alerts in the Third Observing Run. (Invited for the LIGO/Virgo Collaboration)

Software Maintenance & Training

Co-librarian for LIGO/Virgo low-latency infrastructure, **GWCelery**.

Project: <https://git.ligo.org/emfollow/gwcelery>

Documentation: <https://gwcelery.readthedocs.io>

Co-librarian for LIGO/Virgo source classification and properties package, **p-astro**.

Python Package Index: <https://pypi.org/project/p-astro>

Co-organizer for LIGO/Virgo low-latency bootcamp, MIT (Oct 2019).

Program: <https://emfollow.docs.ligo.org/bootcamp>

Interests

I am interested in high energy astronomy and astrophysics of compact binary mergers. In particular, multi-messenger observations of the same astrophysical source in both electromagnetic spectrum and in gravitational waves. In case of stellar mass binaries, several factors, like presence of a neutron star, its equation of state, amount of remnant matter post merger could lead to an electromagnetic counterpart. Even if the counterpart is present, finding it after sifting through large sky areas and thousand of possible host galaxies is a challenge. I am interested in understanding the progenitor systems, the type of counterpart that are possible from such systems, and the possibility of joint detection from such systems in both electromagnetic and gravitational waves.

As a member of the Laser Interferometer Gravitational wave Observatory (LIGO) and Virgo collaboration, I work with low-latency sub-group in development of the software infrastructure and data products that help astronomers determine which GW signals to follow-up. I am also a member of the Zwicky Transient Facility (ZTF) collaboration, where I work on developing follow-up strategies for the ZTF telescope. I also work on characterizing detection efficiency of time domain surveys which in turn allows determination of transient rates like supernovae and kilonovae from survey data.

Software Skills

Proficient

Programming: Python, C, Fortran.

Data analytics tools: Pandas, SQL.

Scheduling tools: HTCondor, Slurm, Celery.

Software development: Git, Unix shell, Continuous integration/deployment.

Working knowledge

Programming: Java, Matlab, Octave.

Web interface: Flask.

Outreach

Udaan guest talk, NSPCL Bhilai, India (Jan 8, 2018), Gravitational waves: Listening to the universe.

Coffee shop astrophysics guest talk, Anodyne Coffee, Milwaukee (Nov 11, 2017), Things that go bump and shine in the Night: LIGO Ushering in a new era of multi-messenger Astronomy

Publication List

Deep Chatterjee

Short-author Publications

1. Deep Chatterjee, Shaon Ghosh, Patrick R. Brady, Shasvath J. Kapadia, Andrew L. Miller, Samaya Nissanke, and Francesco Pannarale. A Machine Learning Based Source Property Inference for Compact Binary Mergers. *arXiv e-prints*, page arXiv:1911.00116, 2019
2. Deep Chatterjee, Peter E. Nugent, Patrick R. Brady, Chris Cannella, David L. Kaplan, and Mansi M. Kasliwal. Toward Rate Estimation for Transient Surveys. I. Assessing Transient Detectability and Volume Sensitivity for iPTF. *The Astrophysical Journal*, 881(2):128, Aug 2019
3. Surabhi Sachdev, Sarah Caudill, Heather Fong, Rico K. L. Lo, Cody Messick, Debnandini Mukherjee, Ryan Magee, Leo Tsukada, Kent Blackburn, Patrick Brady, Patrick Brockill, Kipp Cannon, Sydney J. Chamberlin, Deep Chatterjee, Jolien D. E. Creighton, Patrick Godwin, Anuradha Gupta, Chad Hanna, Shasvath Kapadia, Ryan N. Lang, Tjonnie G. F. Li, Duncan Meacher, Alexander Pace, Stephen Privitera, Laleh Sadeghian, Leslie Wade, Madeline Wade, Alan Weinstein, and Sophia Liting Xiao. The GstLAL Search Analysis Methods for Compact Binary Mergers in Advanced LIGO's Second and Advanced Virgo's First Observing Runs. *arXiv e-prints*, page arXiv:1901.08580, Jan 2019
4. Debnandini Mukherjee, Sarah Caudill, Ryan Magee, Cody Messick, Stephen Privitera, Surabhi Sachdev, Kent Blackburn, Patrick Brady, Patrick Brockill, Kipp Cannon, Sydney J. Chamberlin, Deep Chatterjee, Jolien D. E. Creighton, Heather Fong, Patrick Godwin, Chad Hanna, Shasvath Kapadia, Ryan N. Lang, Tjonnie G. F. Li, Rico K. L. Lo, Duncan Meacher, Alex Pace, Laleh Sadeghian, Leo Tsukada, Leslie Wade, Madeline Wade, Alan Weinstein, and Liting Xiao. The GstLAL template bank for spinning compact binary mergers in the second observation run of Advanced LIGO and Virgo. *arXiv e-prints*, page arXiv:1812.05121, Dec 2018
5. Michael W Coughlin, Duo Tao, Man Leong Chan, Deep Chatterjee, Nelson Christensen, Shaon Ghosh, Giuseppe Greco, Yiming Hu, Shasvath Kapadia, Javed Rana, Om Sharan Salafia, and Christopher W Stubbs. Optimizing searches for electromagnetic counterparts of gravitational wave triggers. *Monthly Notices of the Royal Astronomical Society*, 478(1):692–702, 04 2018
6. Shaon Ghosh, Deep Chatterjee, David L. Kaplan, Patrick R. Brady, and Angela Van Sistine. Hunting Electromagnetic Counterparts of Gravitational-wave Events Using the Zwicky Transient Facility. *The Publications of the Astronomical Society of the Pacific*, 129(981):114503, Nov 2017

Collaboration Publications (part of writing team)

1. B. P. Abbott, R. Abbott, T. D. Abbott, et al. GW190425: Observation of a compact binary coalescence with total mass $\sim 3.4M_{\odot}$. *The Astrophysical Journal*, 892(1):L3, mar 2020
2. The LIGO Scientific Collaboration, the Virgo Collaboration, et al. Low-latency Gravitational-wave Alerts for Multimessenger Astronomy during the Second Advanced LIGO and Virgo Observing Run. *The Astrophysical Journal*, 875(2):161, Apr 2019

Collaboration Publications (contributing)

1. The LIGO Scientific Collaboration, the Virgo Collaboration, et al. Binary Black Hole Population Properties Inferred from the First and Second Observing Runs of Advanced LIGO and Advanced Virgo. *arXiv e-prints*, page arXiv:1811.12940, Nov 2018
2. M. M. Kasliwal, E. Nakar, L. P. Singer, et al. Illuminating gravitational waves: A concordant picture of photons from a neutron star merger. *Science*, 358(6370):1559–1565, Dec 2017
3. The LIGO Scientific Collaboration, the Virgo Collaboration, et al. GW170608: Observation of a 19 Solar-mass Binary Black Hole Coalescence. *The Astrophysical Journal Letters*, 851(2):L35, Dec 2017
4. B. P. Abbott, R. Abbott, T. D. Abbott, F. Acernese, K. Ackley, C. Adams, T. Adams, P. Addesso, R. X. Adhikari, V. B. Adya, and et al. Multi-messenger Observations of a Binary Neutron Star Merger. *The Astrophysical Journal Letters*, 848:L12, October 2017
5. The LIGO Scientific Collaboration, the Virgo Collaboration, et al. GW170817: Observation of Gravitational Waves from a Binary Neutron Star Inspiral. *Physical Review Letters*, 119(16):161101, Oct 2017
6. The LIGO Scientific Collaboration, the Virgo Collaboration, et al. GW170814: A Three-Detector Observation of Gravitational Waves from a Binary Black Hole Coalescence. *Physical Review Letters*, 119(14):141101, Oct 2017
7. The LIGO Scientific Collaboration, the Virgo Collaboration, et al. GW170104: Observation of a 50-Solar-Mass Binary Black Hole Coalescence at Redshift 0.2. *Physical Review Letters*, 118(22):221101, Jun 2017